Department of Electrical and Computer Engineering
Centre for Smart Grid and Sustainable Power Systems

Operation and Performance of Three-Phase Asymmetric Multi-Leg Power Transformers Subjected to Nonlinear and Dynamic Electromagnetic Disturbances

Paul S. Moses

This thesis is presented for the Degree of
Doctor of Philosophy
of
Curtin University

July 2012

DECLARATIONS

To the best of my knowledge this thesis contains no material previously published by any other person except where due acknowledgment has been made. This thesis contains no material that has been accepted for the award of any other degree or diploma in any university.

Signature:  Date: 16 July 2012

ABSTRACT

Three-phase power transformers continue to be an important fixture in modern power systems since their initial development in the 1880s. While transformer design has fundamentally remained the same, the operating environment has significantly changed. This is apparent through new flexible network operations (e.g., integration of renewable energy sources), growing network complexities (e.g., deployment of micro-grids, smart grids, etc.) and increasing use of nonlinear power electronic equipment (e.g., power converters and motor drives). Thus the issue of power quality in power systems has become an important consideration to utilities and industries as the performance of electrical machines and devices could be adversely affected. This doctoral thesis focuses on the performance of three-phase power transformers under various nonlinear and dynamic electromagnetic disturbances in distorted power networks.

The first part of this work is devoted to the development and improvement of nonlinear electromagnetic models of three-phase multi-leg transformer cores for the study of steady-state and transient electromagnetic disturbances. This is mainly achieved by developing new detailed magnetic models for ferromagnetic nonlinearities (e.g., hysteresis) as well as considering core asymmetry and magnetic couplings of core-leg fluxes in three-phase multi-leg iron-core structures. These combined effects have not been considered in conventional electromagnetic transient studies of transformers and are shown in this work for the first time to have a significant impact on predicted steady-state and transient electromagnetic behaviour.

In subsequent parts of this thesis, the developed models are applied to the examination of selected nonlinear electromagnetic phenomena such as transformer operation in harmonically distorted power systems (e.g., terminal voltage distortions and nonlinear loads), dc bias caused by geomagnetically induced currents, ferroresonance, and no-load magnetisation and inrush current effects. Furthermore, based on the new modelling approaches, improved methods are presented for

estimating transformer aging with wider applicability to three-phase transformers considering load and source imbalances with harmonic distortions.

With the advent of newly emerging smart grids, the last part of this thesis is devoted to exploring future transformer operation in new smart grid operating conditions such as plug-in electric vehicle charging. Transformer loading patterns with random uncoordinated PEV charging compared to coordinated charging activity in smart grids is investigated. The investigation highlights the notion of harnessing future smart grid technologies to better manage transformer health and performance.

ACKNOWLEDGMENTS

First and foremost, I would like to express my immense gratitude and love to the closest of people in my circle, my parents, Dr. Danny Moses and Vasanthy Moses, who have provided unconditional and unrelenting support during my pursuit of study. I recognise that their hard work and determination were largely for the betterment of my life for which I am eternally grateful. For my parents, it is with great pleasure and deep felt love that I dedicate this work to you.

Special thanks must go to several people in connection with the research documented in this thesis. I am especially grateful for the active and enthusiastic involvement of my primary Supervisor, Dr. Mohammad A. S. Masoum, who has selflessly given countless hours of his time in discussing my research in depth. Associate Supervisor, Professor Hamid A. Toliyat of Texas A & M University and Professor Keyue S. Smedley of University of California, Irvine, United States, are to be thanked for their contributions in this research project serving as co-author in some of my publications. Likewise, Professor Syed M. Islam, Head of Electrical and Computer Engineering Department at Curtin University, has been extremely supportive in my research endeavours.

I owe a debt of gratitude to the scholarship funding sources for the Australian Postgraduate Award (APA) made possible through Curtin University and the Australian Federal Government, Department of Industry, Innovation, Science, Research & Tertiary Education. I am also grateful to the Bentley campus of Curtin University and its staff for maintaining a supportive research environment including access to excellent laboratories, computing resources, office space and library facilities vital to the success of this research. Department Secretary Margaret Pittuck, Postgraduate Administrative Assistant Robyn Cornwell, and Technical Manager Mark Fowler deserve special mention as they have been very helpful in all my administration and study material needs. For providing valuable technical hardware support in the experimental aspects of my work on power transformers, I am grateful

to the skilful laboratory technicians, Mr. Zibby Cielma and Mr. Russell Wilkinson. Without their help, I would not have been able to carry out safe and accurate measurements for validation and testing of theoretical and simulation results.

I would also like to acknowledge the support from my continuing industry employer, the Defence Science and Technology Organisation (DSTO), Department of Defence, Australian Government. I am grateful to my work colleagues, Dr. Damien Killeen, Dr. Dave Matthews, Dr. Matt Legg, Dr. Rod MacLeod, Dr. Ben Travagelione, Dr. Derek Bertilone, Steven Leopardi, Dr. Michael Newman and Hugh Torresan for their kind friendship and invaluable counsel prior-to and during my doctoral program.

Finally, a great many thanks must go to the people who helped in reviewing and proofreading this thesis. The behind-the-scenes and unsung contributors, the reviewers and examiners of this thesis and related publications, should be acknowledged for their time in helping to ensure the work is of a high standard.

TABLE OF CONTENTS

Contents

LIST OF FIGURES

LIST OF TABLES

LIST OF ABBREVIATIONS AND CONVENTIONS

Symbol	Meaning
AC	Alternating current
DC	Direct current
DT	Distribution transformer
EM	Electromagnetic
FIG	Figure
FR	Ferroresonance
G2V, V2G	Grid-to-vehicle, vehicle-to-grid
GIC	Geomagnetically induced currents
GMD	Geomagnetic disturbance
HRS, H	Clock time
HV	High voltage
HVDC	High voltage direct current
IEEE	Institute of Electrical and Electronics Engineers
IET	Institution of Engineering and Technology
LV	Low voltage
MATLAB	Matrix laboratory
MMF	Magnetomotive force
MSS	Maximum sensitivities selection
PCC	Point of common coupling
PEV	Plug-in electric vehicle
PF	Power factor
PSPICE	Personal simulation program with integrated circuit emphasis
PU	Per-unit
RMS	Root mean squared
SCADA	Supervisory control and data acquisition
SWIS	South west interconnected system
THD	Total harmonic distortion
WHF	Weighted harmonic factor
WYE, WYE-G	Star connection, star connection with grounded neutral

Chapter 1. Introduction

1.1 POWER QUALITY AND ELECTROMAGNETIC DISTURBANCES

For over a century, power transformers have been vital ubiquitous links in transmission and distribution networks throughout the world [1]. Virtually all generated ac electrical power must pass through transformers in order to reach the many load centres. In the past couple of decades, extensive application of power electronics and other nonlinear components and loads has resulted in a marked change in the transformer operating environment. This has been brought about by new loading patterns, power conversion technologies for motor drives, renewable energy sources and distributed generation, and most recently, smart grid operations such as battery charging of plug-in electric vehicles. As a result, there has been a measurable rise in the occurrence of transient and steady-state electromagnetic disturbances contributing to distortions in power system voltages and currents. This creates problems for many power components such as rotating electrical machinery and transformers which are only designed for sinusoidal ac operation. Therefore, transformer performance under degraded power quality in transmission and distribution systems has come under further scrutiny in recent times since their service life, reliability, performance and economic operation could be adversely affected [2].

Over the years, a range of electromagnetic disturbances have been noted in power systems that have contributed to performance degradations and premature failures in transformers. The IEEE have broadly classified these disturbances in the IEEE-1159 standard as categorised in Table 1.1 [3]. The effects of these disturbances on transformers have been steadily investigated over the past 2 decades since power quality has gradually become a major issue in industry [4]. However, nonlinear modelling approaches, especially in the area of three-phase transformers, have so far

Table 1.1
Electromagnetic disturbance categories for
power systems as classified by IEEE-1159 [3]

Categories	Typical spectral content	Typical duration	Typical voltage magnitude
1.0 Transients			
1.1 Impulsive			
1.1.1 Nanosecond	5 ns rise	< 50 ns	
1.1.2 Microsecond	1 μs rise	50 ns – 1 ms	
1.1.3 Millisecond	0.1 ms rise	> 1 ms	
1.2 Oscillatory			
1.2.1 Low frequency	< 5 kHz	0.3–50 ms	0–4 pu[a]
1.2.2 Medium frequency	5–500 kHz	20 μs	0–8 pu
1.2.3 High frequency	0.5–5 MHz	5 μs	0–4 pu
2.0 Short-duration root-mean-square (rms) variations			
2.1 Instantaneous			
2.1.1 Sag		0.5–30 cycles	0.1–0.9 pu
2.1.2 Swell		0.5–30 cycles	1.1–1.8 pu
2.2 Momentary			
2.2.1 Interruption		0.5 cycles – 3 s	< 0.1 pu
2.2.2 Sag		30 cycles – 3 s	0.1–0.9 pu
2.2.3 Swell		30 cycles – 3 s	1.1–1.4 pu
2.3 Temporary			
2.3.1 Interruption		>3 s – 1 min	< 0.1 pu
2.3.2 Sag		>3 s – 1 min	0.1–0.9 pu
2.3.3 Swell		>3 s – 1 min	1.1–1.2 pu
3.0 Long duration rms variations			
3.1 Interruption, sustained		> 1 min	0.0 pu
3.2 Undervoltages		> 1 min	0.8–0.9 pu
3.3 Overvoltages		> 1 min	1.1–1.2 pu
3.4 Current overload		> 1 min	
4.0 Imbalance			
4.1 Voltage		steady state	0.5–2%
4.2 Current		steady state	1.0–30%
5.0 Waveform distortion			
5.1 DC offset		steady state	0–0.1%
5.2 Harmonics	0–9 kHz	steady state	0–20%
5.3 Interharmonics	0–9 kHz	steady state	0–2%
5.4 Notching		steady state	
5.5 Noise	broadband	steady state	0–1%
6.0 Voltage fluctuations	< 25 Hz	intermittent	0.1–7% 0.2–2 P_{st}[b]
7.0 Power frequency variations		< 10 s	± 0.10 Hz

been very limited thus preventing the full extent of symptoms from some of these disturbances to be thoroughly assessed. Some of the detrimental effects on transformers symptomatic of degraded power quality in power systems have been observed in the past as follows:

- additional fundamental and harmonic power losses in the iron-core (hysteresis and eddy currents) and copper losses in the winding conductors

- increased winding conductor and iron-core hot-spot temperatures due to higher than rated loss dissipation
- possibility of premature insulation and conductor failure
- higher than usual acoustic noises and mechanical vibration stresses
- nonlinear increase in flux density and core saturation
- reduction in operational energy efficiency
- age reduction in service life time
- derating of nominal transformer load capacity
- decreases in power factor
- possibility of dangerous harmonic resonances and ferroresonance

One of the main goals of this thesis is to develop and improve nonlinear transformer modelling approaches in three-phase multi-leg transformers and carry out new investigations into serious power quality disturbances currently affecting transformers operation. The selected power quality disturbances for study cover a variety of categories listed in IEEE-1159. Moreover, this thesis focuses on transient and steady-state waveform distortion effects from nonlinear loads, terminal voltage harmonics and internally generated harmonics due to transformer nonlinearities. Also investigated are transient inrush current behaviour, hysteresis effects, (sub)harmonic and chaotic ferroresonance, dc bias from geomagnetically induced currents, as well as the aging of transformers operating in distorted and unbalanced power networks.

1.2 THESIS AIMS, MOTIVATION AND RESEARCH OBJECTIVES

Prior studies indicate that the research and industry community could benefit from improved electromagnetic transient and steady-state models for three-phase multi-leg transformers. Until recent times, the majority of transformer studies were performed only with simplified single-phase transformer models because of the complexity of properly including the magnetic interactions of multi-leg cores. In the last two decades, computing power has notably advanced making it possible to implement

and numerically solve complex high-level models necessary for three-phase transformers. In the present context of growing network complexity and usage of nonlinear power electronic devices, the need for improved nonlinear models of transformers for evaluating power quality impacts is clearly a priority. In lieu of this, the following research activities and objectives were defined for this thesis:

- Review of nonlinear electromagnetic models of three-phase power transformers and power quality issues impacting transformer performance.
- Development of a new nonlinear electromagnetic model for power transformers applicable to asymmetric three-phase multi-leg transformer core structures, (un)balanced non-sinusoidal excitations and (un)balanced (non)linear loading.
- Initiate a study into ferromagnetic hysteresis effects and their impacts on transformer magnetisation current behaviour, input/output current/voltage waveforms, losses and aging including experimental validation.
- Application of model to the study and prediction of three-phase transformer ferroresonance in multi-leg iron cores substantiated by experimental testing.
- Investigate symmetrical and unsymmetrical dc bias effects from geomagnetically induced currents (GICs) in three-phase transformers.
- Application of model for improved accuracy in estimating transformer aging.
- Study possible future smart grid operations impacting transformer performance (e.g., electric vehicle charging) and the application of smart grid technologies for transformer health management.

Generally, the research activities described above are organised to first develop and improve upon existing nonlinear models in order to carry out a series of investigations into selected power quality disturbances. The improvement of nonlinear models is necessary to enable ensuing studies of more complex and dynamic electromagnetic disturbances such as ferroresonance. The last few steps are

aimed at demonstrating other applications of the developed modelling tools in predicting transformer stresses and evaluating performance (e.g., transformer aging).

1.3 THESIS FORMAT AND OUTLINE

This thesis is organised into 8 chapters comprising of this introduction chapter followed by large chapters carrying out investigations into various transformer power quality issues. The main chapters individually address each topic with an introduction, analysis of simulation and experimental results, and the conclusions for each major investigation.

Thesis chapters are organised as follows:

Chapter 1 (this chapter) introduces the topics investigated in this thesis as well as providing an overview of the motivation, aims and research objectives.

Chapter 2 provides an overview of transformer modelling methodologies for transient and steady-state electromagnetic disturbances. The deficiencies in existing three-phase transformer models are particularly emphasised. A novel enhanced nonlinear model is proposed in this chapter that is applicable to three-phase transformers with asymmetric multi-leg core structures. The development details of the new ferromagnetic core models with hysteresis nonlinearities are given together with their implementation into multi-leg magnetic circuits of three-phase transformer cores.

Chapter 3 initiates a study into steady-state and transient electromagnetic disturbances affecting three-phase power transformers. The developed nonlinear model detailed in Chapter 2 is used to carry out the investigation with supporting experimental tests. Specifically, no-load magnetisation and inrush current effects in three-leg transformer cores are analysed which also forms the basis for the validation testing of the proposed model.

Chapter 4 continues the study into a more serious and destructive electromagnetic

disturbance known as ferroresonance. Inadequate approaches with deficient magnetic core models of three-phase transformers have largely limited the study of ferroresonance. This chapter focuses on the three-phase transformer ferroresonance phenomenon with special emphasis on the combined effects of capacitor switching, hysteresis nonlinearities and multi-leg magnetic circuits so far ignored in prior studies. This chapter also provides additional validation of the proposed model by testing its ability to predict ferroresonance modes measured in the laboratory.

Chapter 5 initiates an investigation into the very serious and widespread phenomenon of geomagnetically induced currents (GICs). A new study into GIC effects on asymmetric multi-leg transformer cores is carried out with the developed model. This chapter also provides a detailed theoretical derivation of magnetic circuit fluxes in three-leg transformers cores with symmetrical and unsymmetrical dc biases injected by GICs. More importantly, a possible means in suppressing dc bias effects and harmonics in three-leg transformer cores is demonstrated and verified through simulation and experimental studies.

Chapter 6 presents a new method of estimating transformer aging in three-phase transformers which for the first time considers core nonlinearities, multiple fluxes coupling in multi-leg cores, and nonlinear loads in unbalanced distorted networks. The aging estimation is demonstrated for several practical transformer operational scenarios and is compared to conventional aging estimation approaches.

Chapter 7 begins a study into possible transformer loading issues considering future smart grid operations. Various battery charging scenarios are investigated for multiple plug-in electric vehicles (PEVs) randomly plugging into large distribution systems. Based on power flow studies for a distribution system, the effects on distribution transformers with random uncoordinated PEV charging are simulated. Finally, the benefits of adopting smart coordinated PEV charging on transformer performance are simulated and evaluated.

Chapter 8 provides an overview of the thesis contributions, main conclusions and a summary of topics suitable for further research.

1.4 LIST OF PUBLICATIONS

The main content of this thesis is supported by the following published journal articles and presented conference papers.

- **Journal articles:**

[J1] **P. S. Moses** and M. A. S. Masoum, "Three-phase asymmetric transformer aging considering voltage-current harmonic interactions, unbalanced nonlinear loads, magnetic couplings and hysteresis," ***IEEE Transactions on Energy Conversion*****,** vol. 27, no. 2, pp. 318-327, 2012.

[J2] **P. S. Moses,** M. A. S. Masoum, and H. A. Toliyat, "Impacts of hysteresis and magnetic couplings on the stability domain of ferroresonance in asymmetric three-phase three-leg transformers," ***IEEE Transactions on Energy Conversion,*** vol. 26, no. 2, pp. 581-592, 2011.

[J3] **P. S. Moses,** M. A. S. Masoum, and H. A. Toliyat, "Dynamic modeling of three-phase asymmetric power transformers with magnetic hysteresis: no-load and inrush conditions," ***IEEE Transactions on Energy Conversion,*** vol. 25, no. 4, pp. 1040-1047, 2010.

[J4] M. A. S. Masoum and **P. S. Moses**, "Impact of balanced and unbalanced direct current bias on harmonic distortion generated by asymmetric three-phase three-leg transformers," ***IET Electric Power Applications,*** vol. 4, no. 7, pp. 507-515, 2010.

[J5] **P. S. Moses** and M. A. S. Masoum, "Modeling subharmonic and chaotic ferroresonance with transformer core model including magnetic hysteresis effects," *WSEAS Transaction on Power Systems,* vol. 4, no. 12, pp. 361-371, 2009.

[J6] M. A. S. Masoum, **P. S. Moses**, and A. S. Masoum, "Derating of asymmetric three-phase transformers serving unbalanced nonlinear loads," ***IEEE***

Transactions on Power Delivery, vol. 23, no. 4, pp. 2033-2041, 2008.

[J7] A. Masoum, S. Deilami, **P. S. Moses**, M. A. S. Masoum, and A. Abu-Siada, "Smart load management of Plug-In Electric Vehicles in distribution and residential networks with charging stations for peak shaving and loss minimization considering voltage regulation," ***IET Generation, Transmission & Distribution***, vol. 5, no. 8, pp. 877-888, 2011.

[J8] S. Deilami, A. Masoum, **P. S. Moses**, and M. A. S. Masoum, "Real-time coordination of Plug-In Electric Vehicle charging in smart grids to minimize power losses and improve voltage profile," ***IEEE Transactions on Smart Grid*****,** vol. 2, no. 3, pp. 456-467, 2011.

[J9] M. Mesbah, **P. S. Moses**, S. M. Islam, and M. A. S. Masoum, " Prototype hardware implementation of a fault emulator and its application to the transient study of three-phase three-leg power transformers," ***IEEE Transactions on Industrial Informatics,*** (under 2nd review).

- **Conference papers:**

[C1] **P. S. Moses**, M. A. S. Masoum, and M. Moghbel, "Effects of iron-core topology on inrush currents in three-phase multi-leg power transformers," IEEE Power Engineering Society General Meeting San Diego, USA, July 22-26, 2012. Accepted for presentation/publication (Paper # 2012GM0693).

[C2] M. A. S. Masoum, **P. S. Moses**, and S. Hajforoosh, "Distribution transformer stress in smart grid with coordinated charging of plug-in electric vehicles," in Proc. International Conference on Innovative Smart Grid Technologies (ISGT), Washington D. C., USA, 2012, pp. 1-7.

[C3] A. Masoum, **P. S. Moses**, A. S. Masoum, and A. Abu-Siada, "Impact of rooftop PV generation on distribution transformer and voltage profile of residential and commercial networks," in Proc. International Conference on Innovative Smart Grid Technologies (ISGT), Washington D. C., USA, 2012,

pp. 1-7.

[C4] **P. S. Moses**, M. A. S. Masoum, and S. Hajforoosh, "Overloading of distribution transformers in smart grid due to uncoordinated charging of Plug-In Electric Vehicles," in Proc. International Conference on Innovative Smart Grid Technologies (ISGT), Washington D. C., USA, 2012, pp. 1-7.

[C5] **P. S. Moses** and M. A. S. Masoum, "Distortions in three-phase transformer magnetizing currents with nonsinusoidal conditions considering magnetic hysteresis and leg-flux coupling effects," in Proc. Australasian Universities Power Engineering Conference (AUPEC), Brisbane, Australia, 2011, pp. 1-5.

[C6] **P. S. Moses,** M. A. S. Masoum, and K. M. Smedley, "Harmonic losses and stresses of nonlinear three-phase distribution transformers serving Plug-In Electric Vehicle charging stations," in Proc. International Conference on Innovative Smart Grid Technologies (ISGT), Anaheim, California USA, 2011, pp. 1-6.

[C7] **P. S. Moses** and M. A. S. Masoum, "Modeling and analysis of the suppression of ferroresonance in nonlinear three-phase three-leg transformers," in Proc. IEEE Power Engineering Society General Meeting Detroit, USA, 2011, pp. 1-6.

[C8] M. A. S. Masoum, **P. S. Moses**, and K. M. Smedley, "Distribution transformer losses and performance in smart grids with residential plug-in electric vehicle charging," in Proc. International Conference on Innovative Smart Grid Technologies (ISGT), Anaheim, California USA, 2011, pp. 1-7.

[C9] **P. S. Moses**, A. Masoum, and M. A. S. Masoum, "Operation of three-phase three-leg power transformers subject to voltage swell," in Proc. Electrical Power Quality and Utilisation (EPQU), Lisbon, Portugal, 2012, pp. 1-5.

[C10] P. Juanuwattanakul, M. A. S. Masoum, and **P. S. Moses**, "Voltage analysis for placement of DG in unbalanced distribution networks," in Proc. Electrical Power Quality and Utilisation (EPQU), Lisbon, Portugal, 2012, pp. 1-4.

[C11] **P. S. Moses**, S. Deilami, A. S. Masoum, and M. A. S. Masoum, "Power quality of smart grids with plug-in electric vehicles considering battery charging profile," in Proc. IEEE PES Conference on Innovative Smart Grid Technologies Europe, Chalmers Lindholmen, Gothenburg, Sweden, 2010, pp. 1-7.

[C12] S. Deilami, A. S. Masoum, **P. S. Moses**, and M. A. S. Masoum, "Voltage profile and THD of residential network with high penetration of Plug-in Electrical Vehicles," in Proc. IEEE PES Conference on Innovative Smart Grid Technologies (ISGT) Europe, Chalmers Lindholmen, Gothenburg, Sweden, 2010, pp. 1-6.

[C13] A. S. Masoum, S. Deilami, **P. S. Moses**, and A. Abu-Siada, "Impacts of battery charging rates of plug-in electric vehicle on smart grid distribution systems," in Proc. IEEE PES Conference on Innovative Smart Grid Technologies (ISGT) Europe, Chalmers Lindholmen, Gothenburg, Sweden, 2010, pp. 1-6.

[C14] **P. S. Moses** and A. S. Masoum, "Sensitivity analysis of ferroresonance simulations to small variations in model parameters and initial conditions," in Proc. Australasian Universities Power Engineering Conference (AUPEC), Christchurch, New Zealand, 2010, pp. 1-6.

[C15] A. Masoum, **P. S. Moses**, and A. Abu-Siada, "Impact of voltage sags on three-phase power transformers," in Proc. Australasian Universities Power Engineering Conference (AUPEC), Christchurch, New Zealand, 2010, pp.1-6.

[C16] A. Masoum, S. Deilami, **P. S. Moses**, and A. Abu-Siada, "Impact of plug-in electrical vehicles on voltage profile and losses of residential system" in Proc. Australasian Universities Power Engineering Conference (AUPEC), Christchurch, New Zealand, 2010, pp. 1-6.

[C17] **P. S. Moses** and M. A. S. Masoum, "Experimental and simulation analysis of ferroresonance in single-phase transformers considering magnetic hysteresis effects," in Proc. IEEE Power Engineering Society General Meeting

Minneapolis, USA, 2010, pp. 1-6.

[C18] M. A. S. Masoum, **P. S. Moses**, and S. Deilami, "Load management in smart grids considering harmonic distortion and transformer derating," in Proc. International Conference on Innovative Smart Grid Technologies (ISGT), 2010, pp. 1-7.

[C19] **P. S. Moses** and M. A. S. Masoum, "Modeling ferroresonance in asymmetric three-phase power transformers," in Proc. Australasian Universities Power Engineering Conference (AUPEC), 2009, pp. 1-6.

[C20] **P. S. Moses** and M. A. S. Masoum, "A transformer core model including magnetic hysteresis effects for ferroresonance studies," in Proc. WSEAS Genova, Italy: 9th WSEAS International Conf. on Electric Power Systems, High Voltages, Electric Machines, 2009.

[C21] M. A. S. Masoum and **P. S. Moses**, "Influence of geomagnetically induced currents on three-phase power transformers," in Proc. Australasian Universities Power Engineering Conference (AUPEC), Sydney, Australia, 2008, pp. 1-5.

[C22] M. A. S. Masoum, **P. S. Moses**, and A. S. Masoum, "Impact of adjustable speed PWM drives on operation and harmonic losses of nonlinear three phase transformers," in Proc. 7th International Conference on Power Electronics and Drive Systems (PEDS), 2007, pp. 562-567.

Chapter 2. Dynamic modelling of three-phase power transformers

2.1 INTRODUCTION

This chapter provides an overview of existing three-phase transformer modelling approaches and culminates in the proposal of a new enhanced nonlinear model for three-phase multi-leg transformer cores. The proposed new model will be the basis for the transient and steady-state investigations performed in the latter parts of this thesis. The current state-of-the-art of electromagnetic modelling for three-phase transformers is discussed as well as the deficiencies and short-comings of existing transformer transient studies.

2.1.1 Magnetic circuit modelling of transformers

Despite significant advancements in transformer computer models over the last two decades, three-phase transformer modelling techniques have not progressed as far as their single-phase counterparts. This is mainly due to the additional complexities introduced by multiple flux paths in multi-leg iron-core structures (Fig. 2.1) and their associated ferromagnetic nonlinearities. Furthermore, determination of nonlinear electromagnetic parameters in multi-leg cores is also a significant challenge [5, 6].

The majority of three-phase transformer studies are based mainly on single-phase transformer models that only amount to a "per-phase" representation. Inherent in this approach is the assumption of isolated magnetic cores for each phase that do not exhibit any flux interaction with one another. For three-phase transformers, this approximation would only be valid for a three-phase transformer "bank" or triplex core (i.e., three single-phase transformers) that have isolated cores possibly sharing a tank [5, 7]. A simple consequence of the magnetic circuit fluxes in multi-leg cores is that if a single-phase ac voltage is connected to only one of the coil windings,

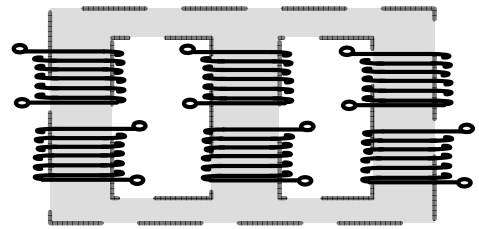

Core formed (stacked)

- Core-form: **least amount of core material**
- Stacked lamination
- **Worst problem: zero sequence fluxes cannot circulate and forced through air and tank**
- **Tank heating problem**

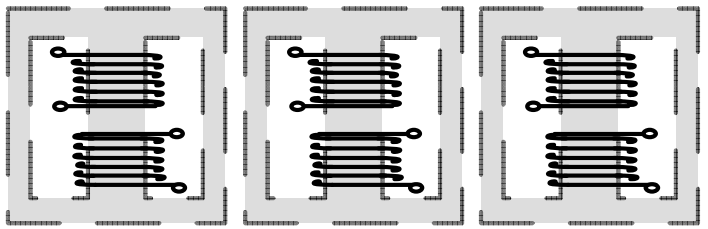

Triplex core (wound or stacked)

- Similar magnetic characteristics to 3x 1Ø transformer banks
- Cores share same tank but magnetically isolated.
- Zero sequence flux circulates in each core
- **minimal tank heating**

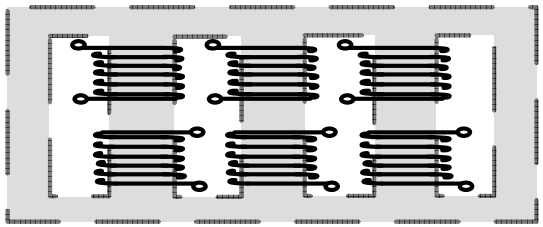

5-legged stacked core

- Magnetic path for zero sequence flux
- More symmetric core
- Often used for low-profile for shipping or visual appearance in urban substations

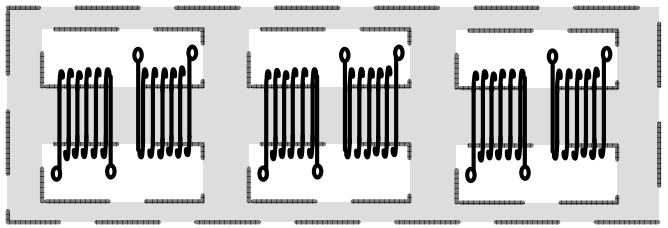

Shell form (stacked)

- Shell-form: provides magnetic path for zero sequence flux
- **Better suited for unbalanced operation**
- Stacked laminations

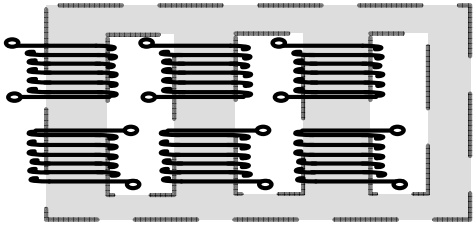

4-legged stacked core

- Provides magnetic path for zero sequence flux
- **Outer phases do not exhibit like behavior**
- Not very common

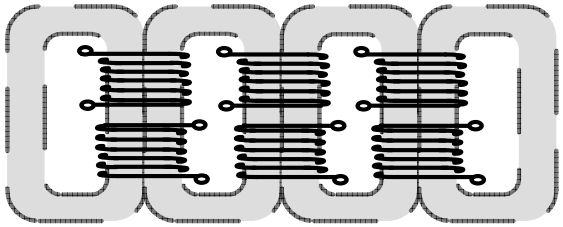

5-legged wound core

- Four concentrically laminated cores
- Only adjacent phases are directly linked magnetically
- Virtually no magnetically coupling in outer windings
- Zero sequence fluxes contained in core
- **minimal tank heating**

Fig. 2.1. Overview of three-phase multi-leg transformer core topologies and their inherent magnetic characteristics.

voltages will still be induced in all other disconnected phases due to ac fluxes "spilling over" into adjacent core-legs. The magnetic flux interactions in multi-leg cores are very slowly being introduced into main stream three-phase transformer models. Virtually all commercial computer simulation tools have yet to adopt such models into their libraries and opt for the simpler per-phase equivalent models. Therefore, emerging three-phase transformer models attempting to include multi-leg core topologies must be custom developed by researchers. An overview of multi-leg transformer core structures is depicted in Fig. 2.1.

2.1.2 Modelling of ferromagnetic core nonlinearities

In addition to core topology considerations is the issue of accurate modelling of the ferromagnetic iron-core nonlinearities. Traditionally, the core behaviour has been modelled with simplified single-value nonlinear functions (e.g., polynomials, arctangent, exponential) or multi-segment piece-wise linear expressions to approximate the nonlinear B-H characteristics. This is usually sufficient for steady-state analysis [8]; however, most dynamic and transient disturbances such as dc biasing, voltage sag/swell, inrush and ferroresonance [9, 10] require more accurate methods. Thus, the impetus is therefore to now to improve core model accuracy by incorporating the complicated hysteresis nonlinearities with their major and minor loop trajectories into transformer core representations [10-12]. This to some degree has recently been considered in single-phase transformers models [9, 13-15] proving beneficial in more accurately modelling single-phase electromagnetic disturbances. However, including these core nonlinearities into three-phase multi-leg transformer models has been exceptionally challenging in the past due to numerical solution complexities and lack of adequate computing power.

Three-phase transformer modelling complexity arises in the need to model each segment of multi-leg cores which carry different time-varying fluxes interacting with one another under three-phase excitation. The solution is further complicated when attempting to include hysteresis nonlinearities into the magnetic core environment. Hence, in the past this has led to compromises of using simplified non-hysteretic

core models or ignoring the multi-leg magnetic circuit completely. To address this, in the following sections a new approach to modelling hysteresis behaviour in multi-leg cores is proposed to improve the dynamic modelling of three-phase transformers.

2.1.3 Physical hysteresis models

A variety of hysteresis models are already available in literature [16, 17] for studying the physical properties of ferromagnetism. Jiles-Atherton [18] and Preisach [19, 20] based models are perhaps the most renowned. However, core model identification methods in these approaches require highly extensive measurements. The Preisach based model requires a set of first order descending curves of minor hysteresis loops to be measured. Jiles-Atherton equations use five parameters difficult to measure accurately requiring a laborious trial and error approach. An alternative approach was sought in this study where fewer tests are needed to characterise three-leg transformer cores. Tellinen [21] proposed a scalar hysteresis model with proven accuracy in recreating both major and minor hysteresis loops. Only the major hysteresis loop needs to be measured from which minor loop effects are dynamically estimated. Thus, this model is an ideal candidate for developing a suitable three-phase transformer core representation which is later described in depth.

2.1.4 Hysteresis modelling in three-phase transformers

There are very few three-phase transformer models which, to certain degrees, consider hysteretic effects. Reference [22] proposes a theoretical transformer model based on a series of exponential curves, however, no experimental validation was given. A five-leg transformer model for transient studies is developed in [23] based on nonlinear voltage dependent core-loss resistors. This approach does not account for dynamic hysteresis behaviour in which core flux amplitudes more directly impact core-losses than the applied voltage. A three-phase transformer model using a simplified Preisach based [19] hysteresis model is proposed in [24]. Unfortunately, there is limited agreement with experimental results. More recently, a finite element model for three-phase transformers using a Jiles-Atherton hysteresis approach [18] is developed in [12]. High accuracy is demonstrated for steady-state no-load behaviour

but requires intensive calculations and detailed knowledge about the core structures dimensions and magnetic properties. In [11, 25], three-phase transformer models including hysteresis and eddy current effects are developed for steady-state and transient operation. None of these models consider core asymmetry in the geometry with unique dynamic leg hysteresis nonlinearities for multi-legged cores.

A new approach to modelling three-phase multi-leg transformers is proposed in this PhD research [26]. Unlike previous methods, this model offers reduced complexity, easier core characterisation tests, and accurate representation of core asymmetry with magnetically coupled hysteresis nonlinearities in each core leg. Furthermore, hysteresis functions are developed as modular PSPICE [27] subcircuit components for flexible implementation for system studies and other core topologies. In subsequent chapters, the model performance is tested under several conditions such as no-load, inrush, ferroresonance and dc bias with full experimental validation.

2.2 NEW APPROACH TO HYSTERESIS MODELLING FOR THREE-PHASE TRANSFORMER CORE STRUCTURES

The essential attributes which classify the capability of three-phase transformer models are (1) electrical coupling due to winding connections, (2) magnetic coupling and core flux interaction due to core topologies (e.g., three-leg, five-leg designs [5]), (3) nonlinear core representation and (4) lossy behaviour due to the ohmic, hysteresis and eddy current losses. Considering these effects, a novel three-phase transformer core model with integrated dynamic hysteresis nonlinearities for each magnetic leg is proposed (Fig. 2.2). Asymmetrical iron-core structures with different hysteresis behaviour are considered by employing individual PSPICE subcircuits for each magnetic core segment.

The model development is covered in three main stages: (1) selection of model topology, (2) integration of an appropriate nonlinear hysteresis core model and (3) model implementation into a suitable time-domain simulation environment.

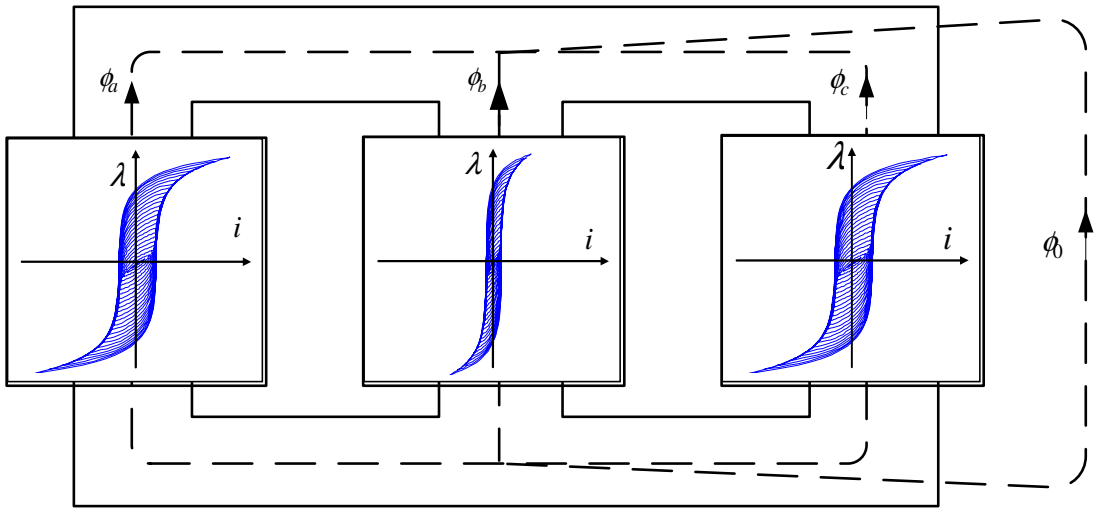

Fig. 2.2. Proposed three-phase multi-leg transformer model concept with integrated asymmetric hysteresis nonlinearities for each core-leg.

2.2.1 Three-phase three-leg transformer model topology

The most distinguishing feature of three-phase transformer models is the need to account for the mutual magnetic coupling amongst the core legs. Furthermore, core asymmetry due to differing leg and yoke reluctances requires special attention in some core structures. This issue of asymmetry has rarely been considered, and then only, with non-hysteretic models [6, 28]. Research indicates that perhaps the most promising approach is to adopt a duality-based topological representation for three-phase transformer core structures [5, 29, 30]. The duality-based approach considers the classical electrical equivalent circuit coupled with a magnetic equivalent circuit (Figs. 2.2-2.3). The duality principle also allows magnetic fluxes to be represented as currents, mmfs as voltages and reluctances as resistances [5, 31-33] which obey established electrical circuit laws that can be more easily solved.

Electric circuit topology

The developed model uses the classical electric equivalent circuit (Fig. 2.3) considering winding connections (e.g., wye/wye) and transformer losses. Linear resistances account for the ohmic, hysteresis and eddy current losses while linear inductors represent leakage fluxes inductances. Three-phase open and short-circuit tests were performed to evaluate the electric circuit parameters (see Appendix A).

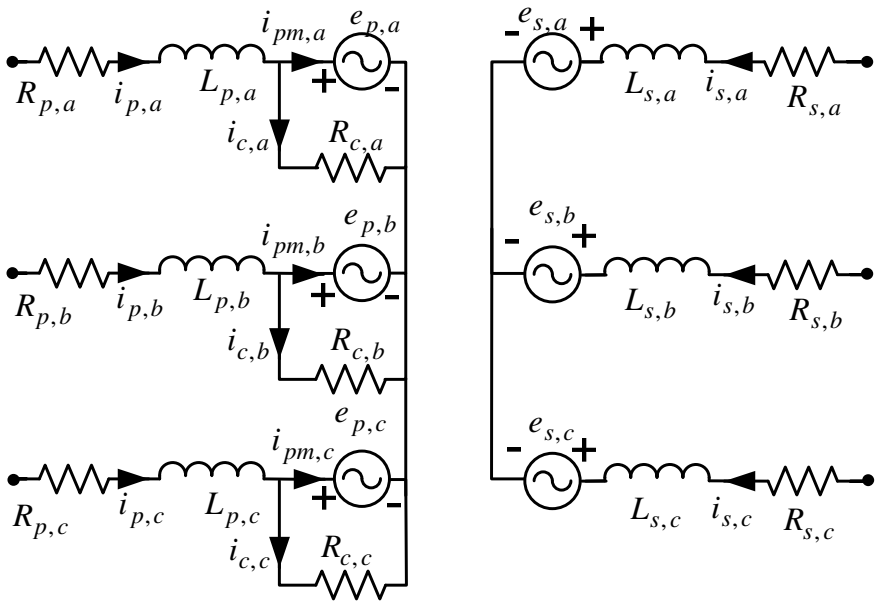

Fig. 2.3. Three-phase three-leg electric equivalent circuit (wye/wye).

Assuming wye/wye winding connections, the governing circuit equations describing the electrical behaviour can be stated as

$$\begin{aligned} v_{p,x}(t) &= R_{p,x}\, i_{p,x}(t) + L_{p,x}\frac{di_{p,x}(t)}{dt} + \frac{d\lambda_{p,x}(t)}{dt} \\ v_{s,x}(t) &= R_{s,x}\, i_{s,x}(t) + L_{s,x}\frac{di_{s,x}(t)}{dt} + \frac{d\lambda_{s,x}(t)}{dt} \qquad (x = a,b,c) \end{aligned} \tag{2.1}$$

where $v_{p,x}$, $v_{s,x}$, $i_{p,x}$, $i_{s,x}$, $\lambda_{p,x}$ and $\lambda_{s,x}$ are the primary/secondary terminal voltages, winding currents and flux linkages, respectively, and x denotes the corresponding phase a, b or c. The respective primary and secondary phase winding resistances and inductances are $R_{p,x}$, $R_{s,x}$, $L_{p,x}$ and $L_{s,x}$. The induced voltages are generated by a controlled voltage source based on the derivative of magnetic flux (Faraday's Law) as determined by the magnetic circuit. Other winding configurations (e.g., wye/delta) present no restrictions on model implementation.

Magnetic circuit topology

The full three-leg core magnetic circuit (Fig. 2.4a) consists of nonlinear reluctance terms for the three leg ($\Re_a, \Re_b, \Re_c$) and the four yoke ($\Re_{ab}, \Re_{cb}, \Re_{ba}, \Re_{ab}$) segments, as

well as three additional reluctances for the magnetic tank and air flux paths ($\Re_{aa}, \Re_{bb}, \Re_{cc}$). Ordinarily, determination of these individual reluctances requires detailed manufacturer data of core dimensions and saturation characteristics which are not usually available and almost impossible to measure accurately.

Therefore, for this work, the individual reluctances for the full magnetic circuit are reduced to three reluctances ($\Re_a^*, \Re_b^*, \Re_c^*$) by lumping the yoke segments into respective leg reluctances. Furthermore, air gap reluctances $\Re_{aa}$, $\Re_{bb}$ and $\Re_{cc}$ are very large compared to the remaining reluctances and can be either neglected or lumped into a single linear reluctance. This reluctance approximates the flux paths through air gaps or the magnetic tank structure which is obtained from the zero-sequence tests described in [6]. The mmfs developed in the primary windings ($F_{p,a}$,

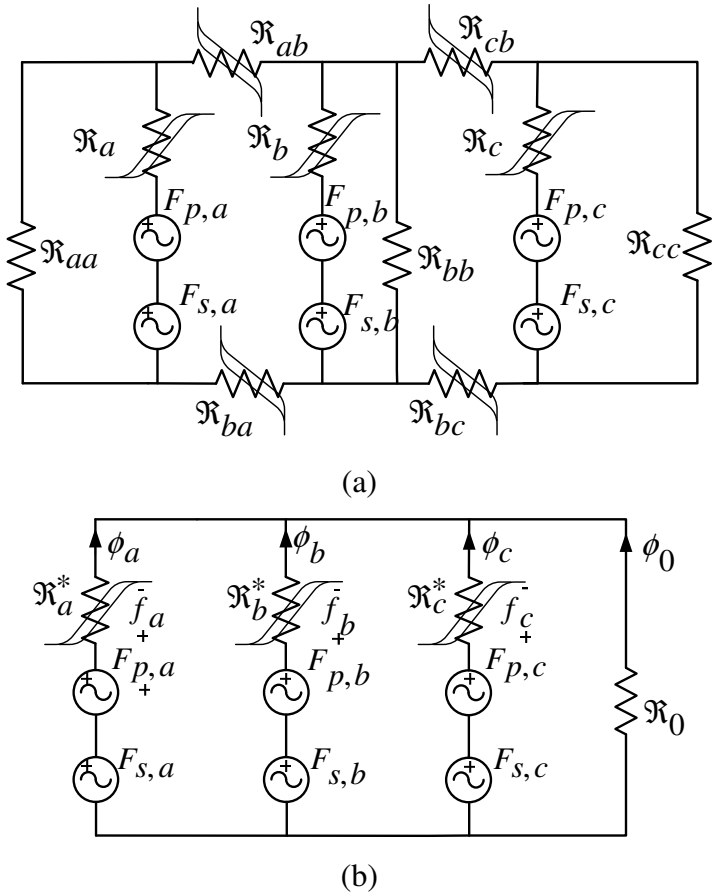

Fig. 2.4. (a) Full magnetic equivalent circuit and (b) reduced approximate equivalent circuit for three-leg three-phase transformer.

$F_{p,b}$, $F_{p,c}$) and secondary windings ($F_{s,a}$, $F_{s,b}$, $F_{s,c}$) are also shown where $F_p = N_p i_{pm}$ and $F_s = N_s i_s$ assuming the current directions indicated in Fig. 2.3. Fig. 2.4b shows the reduced approximate magnetic circuit and emphasises the fact that magnetic hysteresis effects takes place in all ferromagnetic core segments which should be accounted for in core models. This approximate equivalent circuit permits simple laboratory tests for determination of each of the legs magnetising characteristics and provides acceptable results [28, 32-35].

The nonlinear leg reluctances are realised by controlled current sources dependent on their developed leg mmf potential f_x. In this work, these current sources are part of a hysteresis subcircuit block specially designed to model dynamic hysteresis nonlinearities as discussed in the next section. The magnetic circuit accounts for interphase flux interactions in the core and the effect of zero-sequence air or tank flux paths. Therefore, the following relationship must hold true for the magnetic circuit model of Fig. 2.5.

$$\phi_a + \phi_b + \phi_c + \phi_0 = 0 \tag{2.2}$$

2.2.2 Inclusion of hysteresis models for three-leg cores

To account for core asymmetry, each core leg is modelled with its own customisable hysteresis nonlinearity. The magnetic circuit allows the hysteretic behaviour of the legs to interact with one another as is true in real three-phase multi-leg core structures. The scalar hysteresis model formulated in [21] is selected and modified for use in three-leg cores. The main variables are magnetic flux density B and applied field intensity H. However, in this work, the equations (hereafter referred to as the 'hysteresis equations') are modified such that magnetic flux and magnetomotive forces are computed instead of B and H (i.e., $B \rightarrow \phi$ and $H \rightarrow f$). These quantities are easier to measure and allow the hysteresis models to be directly integrated into the iron-core magnetic equivalent circuit. The modified hysteresis equations are

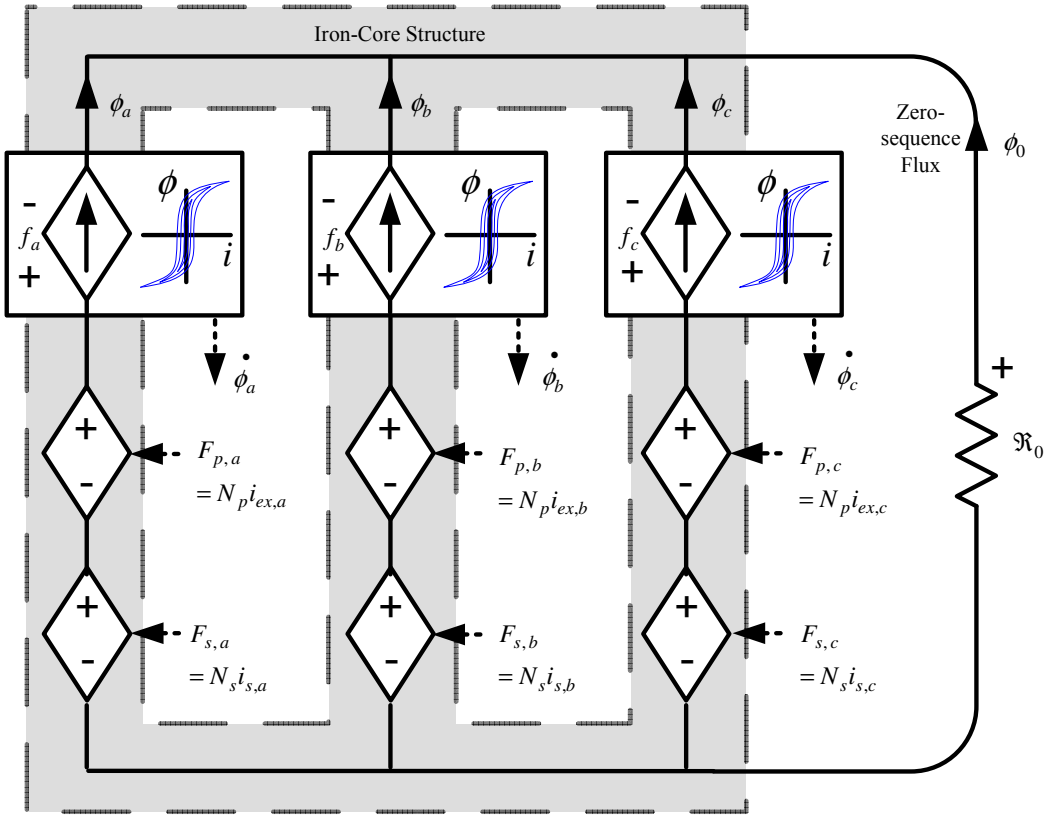

Fig. 2.5. Magnetic equivalent circuit for three-leg three-phase transformer.

$$\frac{d\phi_x}{dt} = \frac{df_x}{dt}\left[\rho_x + \frac{\phi_x^-(f_x) - \phi_x(f_x)}{\phi_x^-(f_x) - \phi_x^+(f_x)}\left(\frac{d\phi_x^+(f_x)}{df_x} - \rho_x\right)\right] \quad \text{if } \frac{d\phi_x}{dt} \geq 0 \tag{2.3a}$$

$$\frac{d\phi_x}{dt} = \frac{df_x}{dt}\left[\rho_x + \frac{\phi_x(f_x) - \phi_x^+(f_x)}{\phi_x^-(f_x) - \phi_x^+(f_x)}\left(\frac{d\phi_x^-(f_x)}{df_x} - \rho_x\right)\right] \quad \text{if } \frac{d\phi_x}{dt} < 0 \ (x = a,b,c) \tag{2.3b}$$

where ϕ_x^+, ϕ_x^- and ϕ_x are the limiting ascending, descending curve functions and instantaneous leg fluxes, respectively, for each phase *x*, dependent on the developed leg mmfs f_x. ρ_x is the slope of the fully saturated region along the limiting hysteresis curves.

From a magnetics standpoint, the modified hysteresis equations are based on domain wall motion theory of ferromagnetic material which governs B-H characteristic behaviour. This core model assumes domain wall motion densities (Barkhausen [36] jumps) vary proportionally to the growth or recession of domain regions corresponding to changes in field strength [21]. This is a departure from other hysteresis models used in transformer studies that typically approximate minor hysteresis loops with scaled versions of the major loop. These existing models cannot account for arbitrary hysteresis loop formations that occur under transient disturbances leading to discrepancies in predicted transformer behaviour. It is therefore important to note that because the developed hysteresis model is based on true physical ferromagnetism behaviour, it is capable of estimating magnetic response for arbitrary (non)sinusoidal and transient transformer operation (e.g., inrush, ferroresonance and harmonic distortion).

In order to compute the hysteresis equations (2.3), the ascending and descending limiting curves ($\phi_x^+(f_x), \phi_x^-(f_x)$) must first be defined and evaluated. The following nonlinear function is proposed

$$\phi(f) = \mathrm{sgn}(f) \cdot \alpha \log_e\left(\beta |f| + 1\right) \tag{2.4}$$

This function has the advantage of only requiring two fitting parameters (α_x, β_x) to shape the curve to measured data. α_x and β_x influence the vertical and horizontal scaling of $\phi(f)$, respectively. By shifting the function (2.4) to the right (or left) by σ_x, the limiting ascending (or descending) curve function enclosing the major hysteresis loop can be defined. Therefore, σ_x effectively controls the width of the major hysteresis loop. This approach of uniquely specifying $\phi_x^+(f_x)$ and $\phi_x^-(f_x)$ allows flexibility in defining and fitting of nonsymmetrical hysteresis loops. The transposed functions are

$$\begin{aligned} \phi_x^+(f_x) &= \mathrm{sgn}(f_x - \sigma_x) \cdot \alpha_x \log_e\left(\beta_x |f_x - \sigma_x| + 1\right) \\ \phi_x^-(f_x) &= \mathrm{sgn}(f_x + \sigma_x) \cdot \alpha_x \log_e\left(\beta_x |f_x + \sigma_x| + 1\right) \quad (x = a, b, c) \end{aligned} \tag{2.5}$$

In this study, the limiting curves $\phi_x^+(f_x)$ and $\phi_x^-(f_x)$ were fitted to measured major hysteresis curves for each core-leg obtained from the test procedures of [6] (see Appendix A for function parameters). ρ_x was estimated from the slope of measured leg characteristics in the saturated region. The influence of the ascending and descending curve functions on hysteresis behaviour can be seen in Fig. 2.6.

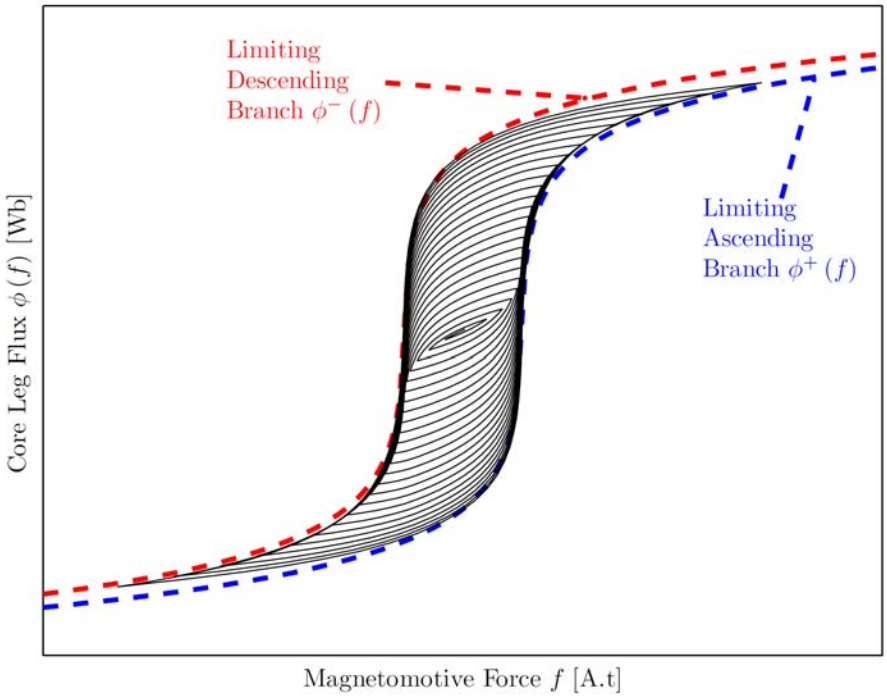

Fig. 2.6. Proposed limiting ascending and descending functions ($\phi^+(f)$, $\phi^-(f)$) for defining hysteresis nonlinearities (Eq. 2.5) in magnetic core legs.

The remaining terms in (2.3) are the slope functions $d\phi_x^{\pm}(f_x)/df_x$ of the ascending and descending loop curve segments for each core leg. These are determined by differentiation of (2.5) with respect to mmf (f_x).

$$\frac{d\phi_x^{\pm}(f_x)}{df_x} = \frac{\alpha_x \beta_x}{\beta_x \left| f_x \mp \sigma_x \right| + 1} \qquad (x = a, b, c) \qquad (2.6)$$

The hysteresis equations (2.3) can now be evaluated for each time step by the

substitution of (2.4)-(2.6). It should be noted that the core-loss resistance R_c in the electric equivalent circuit provides another degree of freedom in influencing the hysteresis loops. In this study, the role of R_c is effectively replaced by the hysteresis functions. Though not the objective here, if so desired, R_c could be adjusted to accurately reflect the breakdown of core losses into their hysteresis and eddy-current components if these can be determined from measurements.

2.2.3 PSPICE implementation of hysteresis nonlinearities

A PSPICE computer program is developed to solve the combined nonlinear hysteresis and electromagnetic circuit equations for the three-leg core (Appendix C). PSPICE is selected due to its robustness in transient analysis and relative ease in defining custom nonlinear models. The nonlinear differential equations are solved numerically by variable time step integration using the Newton-Raphson algorithm. For defining a self-contained modular hysteresis component model, PSPICE's subcircuit feature was employed. Once developed, the subcircuit can be instantiated into any part of the magnetic circuit which exhibits hysteresis. The complete PSPICE electromagnetic circuit model including a detailed exposition of the hysteresis subcircuit mechanism is shown in Fig. 2.7.

The basis for the hysteresis subcircuit is the current source which is controlled by the hysteresis equation (2.3). The mmf drop f_x across the hysteresis subcircuit block is used to compute (2.3) based on (2.4)-(2.6) as previously discussed. At every time step, an "IF statement" selects one of the equations (2.3a) or (2.3b) based on the sign of the induced voltage or the derivative of flux (i.e., whether magnetisation is increasing or decreasing). An arbitrary capacitor-current source circuit loop is implemented to perform the integration of equation (2.3) to compute flux (Fig. 2.7). This approach was found to be more numerically stable compared to using the standard integration function. The current source and capacitor loop equation is

$$i = C\frac{dV_c}{dt} = \frac{d\phi_x}{dt} \text{ where } C = 1 \tag{2.7}$$

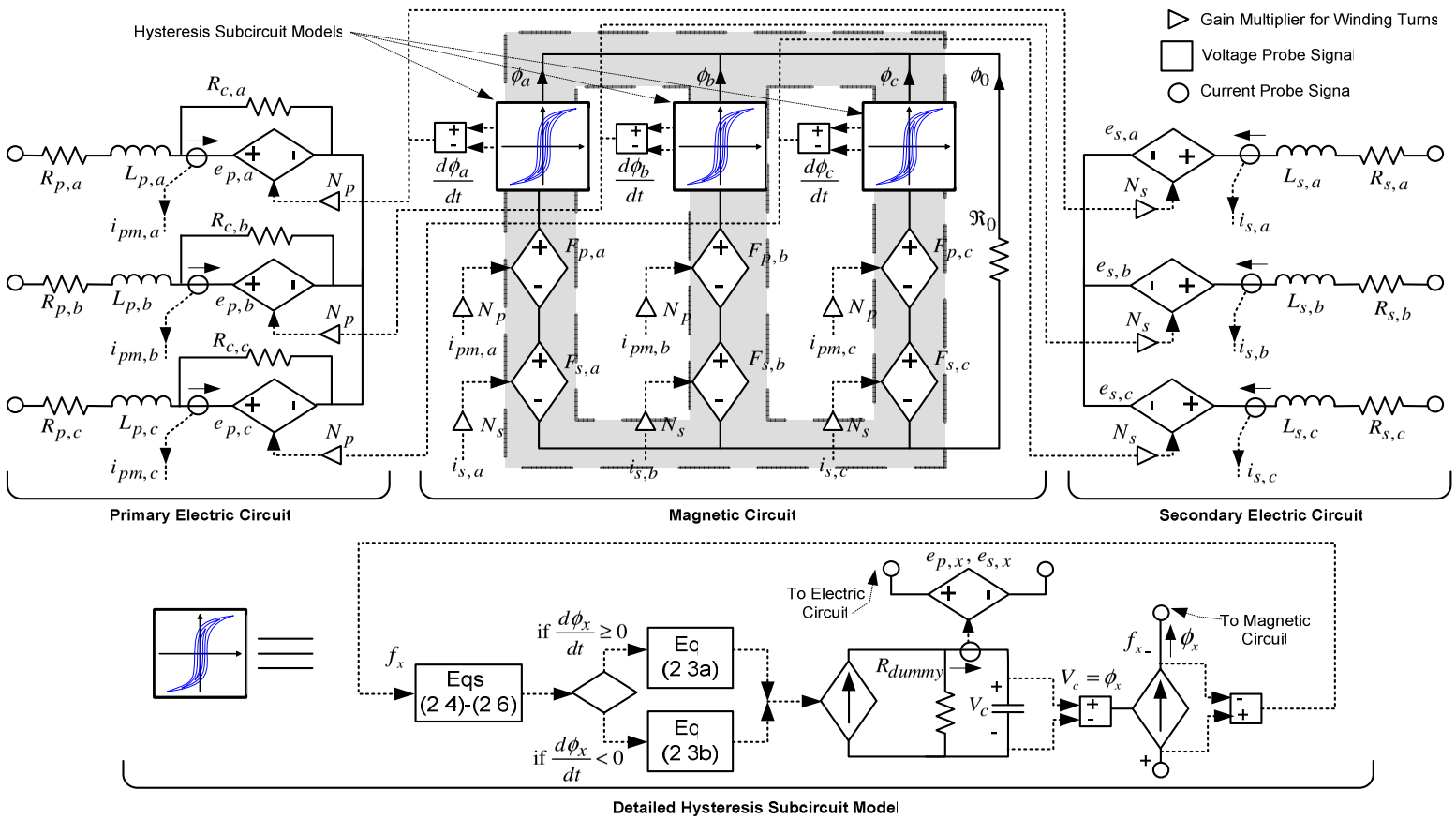

Fig. 2.7. Proposed coupled electromagnetic circuit model for wye/wye three-phase three-leg transformer core with integrated hysteresis nonlinearities. The transformer primary electric equivalent circuit is linked via the magnetic circuit core model to the transformer secondary equivalent electric circuit.

Thus, the voltage across the capacitor directly equates to flux and the capacitor current i is equal to $d\phi_x / dt$ generated by the current source based on (2.3). The capacitor voltage V_c is used to drive a controlled flux (current) source to inject flux into the magnetic circuit for each leg. The capacitor current i also generates the induced phase voltage in the electric circuit (Faraday's Law) via a controlled voltage source. A large resistor (10^{12} Ω) is placed in parallel with the integrator circuit to avoid floating node conditions in PSPICE. This resistance must be large enough to not affect the transformer model behaviour. For this work, three subcircuits in the manner described above are implemented for the three-leg hysteresis nonlinearities. The same subcircuit principles can be used to accommodate other core topologies.

2.3 CONCLUSION

In response to the prevalent need in power research communities for improved dynamic models for carrying out power quality studies, a newly developed time-domain model of a three-phase multi-leg transformer core is proposed in this chapter. While recent advances and technological innovations have led to more flexible power system operations, the corresponding dynamics and stresses imposed on transmission and distribution grids have led to a decline in overall power quality and stability. Hence, there has been a concerted effort in recent years toward improving dynamic models of power components such as transformers. Much like enhanced optics in magnifying glasses reveals finer details in images, improved nonlinear models could potentially allow one to closely examine electromagnetic behaviour in further detail that are otherwise unclear or overlooked with simplified core models.

In the following chapters, the merits of improved nonlinear models in properly diagnosing and predicting transformer performance issues in distorted power networks will be evaluated. For the first time in an integrated manner, the proposed model takes into consideration dynamic magnetic hysteresis effects with major and minor loop formation, asymmetric core structures and magnetic cross-coupling of the legs. New nonlinear mathematical formulations have been developed to effectively

characterise magnetic hysteresis behaviour in multi-leg transformer cores. The modelled hysteresis nonlinearities are integrated for the first time into the magnetic circuits for iron-core structures based on the electromagnetic duality principle.

The proposed electromagnetic model is a departure from previous works that largely take on a single-phase per-phase assumption not considering multiple fluxes and coupled hysteresis nonlinearities interacting under three-phase excitation. Furthermore, the model is based on modular subcircuit implementation for hysteresis nonlinearities which is designed to be easily customisable for other applications and magnetic circuits.

In subsequent chapters, the validity of this model in predicting several transient and steady-state disturbances will be evaluated through a series of extensive simulations and experimental testing with a three-phase three-leg transformer core. The consequences of ignoring three-phase transformer core effects as well as oversimplifying core nonlinearities in models will be examined in detail. Furthermore, new applications of this model will be presented for its usefulness in predicting several destructive power quality disturbances and transformer stress effects (e.g., aging).

Chapter 3. Influence of magnetic hysteresis on no-load and inrush currents in three-phase transformers

3.1 INTRODUCTION

In the previous chapter, a newly developed and improved three-phase multi-leg transformer model was proposed for electromagnetic transient and steady-state studies of transformer operation. One of the main features of this model is the inclusion of magnetic hysteresis nonlinearities for each of the core-legs in the magnetic circuit of the transformer core. In this chapter, the impacts of hysteresis nonlinearities on the formation of no-load magnetisation and inrush currents as well as the consequences of ignoring such effects are examined with the developed transformer model. Simulation and experimental tests are performed to study inrush current waveforms subjected to different initial conditions as well as comparing the effect of traditional single-value non-hysteresis models versus the proposed hysteresis based three-phase transformer model.

3.2 EXPERIMENTAL VALIDATION AND SIMULATION RESULTS

Laboratory tests and simulations are performed to test the validity of the developed model and demonstrate impacts of magnetic hysteresis on no-load and inrush current behaviour. The laboratory setup consists of a dry-type three-phase three-leg transformer apparatus with rated primary and secondary voltages of $440\sqrt{3}$ V and $55\sqrt{3}$ V (10 A), respectively, operated at 50 Hz. The transformer is supplied from a variable three-phase power source using an autotransformer. Excitation currents and voltage waveforms were captured on two synchronised digital oscilloscopes and

processed on a computer. The transformer is connected in wye-G/wye configuration for three-phase no-load and inrush current tests.

3.2.1 Core identification

Magnetic leg hysteresis characteristics for fitting model parameters Eqs. (2.3)-(2.6) were determined using procedures developed in [6]. Each phase of the low voltage winding was separately excited with single-phase voltages up to twice the rated voltage and the exciting currents and induced secondary voltages waveforms were recorded digitally. The corresponding hysteresis loops ($\lambda_p - i_{ex}$) are computed by integrating the induced voltages and the limiting hysteresis curve functions were fitted to the measurements of the core-leg hysteresis loops.

3.2.2 Impact of hysteresis on no-load currents

Steady-state no-load excitation currents and hysteresis loop formation for the three-leg transformer is examined. In the first case, the transformer phase windings are separately excited with single-phase excitations such that magnetic coupling of the phases is suppressed (Fig. 3.1). In the next case, full magnetic leg coupling is enforced by subjecting the transformer to three-phase excitation (Fig. 3.2). Both cases are performed with and without the developed hysteresis model and are excited at twice the rated voltage to emphasise the core nonlinearity for experimental validation. For comparison, the non-hysteretic core model makes use of the nonlinear single-value function of (2.4) for each leg (essentially setting the hysteresis loop width to zero).

Results show that the measured single-phase excitation tests for magnetising current and hysteresis loops can be accurately reproduced in simulations. In particular, the hysteresis model improved the accuracy near the zero-crossings. The simulated leg hysteresis loops with the proposed model show similar behaviour to the measured hysteresis loops when full magnetic coupling is in effect for three-phase excitation (Fig. 3.2). The small discrepancies are attributed to high sensitivity to small errors introduced by the modelled saturation region that are amplified under

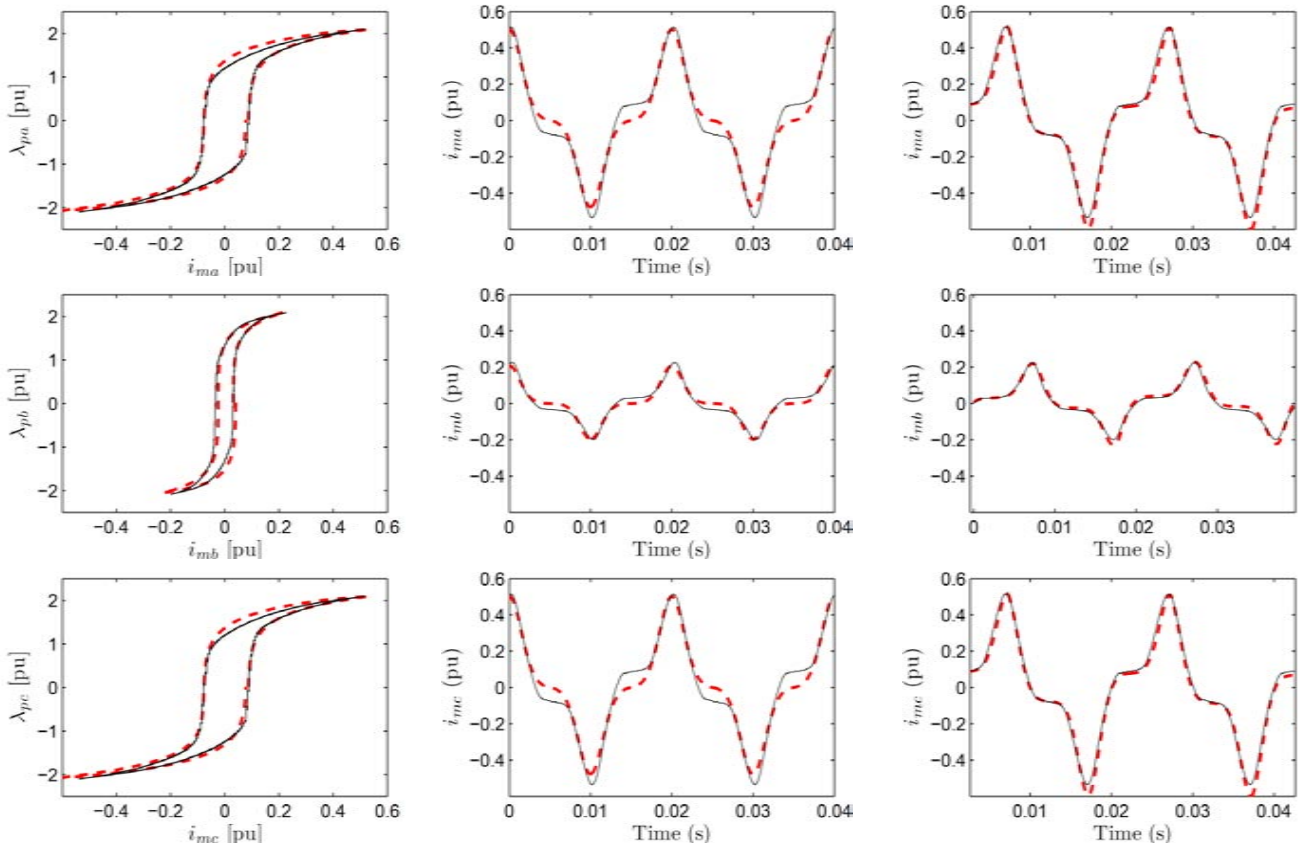

(a) (b) (c)

Fig. 3.1. Single-phase excitation tests (high level saturation) showing in per-unit of rated quantities (a) hysteresis loops, (b) excitation current without hysteresis model (single-value approximation) and (c) with hysteresis model. The dashed (- -) lines are simulations and solid (-) lines are experimental results.

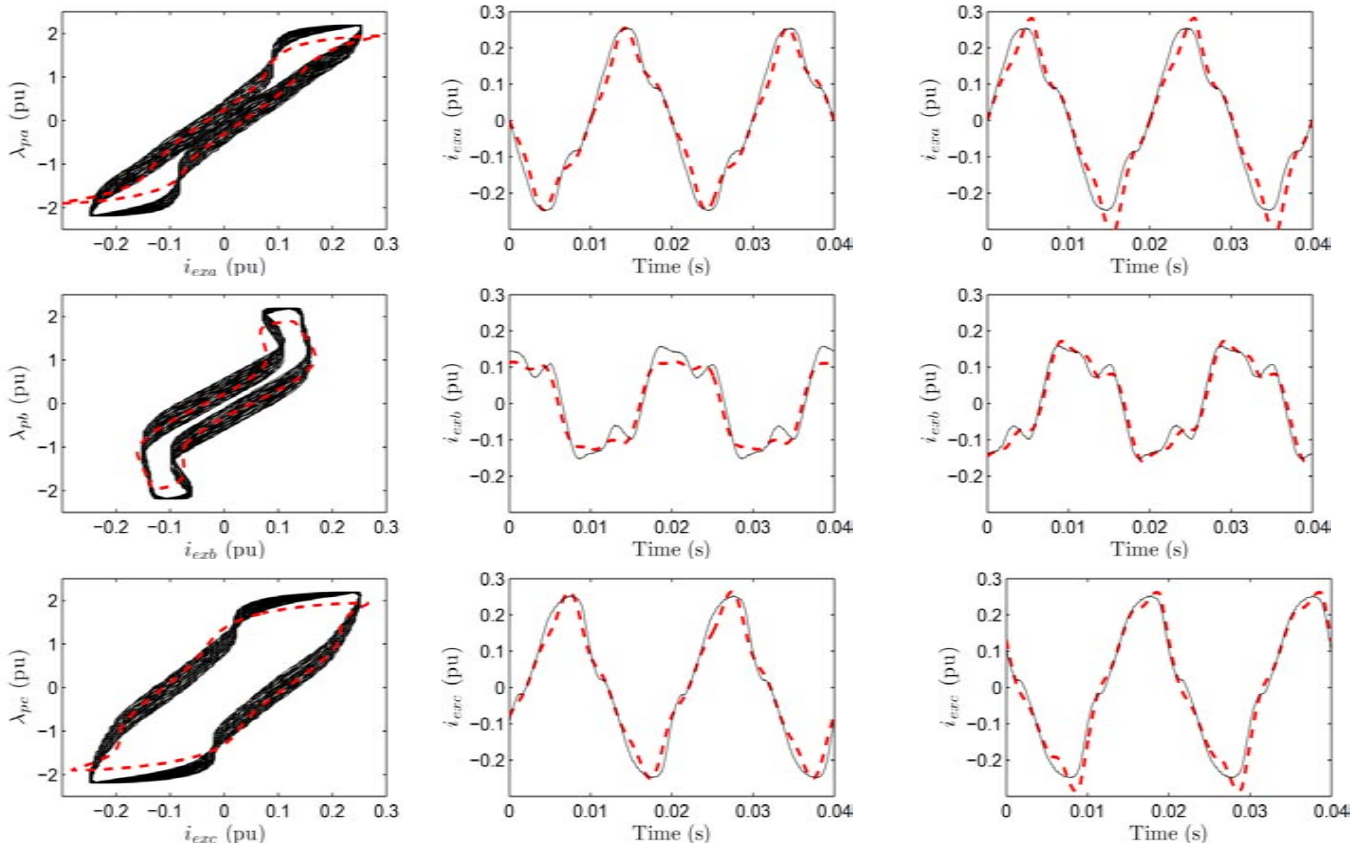

(a) (b) (c)

Fig. 3.2. Three-phase excitation tests (high level saturation) showing in per-unit of rated quantities (a) hysteresis loops, (b) excitation current without hysteresis model (single-value approximation) and (c) with hysteresis model. The dashed (- -) lines are simulations and solid (-) lines are experimental results.

three-phase excitation. Furthermore, the three-phase supply contained small amounts of low order harmonics and slight imbalances which could not be accurately duplicated in simulations. Nevertheless, these results conclusively show that the proposed hysteresis models in each core leg are functioning correctly with proper magnetic cross-coupling interactions taking place within the magnetic circuit.

3.2.3 Impact of hysteresis on inrush currents

Simulations and measurements of inrush currents are performed and compared under different starting conditions to show the significance of including hysteresis nonlinearities in the transformer model. Power transformers typically operate at voltages with corresponding fluxes peaking near the knee-point saturation region of the magnetizing characteristic. At the moment of energisation, the developed core flux can further be driven into saturation resulting in large magnetising currents possibly causing significant voltage dips and malfunctioning protective relays. The models ability to perform under such severe dynamic disturbances and the significant impacts of hysteresis on inrush peak magnitudes and settling times for different starting conditions are examined and summarised in Table 3.1.

Three-phase voltages were applied to the model with rated fundamental magnitude and varying initial voltage phase angle ψ with respect to switching instant. The impact of hysteresis on inrush currents was examined by comparing initial maximum peak current magnitudes (i_{ex}^{peak}) and settling time to half the maximum amplitude (t_{settle}^{min}) with and without hysteresis (Table 3.1). Findings indicate that the inclusion of hysteresis nonlinearities in the modelling of inrush currents results in larger initial peak currents (up to 78% increase) and longer settling times in some of the phase currents compared to results obtained from the single-value non-hysteretic core model. The computed and measured inrush hysteresis formation and magnetising current waveforms for $\psi = 0°$ and $\psi = 90°$ are shown in Figs. 3.3 and 3.4. These results demonstrate the formation of asymmetric leg hysteresis minor loops and diminishing unipolar half-wave peaks for magnetising currents as the inrush dc component decays toward the steady-state condition.

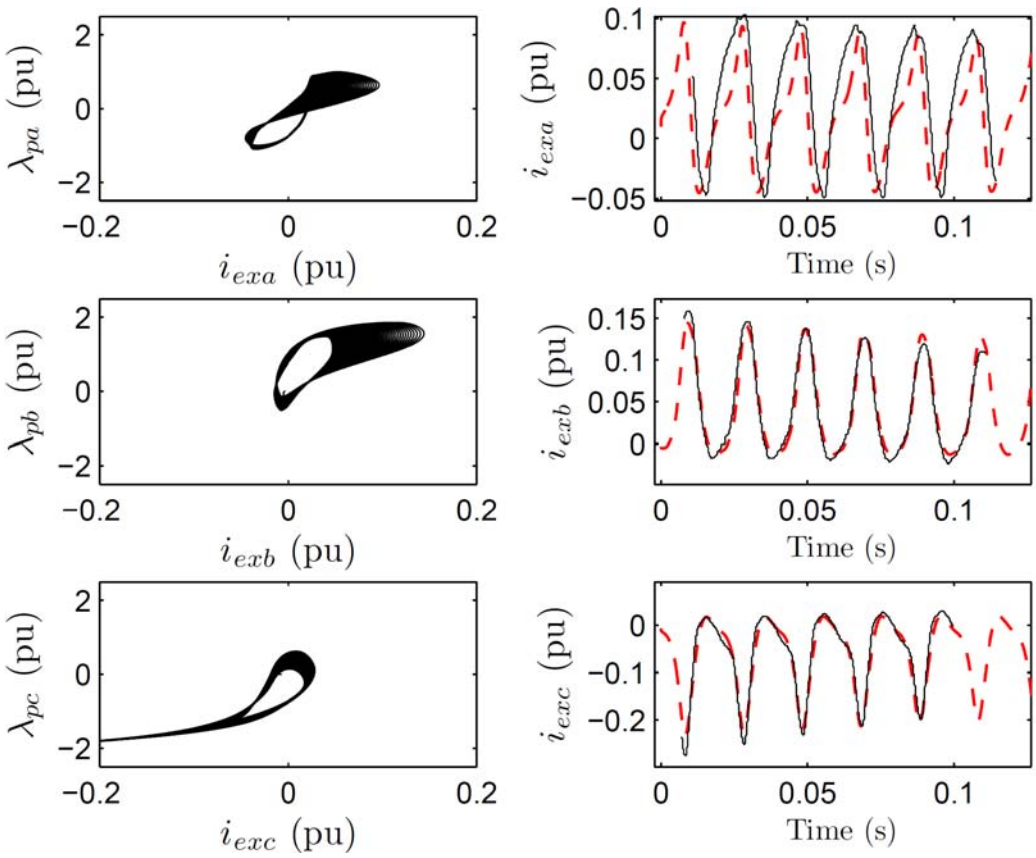

Fig. 3.3. Transformer inrush with starting voltage phase angle ψ = 0°; (a) simulated dynamic hysteresis loop formation, (b) measured (solid line) and simulated (dashed line) magnetising inrush current waveforms in each phase.

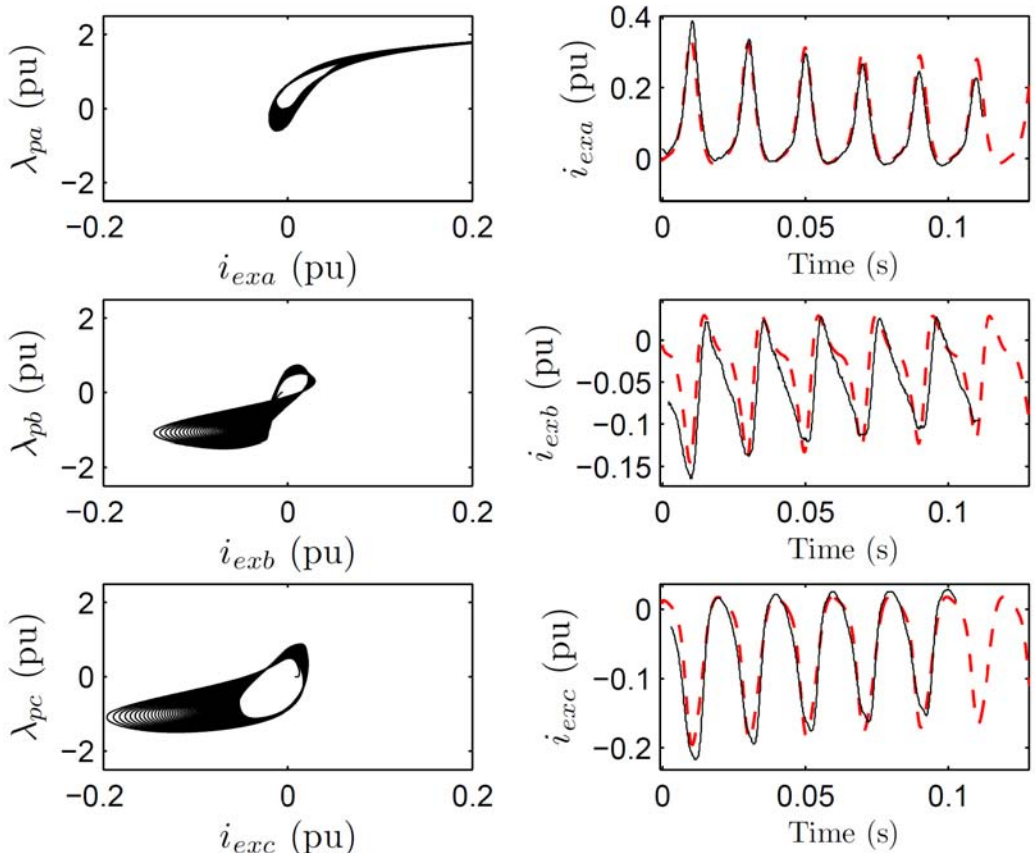

(a) (b)

Fig. 3.4. Transformer inrush with starting voltage phase angle ψ = 90°; (a) simulated dynamic hysteresis loop formation, (b) measured (solid line) and simulated (dashed line) magnetising inrush current waveforms in each phase.

Table 3.1

Impact of hysteresis on initial peak magnitude and settling time of inrush currents at different starting voltage phase angles corresponding to different moments of energisation

		Initial maximum peak of inrush current		Settling time to half the maximum amplitude	
ψ^* (deg)	Phase	$\lvert i_{ex-no\ hys}^{peak} \rvert$ (pu)	$\lvert i_{ex-hys}^{peak} \rvert$ (pu)	$t_{settle-no\ hys}^{min**}$ (A)	$t_{settle-hys}^{min**}$ (A)
0°	a	0.090	0.085	0.79	0.05***
	b	0.128	0.148	0.83	1.19
	c	0.207	0.228	0.77	0.97
45°	a	0.145	0.178	1.11	1.87
	b	0.126	0.126	0.91	1.41
	c	0.054	0.096	1.55	3.50***
90°	a	0.285	0.323	0.55	0.73
	b	0.127	0.124	0.55	0.49
	c	0.156	0.190	0.63	1.01
135°	a	0.169	0.183	0.67	1.13
	b	0.109	0.116	0.57	1.47
	c	0.275	0.254	0.55	0.83
180°	a	0.090	0.066	0.79	1.50***
	b	0.128	0.129	0.83	1.59
	c	0.207	0.191	0.77	1.27

*) initial voltage phase angle influencing the moment of energisation.
**) settling time to half of the maximum peak inrush current amplitude.
***) settling time to steady-state conditions (for final amplitudes greater than half of the maximum peak amplitude).

3.3 CONCLUSION

In this study, the effectiveness of the proposed three-phase transformer model in reproducing steady-state and transient current effects such as no-load and inrush current conditions has been explored. Model based simulations have been compared with experimental results obtained from a laboratory three-phase test transformer in order to verify the validity and accuracy of the proposed model. The main conclusions of this analysis are:

- Comparisons of simulated and measured no-load transformer current waveforms including hysteresis loops (single and three-phase excitations) confirm the correct operation of the proposed model (Figs. 3.1-3.2). The small discrepancies are due to the high sensitivity to small errors introduced by the modelled saturation region and omission of imbalances and harmonic magnitude differences in each phase that could not be accurately measured with the available equipment.
- The proposed three-leg magnetic core model shows reasonable accuracy under dynamic excitation as shown by comparisons of simulated and measured inrush current waveforms with different starting voltage conditions (Figs. 3.3-3.4).
- For a variety of point-on-wave starting voltage conditions, the inclusion of hysteresis nonlinearities and core asymmetry are shown to impact inrush behaviour by significantly increasing initial peak current amplitudes (up to 78% increase) in some of the phases (Table 3.1, cols. 3-4).
- For most of the observed inrush current waveforms, the settling time of dc offset with hysteresis nonlinearities is considerably longer compared to results obtained with the single-value non-hysteretic core model (Table 3.1, cols. 5-6).
- The proposed hysteresis limiting ascending and descending curve functions with two fitting parameters (α, β) are a trade-off between simpler parameter evaluation from measurements, model complexity and precision. There is flexibility in the model and potential for improved performance by permitting more accurate (and complex) mathematical representation of limiting hysteresis curves provided

their functions are differentiable as required by the hysteresis models.

- The proposed method of defining hysteresis nonlinearities as subcircuit components in circuit simulation software is general and could be expanded for the study of inrush currents in other electrical machines based on their magnetic circuit topologies (e.g., four-leg and five-leg transformer cores, induction machines).
- The presented findings and model are applicable to protection design where a more realistic evaluation of transformer stress from inrush and transient current behaviour is required for overcurrent and differential relay coordination. Furthermore, the developed core model could potentially improve accuracy in steady-state (e.g., (non)linear loading, dc biasing and harmonic distortion) and dynamic (e.g., ferroresonance) conditions that will be further examined in following chapters.

Chapter 4. Impacts of hysteresis and magnetic couplings on the stability domain of ferroresonance in asymmetric three-phase three-leg transformers

4.1 INTRODUCTION

Many investigations of ferroresonance phenomena in power and instrument transformers have been performed in the past, spanning nearly a century of accumulated research [5, 37]. Much progress has been made in the modelling and understanding of single-phase transformer ferroresonance. However, one of the weakest areas in ferroresonance research remains in the modelling of three-phase transformers [38, 39] which is the focus of the investigation in this chapter.

4.1.1 Description of ferroresonance

Ferroresonance is a complex oscillatory interaction of energy exchanged between nonlinear magnetising inductances of ferromagnetic cores and system capacitances (e.g., series compensated lines) [37, 39, 40]. These oscillations manifest as large distorted voltages and currents potentially leading to excessive heating and insulation failure in transformers as well as significant disruptions to power networks [41-48].

Unlike ordinary RLC circuit resonance, oscillations involving nonlinear magnetising inductances can exhibit multiple modes with no definite resonant frequency. These modes typically come in four types. The fundamental mode oscillates at the power system frequency f and usually contains harmonics. The subharmonic mode is periodic and oscillates at $1/n$ multiples of the system frequency (f/n). Quasi-periodic modes exhibit irregular patterns of near periodicity due to incommensurable frequencies nf_1+mf_2 where f_1/f_2 is irrational with integer n and m. These modes are strictly non-periodic and produce a discontinuous frequency spectrum. Chaotic

modes exhibit no periodicity and produce a continuous frequency spectrum resembling broadband noise. Sudden jumps (bifurcations) to different modes are also possible due to gradual system variations and perturbations (e.g., switching transients) [40].

4.1.2 Historical review of ferroresonance research

Ferroresonance research has its origins in ordinary transformer resonance studies performed as early as 1907 [49] (Fig. 4.1). It was not until 1920 that the vernacular 'ferroresonance' was first documented by Boucherot [50] describing the unusual coexisting operating points in a series resistor, nonlinear inductor and capacitor circuit. Much early experience in ferroresonance was gained through extensive field observations when digital computer models and analytical methods were in their infancy. Notable examples are the studies conducted in [51-54] on distribution systems exhibiting ferroresonance with voltage regulation capacitors, and the triggering of ferroresonance in three-phase systems from single-pole switching.

Analytical approaches based on simple graphical solutions were proposed early on [55, 56] to predict particular bifurcations in single-phase ferroresonant circuits. It was not until the late 1980s that significant breakthroughs were made in nonlinear transformer models and analytical techniques. This was largely driven by advancements in computing power and the foundation of nonlinear dynamics and chaos theory which Kieny [57] and Mork [58] first proposed as a suitable framework for ferroresonance study. Henceforth, new useful analytical approaches have emerged (e.g., bifurcation, phase-plane and Poincaré techniques [59-63]) which are now the benchmark for modern ferroresonance analyses.

Toward the end of the 20th century, the study area has branched into four main directions: (i) practical system level case studies [43, 64-66], (ii) ferroresonance identification methods [67, 68] (iii) development of ferroresonance mitigation approaches [69-76], and most prominently, (iv) the improvement of analytical techniques and the modelling of electromagnetic transients in transformers, which is one of the main contribution of this research.

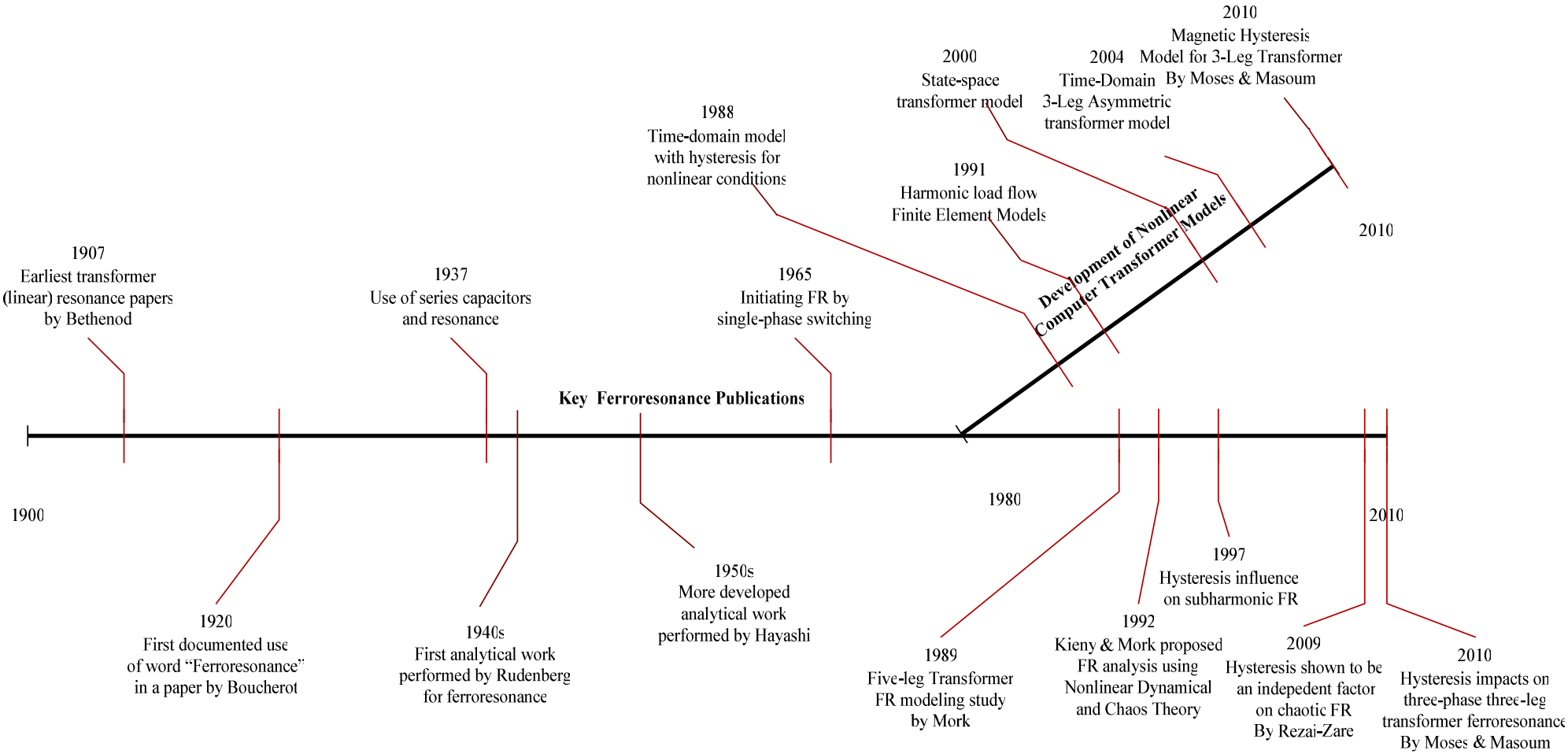

Fig. 4.1. Timeline of key ferroresonance research studies.

4.1.3 Modeling of three-phase ferroresonance phenomena

There have been very few attempts at studying three-phase transformers under ferroresonance conditions. This is owing to the lack of adequate three-phase transformer models and the complexity of many scenarios associated with three-phase switching induced ferroresonance (see Appendix B). References [38, 77-79] implement models considering core topology and employ single-value nonlinear functions for core effects. Analytical and numerical approaches are developed in [80-82] to calculate ferroresonance modes. However, these approaches do not consider dynamic hysteresis effects with core asymmetry and associated magnetic core-leg couplings. Furthermore, these models lack experimental validation.

As previously alluded to, a new class of single and three-phase transformer models is emerging with the inclusion of hysteresis nonlinearities into core representations. Recent studies have shown that accurate representation of ferromagnetic iron-core nonlinearities (e.g., saturation, hysteresis and eddy-currents) is important in ferroresonance. Hysteresis formation significantly impacts the stability domain of ferroresonance, especially for subharmonic and chaotic modes in single-phase transformer core models [9, 10, 13, 14]. The common approach of approximating core nonlinearities with non-hysteretic single-value functions (e.g., piece-wise, exponential and polynomials) has proven to be inadequate for ferroresonance studies in single-phase transformers. The impacts of dynamic hysteresis nonlinearities (e.g., major and minor loops) and magnetically coupled asymmetric legs on three-phase transformer ferroresonance have not been explored.

For the first time, this work studies ferroresonance in asymmetric three-phase transformers using a newly developed and detailed nonlinear electromagnetic circuit model for multi-leg transformer cores. A variety of analytical techniques from nonlinear and dynamics chaos theory are invoked for this study. Experimental validation tests are performed with a laboratory test setup of a three-phase transformer with capacitor switching to demonstrate the models high accuracy in duplicating ferroresonance behaviour in three-phase transformers.

4.2 FERRORESONANCE SYSTEM CASE STUDY

The ferroresonance study in this work is performed for an unloaded wye/wye three-phase three-leg transformer supplied by a three-phase source (Fig. 4.2). The transformer primary and secondary windings are rated at 440 and 55 V (10 A), respectively, and operate at a nominal frequency of 50 Hz. The ferroresonance circuit consists of series and shunt capacitances interacting with the magnetising inductances of the wound transformer core legs. The origin of C_{shunt} and C_{series} can typically be from circuit breakers equipped with grading capacitors, shunt and series capacitive couplings in transmission lines (overhead and underground cables), reactive power compensation capacitor banks, and lumped stray capacitances in transformer windings, bushings, bus bars and feeders.

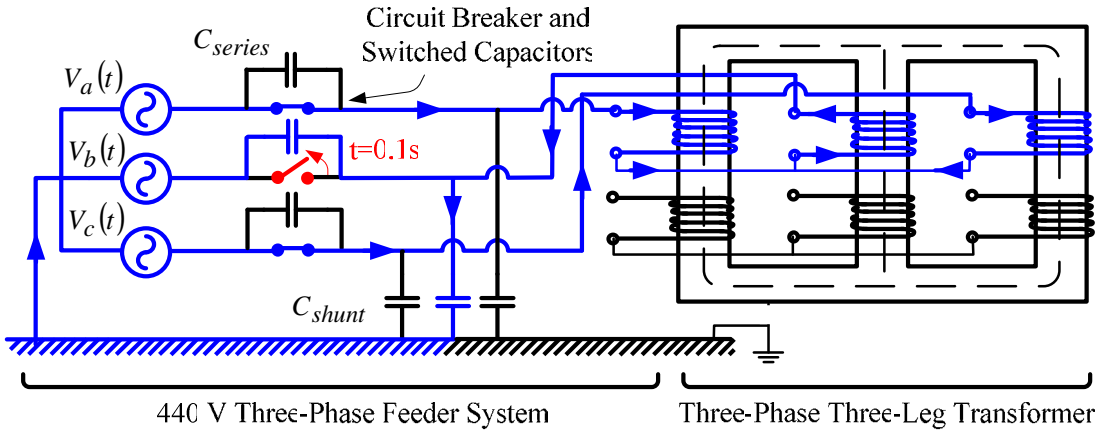

Fig. 4.2. Ferroresonance in an unloaded or lightly loaded transformer fed through series and shunt capacitors (e.g., cable capacitance). The blue lines indicate the ferroresonance circuit path when phase b circuit breaker is suddenly opened (red).

In order for ferroresonance to occur, a system perturbation (e.g., switching transient) with initial conditions conducive to ferroresonance is usually necessary. For the studied system, phase *b* circuit breaker is used to impose switching transients to initiate ferroresonance. There have been many such practical occurrences where unsynchronised three-phase switching or single-phase circuit breaker operations resulted in one or two phases suddenly lost while the transformer is unloaded or lightly loaded, giving rise to ferroresonance [40]. For example, feeders employing

single-phase circuit breakers or fuses can suddenly develop faults causing one or more of the phases to de-energise. The switching transient and resulting unbalanced excitation of the transformer can lead to a ferroresonance path involving magnetising inductances in series with capacitances (see Appendix B). Furthermore, in unloaded or lightly loaded systems (e.g., rural distribution feeders), there may be insufficient system damping to extinguish ferroresonance modes. The resulting large distorted currents and over-voltages have been known to cause severe damage to network equipment including transformers [41-45].

4.3 SIMULATION RESULTS

Detailed time-domain simulation analysis based on the developed three-phase three-leg transformer model is carried out for the system described in Section 4.2. Simulations are performed in PSPICE using the Newton-Raphson numerical algorithm with a variable time step limited to 50 μs. At the start of each simulation, the voltage is ramped linearly from 0 volts to its rated value to reach steady-state conditions and to avoid transformer inrush effects. Ferroresonance considering different combinations of C_{series} and C_{shunt} parameters (Fig. 4.2) with single-phase switching actions are tested. The initial conditions of the system must be considered as they highly influence ferroresonance behaviour. Unless otherwise stated, the reported simulation results maintain the same initial values (e.g., point-on-wave of ac voltage when the circuit breaker is opened, residual fluxes and capacitance charge). At t = 0s, the simulated core is assumed to have zero residual flux and all capacitors have no initial charge. The initial phase angle between the switch opening instant with respect to the phase *a* voltage peak is stated in degrees as ψ.

For selected cases, time-domain waveforms of primary voltages and currents including core leg fluxes are computed. Furthermore, bifurcation diagrams, Poincaré maps, phase-plane trajectories and hysteresis formations are plotted to better analyse the complicated stability domain of ferroresonance modes. In Section 4.4, experimental tests are performed to verify simulated results and model accuracy.

4.3.1 Bifurcation analysis

A useful and effective approach for identifying system parameters conducive to ferroresonance is carried out through bifurcation analysis. The shunt capacitance is chosen as the bifurcation parameter and the primary phase voltages are studied. Tests are repeated for C_{shunt} ranging from 0.1 μF to 10 μF under the same single-phase fault clearing condition.

The bifurcation diagram is constructed from each C_{shunt} parameter change by sampling at the power system frequency (50 Hz) the primary voltage for the open phase *b*. The transient period is ignored in the sampling process to only analyse the subsequent stable ferroresonance oscillations. Poincaré maps [58, 59] are constructed in a similar way by sampling the phase-plane trajectory orbits. The resulting patterns can be interpreted for visual classification of ferroresonance modes [59].

Fig. 4.3 illustrates the existence of multiple ferroresonance modes in the bifurcation diagram based on the developed hysteresis core model. For C_{shunt} = 0.1 μF to 0.5 μF, there is a small jump (bifurcation) in the operating point from normal conditions to fundamental ferroresonance mode. Fundamental ferroresonance mode is shown in Fig. 4.4 for C_{shunt} = 200 pF. The circuit breaker transient is indicated by the large orbit excursions which eventually settle to a stable attracting limit cycle. The distorted noncircular orbit indicates the presence of harmonics in the voltage waveforms.

For C_{shunt} = 3.6 μF, another bifurcation occurs where the transformer enters period-3 type ferroresonance mode as indicated by the branching into a three line trajectory (Fig. 4.3). This mode is stable up to C_{shunt} = 5.5 μF. Simulated time-domain waveforms and hysteresis formation for this mode are shown for C_{shunt} = 4 μF in Fig. 4.5. The voltages, fluxes and currents exhibit highly distorted waveforms reaching in excess of 1.2 pu, 2 pu and 0.4 pu of rated peak values, respectively. The phase-plane trajectory of this mode indicates multiple competing solutions (known as attractors) which influence the trajectory orbits to form subharmonic oscillations.

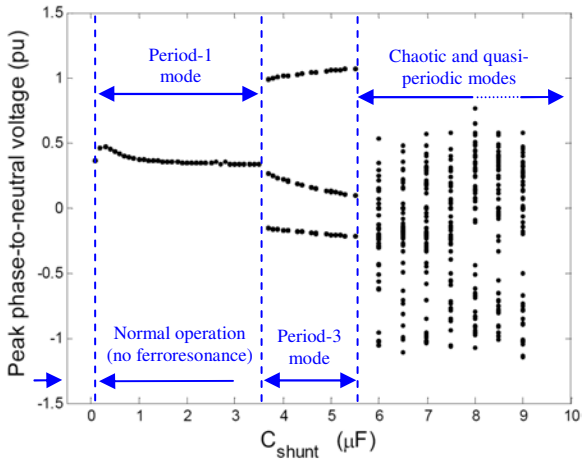

(a)

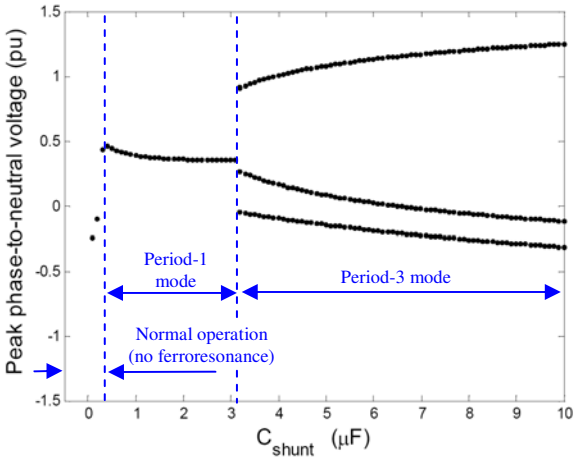

(b)

Fig. 4.3. Bifurcation diagram of ferroresonance modes (phase b voltage) for fixed C_{series} (=30pF) and different C_{shunt} values; (a) considering hysteresis using the proposed three-phase three-leg transformer model and (b) without hysteresis using single-value magnetising curves. Note the absence of chaotic ferroresonance modes and the generation of false period-3 modes in the lower diagram when using single-value (non-hysteretic) core models.

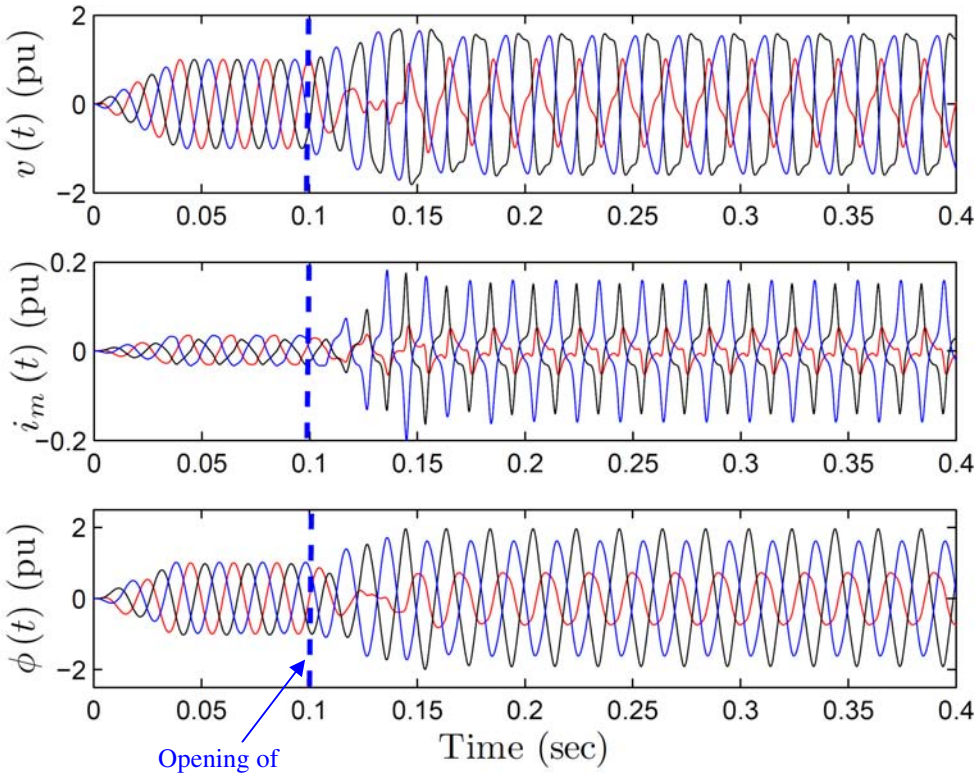

(a)

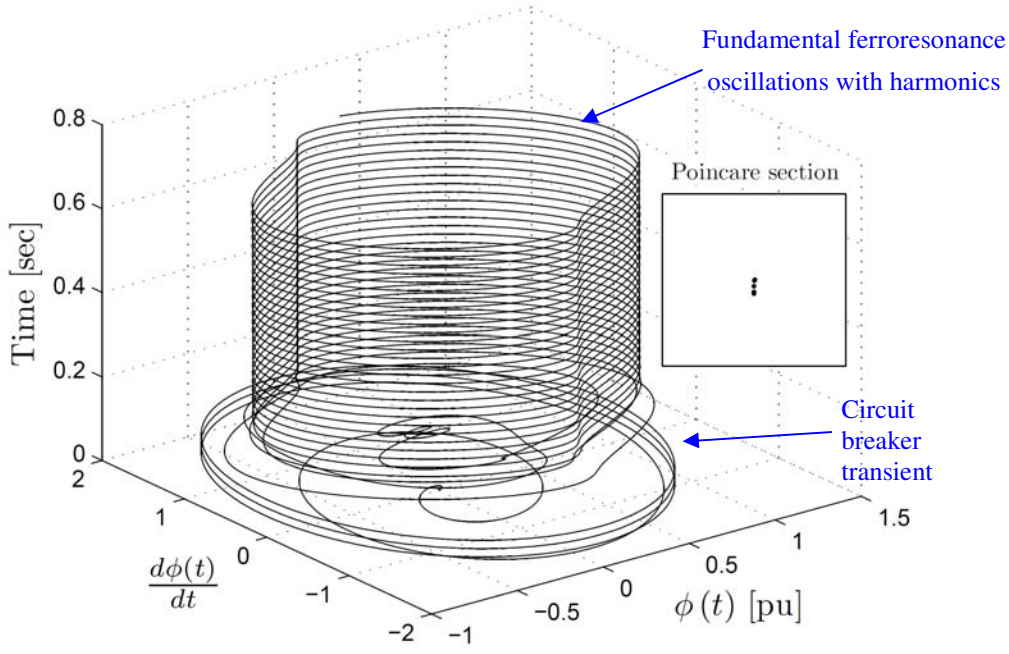

(b)

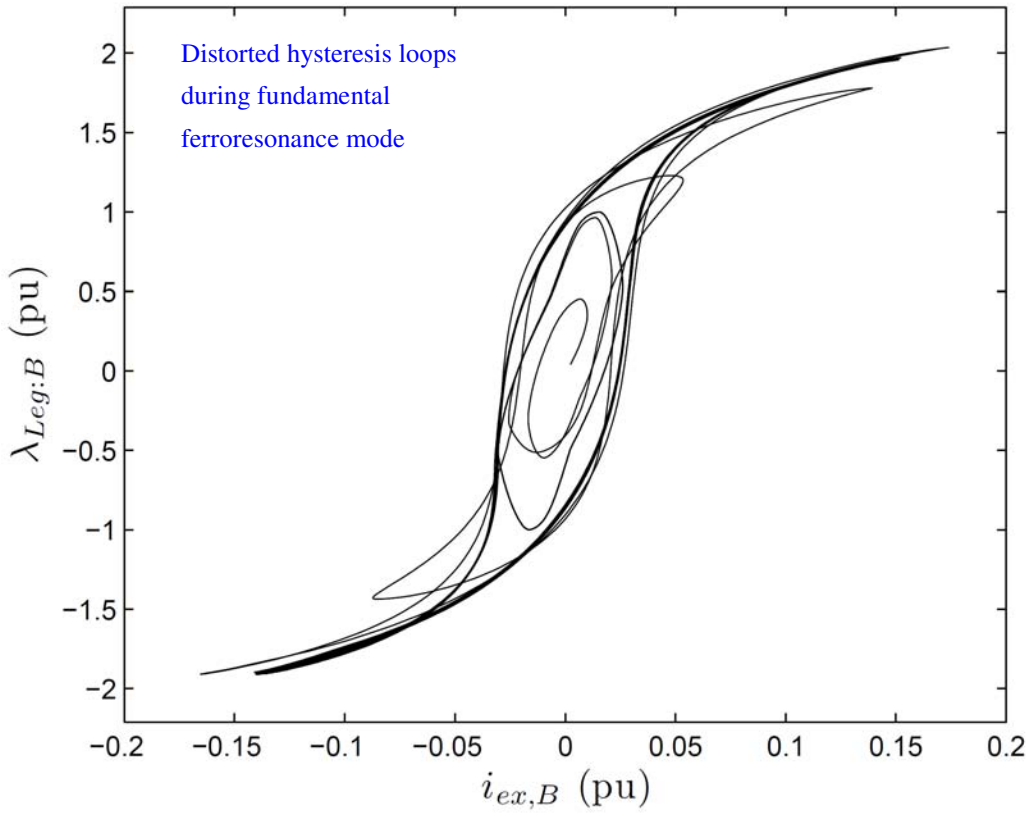

(c)

Fig. 4.4. Time domain waveforms of transformer primary voltages, winding currents and core fluxes for fundamental ferroresonance mode (C_{series} = 200 nF, C_{shunt} = 200pF). (b) Phase-plane trajectory and (c) hysteresis loop (phase b) shows the circuit breaker transient perturbing the system oscillations which then settle to a stable attracting limit cycle. The circuit breaker is opened at an initial phase angle of $\psi = 90°$ w.r.t. peak phase a voltage.

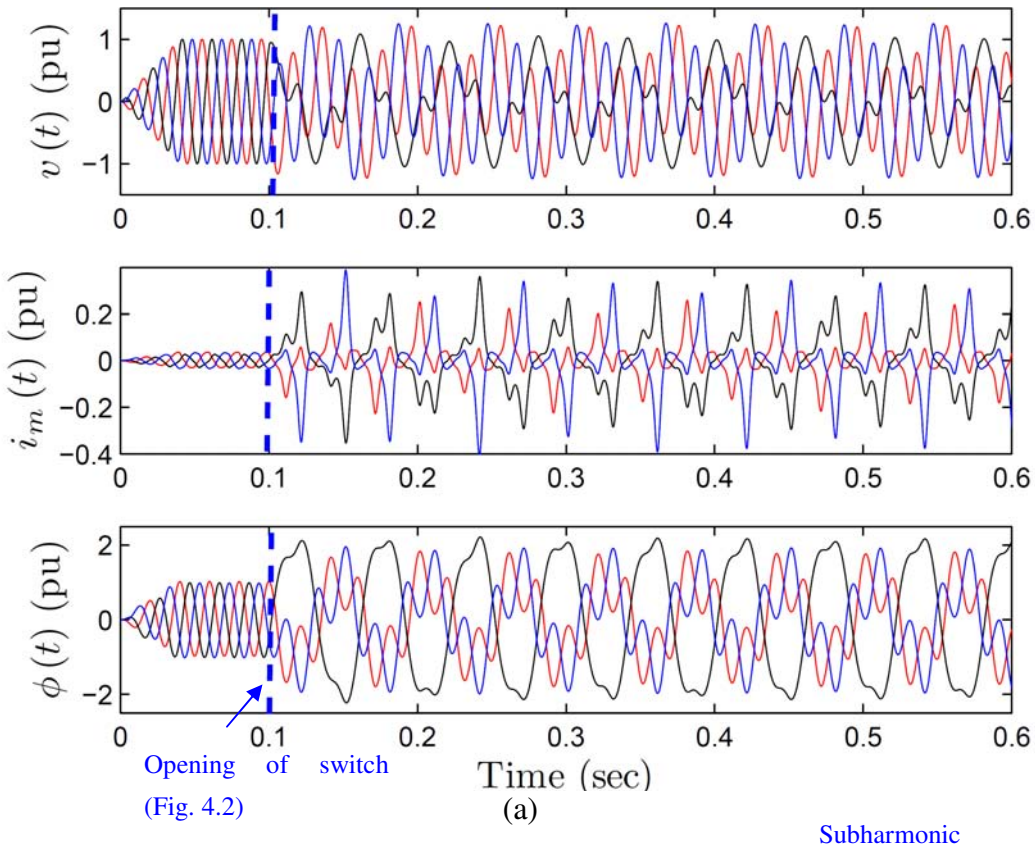

(a)

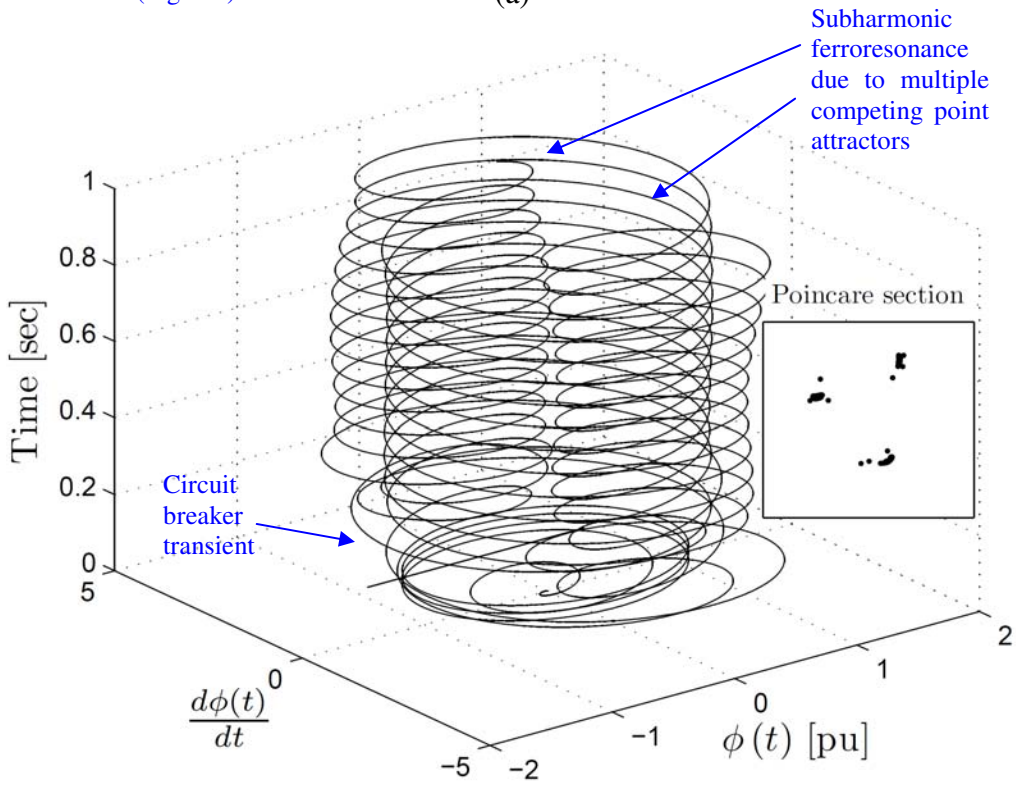

(b)

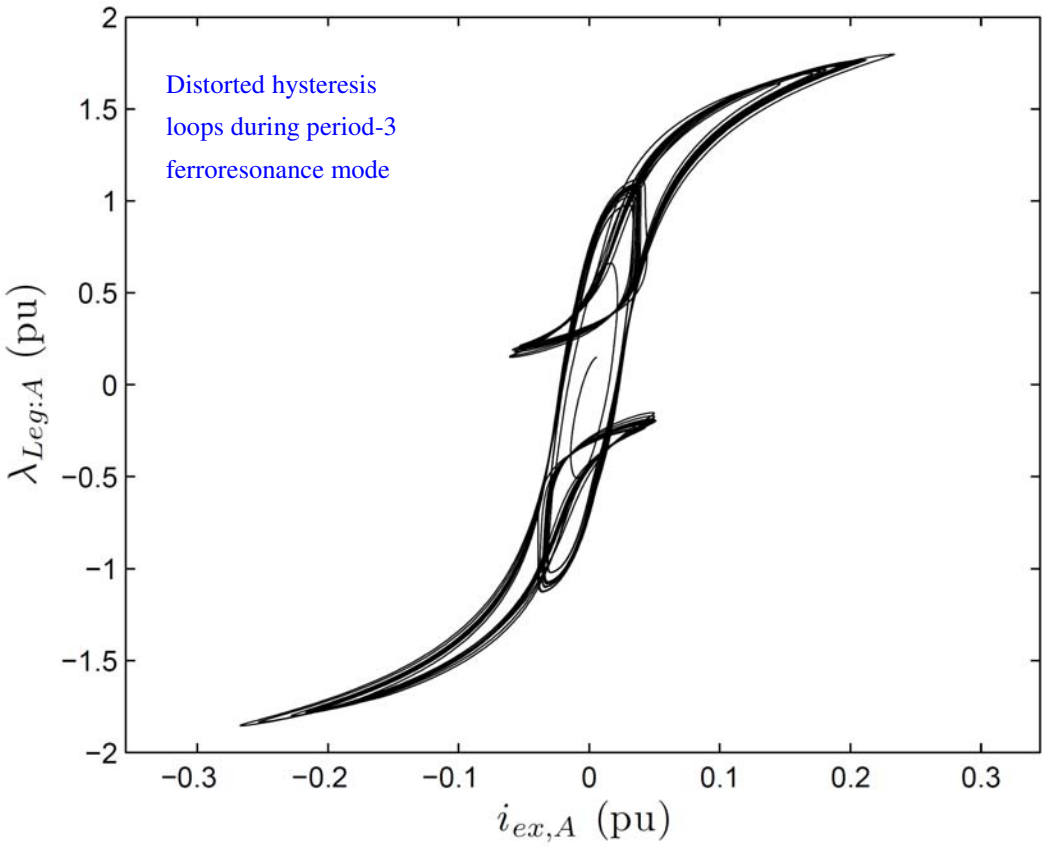

(c)

Fig. 4.5 (a) Time domain waveforms of transformer primary voltages, winding currents and core fluxes for period-3 subharmonic ferroresonance mode (C_{shunt} = 4 μF). (b) Phase-plane trajectory and (c) hysteresis loop (phase a) clearly indicates the transient caused by circuit breaker operation and the existence of competing attractors in the system orbits. The circuit breaker is opened at an initial phase angle of $\psi = 90°$ w.r.t peak phase a voltage.

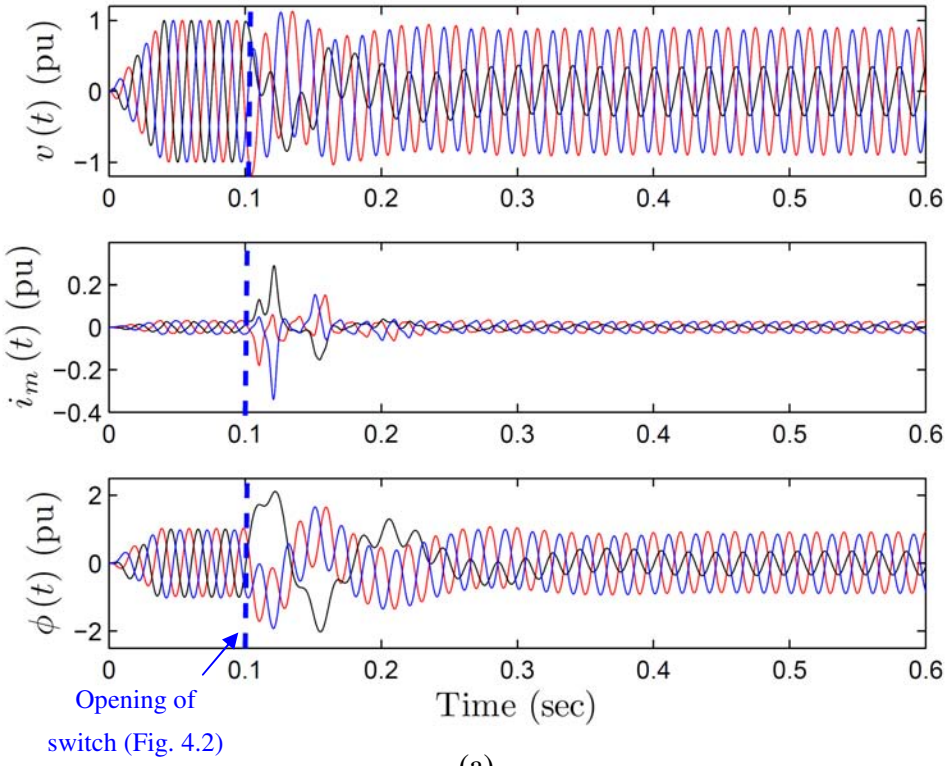

(a)

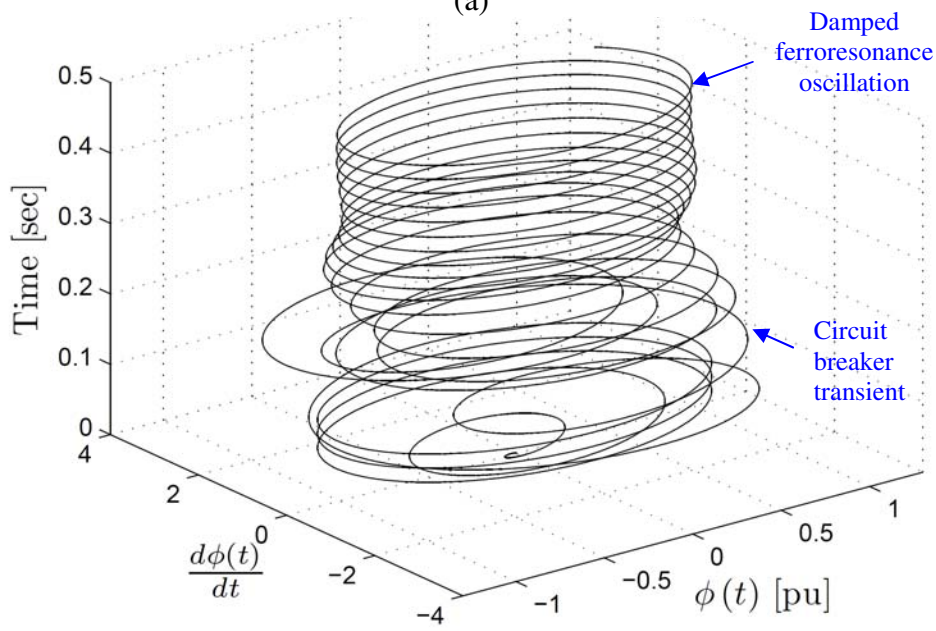

(b)

Fig. 4.6. (a) Time domain waveforms of transformer voltages, winding currents and fluxes for ***unstable ferroresonance***. (b) Phase-plane trajectory indicates the transitory period and damping of ferroresonance in the steady-state. The circuit breaker is opened at an initial phase angle of $\psi = 60°$ w.r.t. peak phase *a* voltage.

Beyond C_{shunt} = 5.5 μF, a bifurcation from period-3 into chaotic ferroresonance modes is detected. This is indicated by the non-repeating structure of the bifurcation diagram corresponding to the sampling of chaotic voltage waveforms. This behaviour is due to the existence of a *strange attractor* in the stability domain.

4.3.2 Sensitivity of ferroresonance to initial conditions

The previous simulation studies have assumed fixed circuit parameters for a varying C_{shunt}. To illustrate the sensitivity of ferroresonance to initial conditions, the circuit breaker opening instant for the previous case (Fig. 4.5) is now changed to $\psi = 60°$. The resulting waveforms and phase-plane trajectories in Fig. 4.6 now indicate a momentary ferroresonant oscillation which loses its stability and dampens out.

4.3.3 Impact of hysteresis on three-phase three-leg transformer ferroresonance

The bifurcation diagram of Fig. 4.3b demonstrates the estimated ferroresonance modes based on a non-hysteretic core model. A single-value nonlinear saturation curve based on (2.4) with zero hysteresis width in each core leg is implemented for the previous case study. The predicted stability domain of ferroresonance is significantly different when compared to Fig. 4.3a. The bifurcation transition into period-3 ferroresonance occurs at a lower C_{shunt} value (3.1 μF) without hysteresis compared to C_{shunt} = 3.6 μF with hysteresis, and extends for a wider range of capacitance. More importantly, when hysteresis is neglected, the model does not detect the chaotic modes and falsely replaces them with extended period-3 subharmonic modes. These findings are consistent with the single-phase transformer study performed in [10] in which chaotic modes were also misrepresented in non-hysteretic core models. The bifurcation diagram of Fig. 4.3a has been confirmed through extensive measurements.

4.3.4 Impact of magnetic couplings on three-phase three-leg transformer ferroresonance

In order to assess the impact of magnetic leg couplings on three-phase transformer ferroresonance, a transformer bank (i.e., three single-phase transformers) was

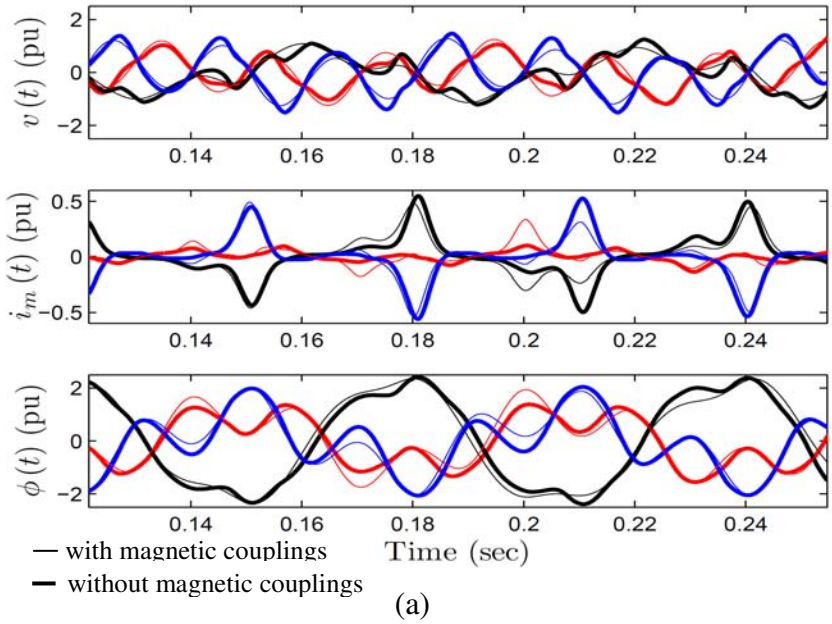

(a)

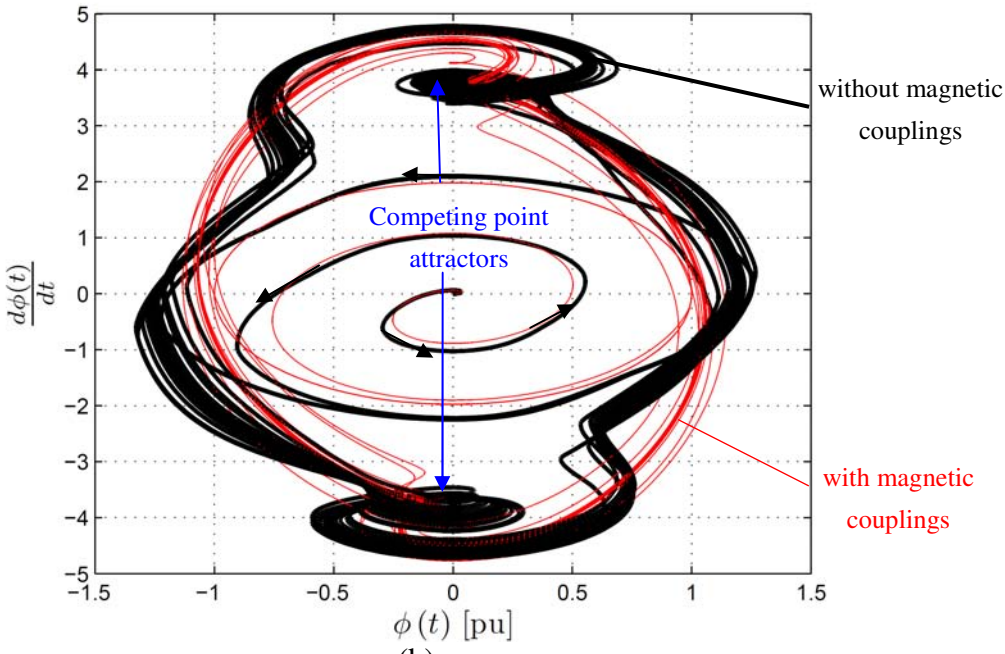

(b)

Fig. 4.7. Comparisons of simulated ferroresonance oscillations for C_{shunt} = 5 µF considering core leg magnetic couplings (thin lines) versus three single-phase transformer bank with no magnetic couplings (thick lines). Time domain waveforms (a) for voltages, currents and fluxes are shown (see Fig. 4.10 for model comparison to measurements) and (b) phase-plane trajectories (drawn in 2 dimensions to highlight differences). Both models indicate period-3 subharmonic modes, however, wave shapes are incongruent and phase-plane trajectories diverge to different orbits.

simulated under the same conditions described in Section 4.2 (Fig. 4.2). This type of transformer has no magnetic core leg couplings because the magnetic cores of each phase are physically isolated. The developed model can approximate this behaviour by setting the zero-sequence reluctance to a very small value, effectively eliminating magnetic leg couplings. The corresponding bifurcation diagram is very similar to Fig. 4.3 (not shown) and similar ferroresonance modes are predicted. However, on closer examination of time-domain waveforms (e.g., C_{shunt} = 5 μF), ignoring inter-phase magnetic couplings results in significant differences in the predicted waveforms when compared to the proposed model (Fig. 4.7). Furthermore, the computed phase-plane trajectories (drawn in 2 dimensions to highlight incongruities) assume different orbit trajectories.

4.4 EXPERIMENTAL RESULTS AND MODEL VALIDATION

Further investigations of three-phase transformer ferroresonance were carried out through experimental tests for the system of Fig. 4.2. The validity of the developed transformer model under ferroresonance conditions is examined by comparing simulations of ferroresonance with measurements obtained from a dry-type three-leg $440\sqrt{3}/55\sqrt{3}$ V laboratory test transformer (Fig. 4.8). The transformer electrical parameters have been previously determined from three-phase open and short-circuit tests. The nonlinear asymmetric core magnetising characteristics were measured by single-phase sinusoidal excitations of each leg. Based on the parameters given in the Appendix, the core models for each magnetic leg closely agree with measured hysteresis loops for a wide range of excitations (Fig. 4.9).

4.4.1 Measurement apparatus and method

The three-phase experimental setup (Fig. 4.8) consists of an autotransformer source, isolation transformers, three single-phase circuit breakers for imposing unbalanced switching transients, capacitor banks and a $440\sqrt{3}/55\sqrt{3}$ V three-phase three-leg transformer. Each circuit breaker has a fixed measured open-circuit capacitance of

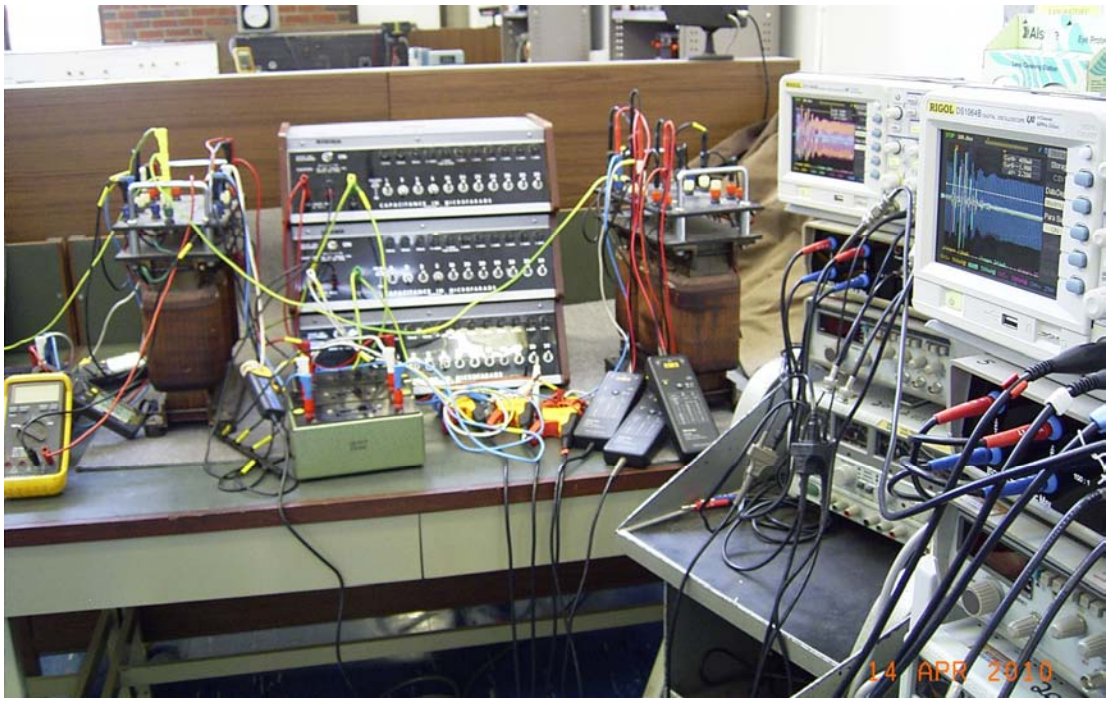

Fig. 4.8. Experimental test setup for ferroresonance measurements. The setup consists of two synchronised oscilloscopes to capture three-phase voltages and currents waveforms, three-phase three-leg isolation and test transformers, single-phase circuit breaker switches and switchable capacitor banks.

approximately 30 pF. The switchable capacitor banks operate in the microfarad range and are connected in shunt arrangement as in Fig. 4.2. Two synchronised oscilloscopes were setup to capture the transformer primary phase-to-neutral voltages and phase winding currents.

In order to obtain good comparisons of measured and simulated waveforms, the initial conditions (i.e., the instant of voltage phase angle the circuit breaker operates) at the onset of ferroresonance must be determined precisely. The slightest phase mismatch can lead to large discrepancies. The two oscilloscopes were triggered simultaneously at the moment of circuit breaker operation to capture initial conditions and subsequent ferroresonance oscillations. Measurements of ferroresonance were obtained with different shunt capacitance values and switching of phase *b* circuit breaker.

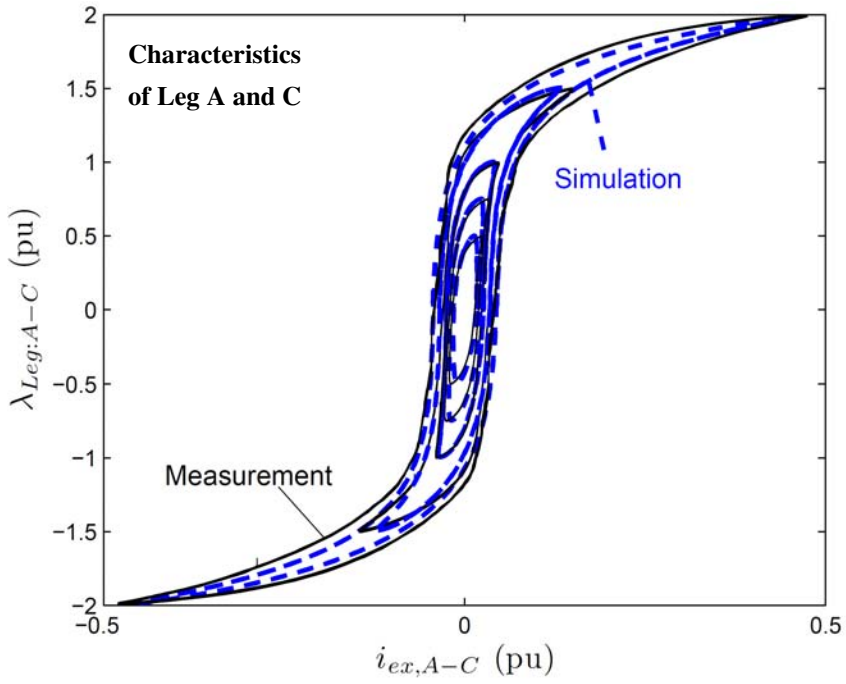

(a)

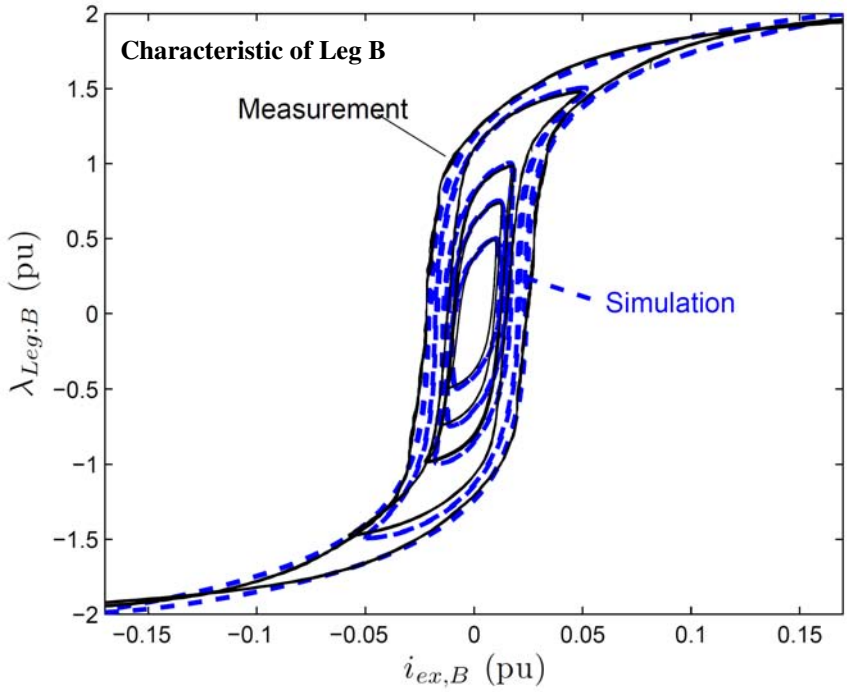

(b)

Fig. 4.9. Measured (solid line) versus modelled (dashed line) core magnetisation hysteresis loops (major and minor) for outer (a) and centre (b) legs at different excitation levels.

4.4.2 Experimental results

Fig. 4.10 displays the measured and model computed period-3 subharmonic ferroresonance modes in the primary voltage waveforms (C_{shunt} = 5 μF). Close agreement is shown for the transition period (bifurcation) from normal conditions to ferroresonance as well as the subsequent steady-state oscillations in all three phases. Note that the wave shapes are not identical amongst all phases. The wave shape of the faulted phase *b* is markedly different to phases *a* and *c*, but is still period-3 mode. This is because the ferroresonance path of the centre leg is not identical to the other legs due to the open phase *b* condition. The centre phase magnetising inductance has a direct path to the shunt capacitance compared to the other two phases (Fig. 4.2). Furthermore, the core is asymmetric because the centre leg (phase *b*) has a shorter flux path length. Since phase *b* winding is open, its voltage is not being supplied by the source, but is developed by induction from magnetic flux couplings of the core.

Comparisons of measured and simulated waveforms for C_{shunt} = 7 μF are shown in Fig. 4.11. It is interesting to note that phases *a* and *c* exhibit subharmonic ferroresonance oscillations while phase *b* waveforms are chaotic. This has not been documented in prior studies. This behaviour is due to the complicated electromagnetic phase couplings in the core. The developed transformer model accurately duplicates this behaviour under the same conditions. Further experimental tests revealed more chaotic modes for larger C_{shunt} values.

Fig. 4.12 depicts the measured and simulated phase voltages and winding currents C_{shunt} = 9 μF. Chaotic ferroresonance modes are observed in phase *b*, however, phases *a* and *c* waveforms resemble period-3 mode but are strictly non-repeating (quasi-periodic). The maximum peak voltage is approximately 1.5 pu for C_{shunt} between 8.0 μF and 9.5 μF. These high overvoltages can degrade winding insulation

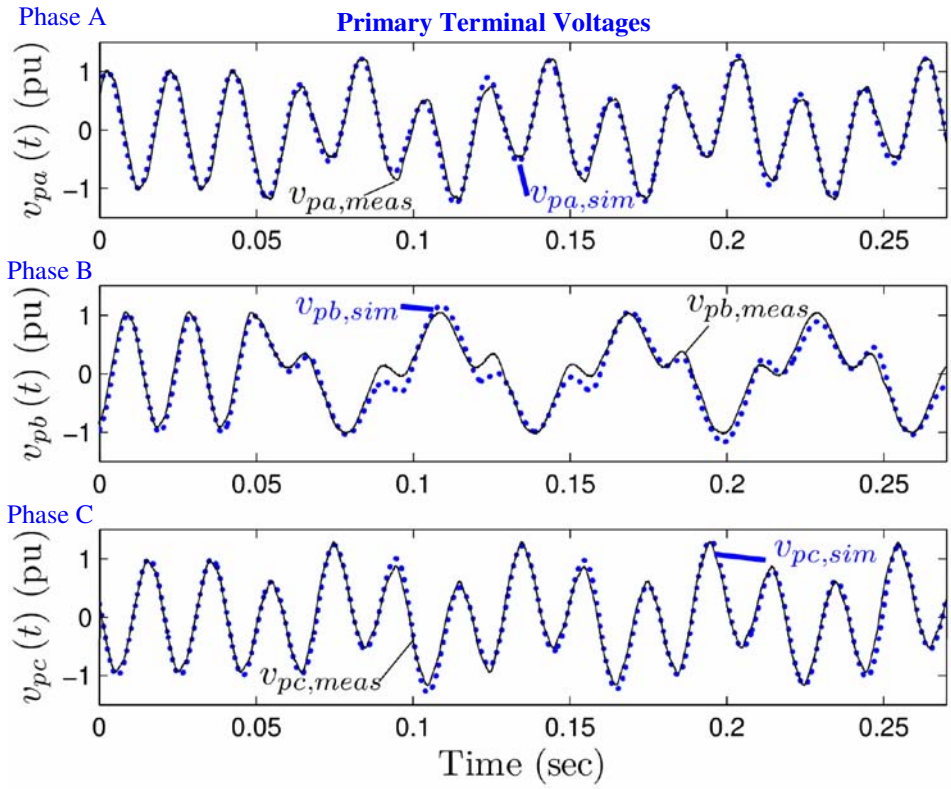

Fig. 4.10. Comparison of measured (solid line) versus simulated (dashed line) ferroresonance oscillations in transformer primary voltage (v_p) waveforms (C_{shunt} = 5 μF). Transition (bifurcation) from normal operation to stable period-3 subharmonic ferroresonance (bifurcation) is shown. The circuit breaker is opened at an initial phase angle of $\psi = -137°$ w.r.t. peak phase *a* voltage.

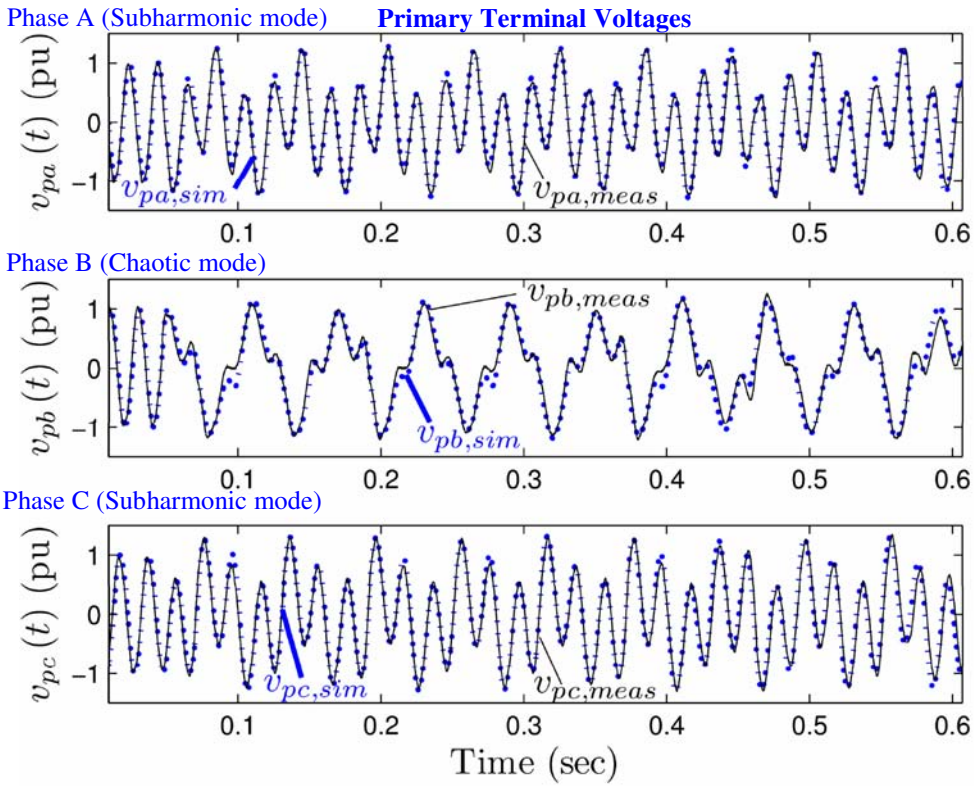

Fig. 4.11. Comparison of measured (solid line) versus simulated (dashed line) chaotic ferroresonance oscillations in transformer primary voltage (v_p) waveforms (C_{shunt} = 7 μF). Stable subharmonic period-3 (phases *a* and *c*) and chaotic ferroresonance oscillations (phase *b*) are shown. The circuit breaker is opened at an initial phase angle of $\psi = -74°$ w.r.t. peak phase *a* voltage.

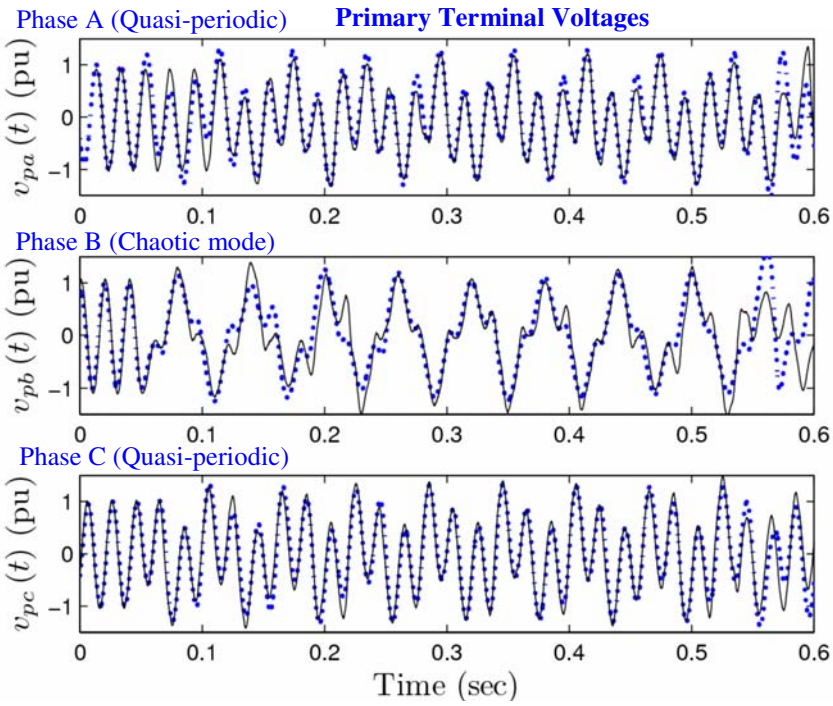

(a)

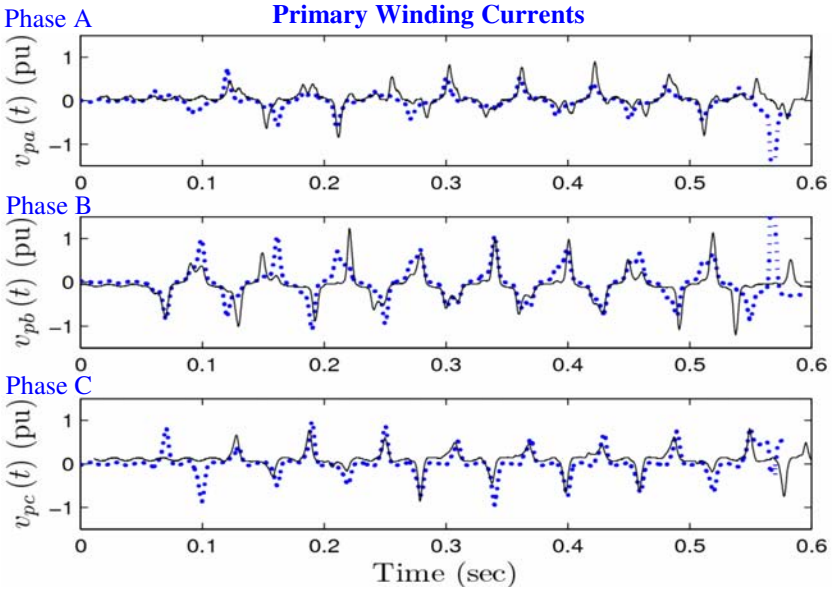

(b)

Fig. 4.12. Comparison of measured (solid line) versus simulated (dashed line) chaotic ferroresonance oscillations for primary (a) terminal voltages (v_p) and (b) winding currents (i_p) for C_{shunt} = 9 μF. The waveforms exhibit chaotic behaviour in phase *b* and quasi-periodic mode resembling subharmonic (Period-3) ferroresonance in phases *a* and *c*. The circuit breaker is opened at an initial phase angle of $\psi = 60°$ w.r.t. peak phase *a* voltage. The errors are due to the sensitivity of chaos to mismatching of initial conditions.

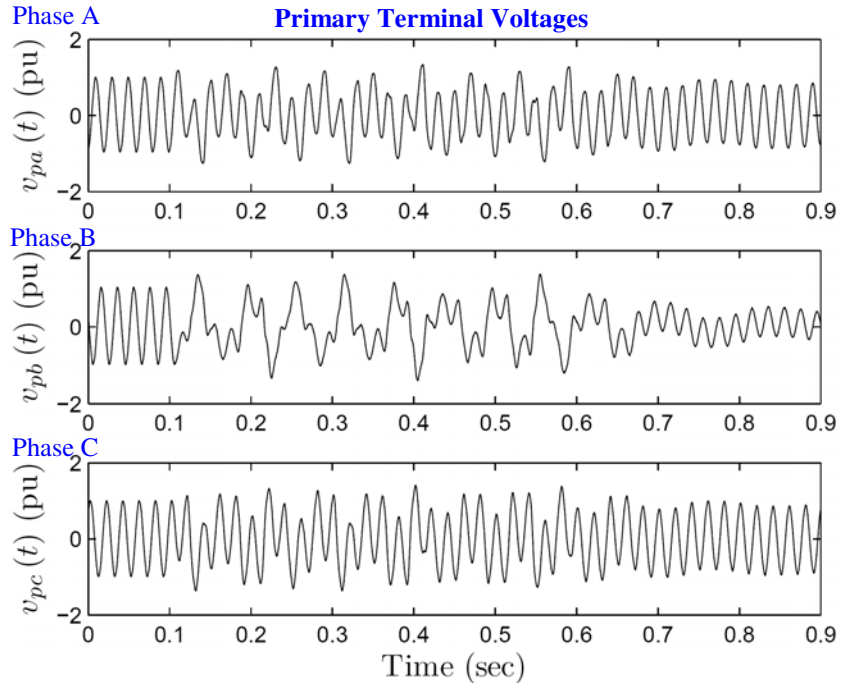

(a)

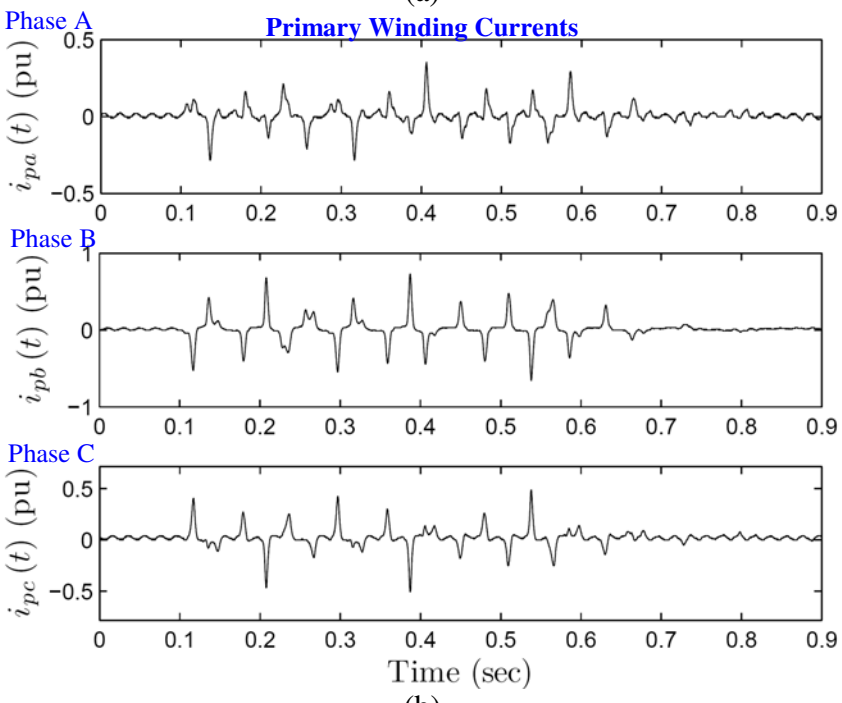

(b)

Fig. 4.13. Measured transformer waveforms for primary (a) terminal voltages (v_p) and (b) winding currents (i_p). The previous case (Fig. 4.12) is repeated for the same C_{shunt} (9 μF) but at a different circuit breaker opening time which results in momentary unstable chaotic ferroresonance. The circuit breaker is opened at an initial phase angle of $\psi = 66°$ w.r.t. peak phase *a* voltage.

Table 4.1
Observed ferroresonance modes and peak phase voltage values:
C_{series} = 30 pF and C_{shunt} = 2 to 10 μF

C_{shunt} (μF)	Ferroresonance Modes*			V_a^{peak}	V_b^{peak}	V_c^{peak}
	Phase *a*	Phase *b*	Phase *c*	(pu)	(pu)	(pu)
2.0	I	I	I	1.16	0.82	1.16
3.0	I	I	I	1.17	1.04	1.29
4.0	III	III	III	1.25	1.17	1.40
5.0	III	III	III	1.20	1.05	1.37
5.5	III	III	III	1.21	1.09	1.37
6.0	III	C	III	1.29	1.30	1.43
6.5	III	C	III	1.35	1.25	1.45
7.0	III	C	III	1.27	1.27	1.40
7.5	III	C	III	1.38	1.35	1.46
8.0	III	C	III	1.45	1.45	1.49
8.5	III	C	III	1.43	1.37	1.49
9.0	Q-III	C	Q-III	1.45	1.43	1.48
9.5	Q-III	C	Q-III	1.40	1.49	1.45
10.0	Q-III	C	Q-III	1.43	1.45	1.45

*) Ferroresonance modes- I: Period-1 fundamental, III: Period-3 subharmonic, Q: Quasi-periodic, C: Chaotic, Q-III: quasi-periodic modes resembling period-3 type ferroresonance.

and cause excessive harmonic distortions and losses. Note that after a few cycles, the simulated chaotic waveforms tend to diverge away from measurements due to sensitivity to small unaccounted for perturbations (e.g., supply harmonics) and differences in initial conditions (e.g., precise switching instant). A summary of the measured ferroresonance modes and peak phase voltages is shown in Table 4.1.

Lastly, the influence of circuit breaker switching time on resulting ferroresonance behaviour was examined experimentally (Fig. 4.13). The case for C_{shunt} = 9 μF (Fig. 4.12) was repeated for a different switching angle with respect to phase *a* voltage peak. By changing the circuit breaker opening instant from $\psi = 60°$ to $\psi = 66°$, the previously stable chaotic modes became unstable and dampened out.

4.5 CONCLUSION

A new analysis into the stability domain of three-phase transformer ferroresonance in multi-leg core structures is presented in this chapter. For the first time, a newly developed three-leg core model considering dynamic leg hysteresis nonlinearities, core topology and asymmetric leg structures is applied to ferroresonance. Extensive experimental tests of transformer ferroresonance have been performed to confirm the accuracy of model predictions. The main conclusions are:

- The study results indicate that the stability domain of ferroresonance modes and electromagnetic oscillations (e.g., voltages, currents and fluxes) are highly dependent on the correct modelling of magnetic couplings and nonlinearities of the iron-core structure.

- Likewise, the magnetic couplings in the legs are shown to significantly impact the accuracy of predicted wave shapes and trajectories of ferroresonance oscillations.

- For the first time, measured and modelled ferroresonance oscillations are shown to exhibit different behaviour in each phase. For particular conditions, chaotic voltage waveforms were observed in the open-circuited phase while exhibiting subharmonic or quasi-periodic modes in the other phases. Therefore, extending per-phase modelling approaches and analysis techniques to the study of three-phase transformer ferroresonance behaviour can lead to incorrect results.

- Predicted ferroresonance modes (e.g., subharmonic and chaotic modes) are shown to be misrepresented in three-phase transformer models that neglect hysteresis nonlinearities (e.g., using single-value functions). False ferroresonance modes and the omission of more severe chaotic modes are shown for non-hysteretic core models.

- The developed three-leg core model correctly predicted ferroresonance modes observed in laboratory tests. Results show that the model duplicates the three-

phase terminal voltage waveforms with high accuracy under transient and steady-state ferroresonance conditions.

- Moreover, for stable periodic modes (e.g., subharmonics), the model accurately predicted their existence for the range of capacitance values observed experimentally. For non-periodic modes (e.g., quasi-periodic and chaotic), the model can reproduce waveforms accurately for a few cycles after the bifurcation point if initial conditions are known precisely. However, due sensitivity of chaos to minute differences in initial conditions (e.g., switching transient) and small unaccountable perturbations (e.g., supply harmonics), long term behaviour under chaotic conditions cannot be predicted.
- The proposed three-leg transformer modelling approach is general and expandable to the study of ferroresonance and other transient disturbances in different electrical machines, transformer types and configurations (e.g., five-leg transformers, induction machines, etc.). The modelling approach is useful for evaluating transformer stresses (e.g., insulation) and testing dynamics of multi-leg core designs.

Chapter 5. Impacts of geomagnetically induced currents (GICs) on balanced and unbalanced dc bias in three-phase transformers

5.1 INTRODUCTION

The occurrence of dc bias in ac power networks has received considerable attention due to its detrimental impact on power quality. Geomagnetic disturbances (GMDs) are the most renowned source of dc bias in ac power systems. The electrical effects of GMDs were first observed in early telegrapher cables before the establishment of power systems [83, 84]. GMDs are associated with solar phenomena such as sun spot and flare activity which cause charged solar particles (solar winds) to interact with the earth's magnetic field producing surface electric fields [32, 37, 85, 86] (Fig. 5.1). During severe geomagnetic storms, these surface electric fields can form in regions with low earth conductivity (e.g., igneous rock geology of the Rocky Mountains) and force geomagnetically induced currents (GICs) through the network via transformer grounding connections. GICs are typically quasi-dc events (0.001 to 0.1 Hz) with magnitudes up to several hundreds of amperes [87]. Severe power system instabilities and blackouts have been attributed to GICs such as those documented in [88-90].

There are, however, other sources of dc bias usually with much less severity than GICs. For example, the employment of electronic switching devices (rectifiers or switched-mode power supplies) can draw currents with large dc components. It has also been shown that the dc earth return currents in HVDC systems can induce dc bias in nearby ac power networks [91-94].

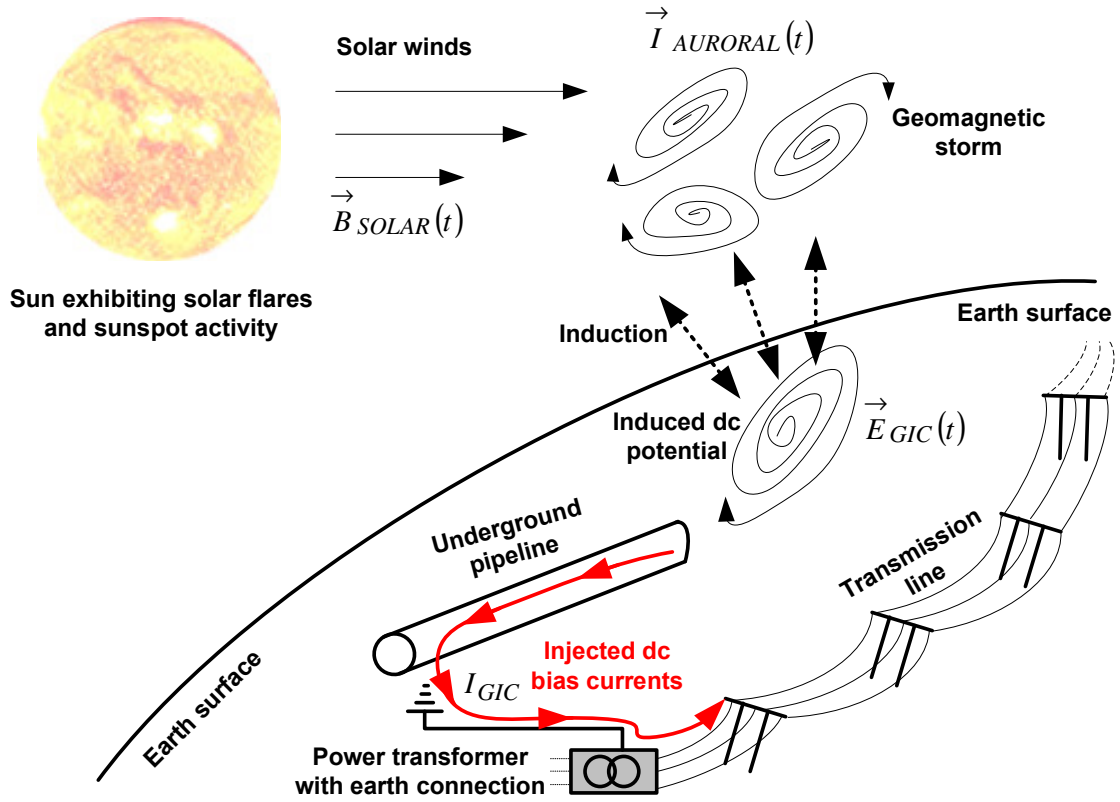

Fig. 5.1. Solar electromagnetic activity (e.g., solar flare and sun spot activity) contributing to geomagnetic disturbances (GMDs) and geomagnetically induced currents (GICs) on the earth surface.

A dc bias can offset magnetic fluxes in ac machines and transformers resulting in a number of serious symptoms such as:

- half-wave core saturation of magnetic fluxes
- increased even and odd current harmonics
- additional fundamental and harmonic frequency power losses
- insulation, windings and core thermal stresses
- mechanical vibrations and sound
- increased reactive power flow
- capacitor overloading
- voltage stability problems
- malfunctioning protection relays.

Three-phase wye-connected transformers with earthed neutrals are particularly susceptible to dc bias. Such configurations are commonly found in step-up/step-down transformers at opposite ends of long distance high voltage transmission lines where GICs have sometimes occurred.

This investigation explores the impact of balanced and unbalanced dc biasing on the harmonic distortions generated by three-phase transformers. Imbalances may arise from poor line transpositions, unbalanced loads and transformer core asymmetry. Preliminary experiments performed in [95] reveals that harmonic distortions in three-phase three-leg transformers can increase significantly if the dc bias currents and developed magnetomotive forces (mmfs) in each phase winding are unbalanced. A related study [96, 97] also experimentally shows the impact of dc bias imbalance on reactive power demand. To date, no theoretical analysis or transformer model considering core asymmetry has been applied to this phenomenon.

The main contribution of this investigation is an exposition of the findings in [95] with full theoretical derivation based on electromagnetic theory. The mechanism behind dc flux imbalance and its impact on transformer operation is demonstrated mathematically and simulated with the developed model. Furthermore, supporting experimental results are presented to study three-phase transformer dc bias. Finally, a method for suppressing dc bias induced harmonics in three-phase transformers is presented. In particular, it is revealed why balancing dc magneto-motive forces in three-leg cores can suppress the dc offsets in flux waveforms and reduce the level of unipolar flux saturation and current distortions.

5.2 THEORETICAL ANALYSIS OF DC BIAS IN THREE-PHASE THREE-LEG TRANSFORMER CORES

Preliminary experiments [95] on a three-phase three-leg transformer for the first time demonstrated that harmonic currents can be suppressed if the applied dc bias in each leg or phase winding is precisely balanced. On the other hand if a small degree of

imbalance exists, large dc fluxes can develop in the legs resulting in increased unipolar saturation as well as even and odd harmonic current generation. Until now, no theoretical explanation or simulation model of this phenomenon has been described in literature. This section presents a new theoretical analysis based on electromagnetic theory to shed some light on the characteristics of this behaviour. It is shown that power system symmetry and phase balance play an important role in the suppression of dc fluxes and harmonics.

5.2.1 Mathematical derivation of magnetic circuit fluxes

The dc bias currents flowing through three-phase transformer windings will generate unopposed dc mmfs in the magnetic legs of three-leg cores. The corresponding impact on developed transformer fluxes is best understood by first deriving the electromagnetic circuit relationships using the approximate equivalent magnetic circuit [6, 35] of a three-leg core as shown in Figs. 2.4 and 2.5. For the moment, calculations can be greatly simplified by assuming that the nonlinear leg reluctances are constants, yielding a system of linear equations that can readily be solved and understood. Thus, the developed leg fluxes in each phase as a function of winding mmf potentials will be derived.

By assigning arbitrary loop fluxes ϕ_1, ϕ_2 and ϕ_3 (Fig. 5.2), mesh analysis can be applied to form the system of linear equations below,

$$\begin{pmatrix} \Re_a + \Re_b & -\Re_b & 0 \\ -\Re_b & \Re_b + \Re_c & -\Re_c \\ 0 & -\Re_c & \Re_c + \Re_0 \end{pmatrix} \begin{pmatrix} \phi_1 \\ \phi_2 \\ \phi_3 \end{pmatrix} = \begin{pmatrix} f_a - f_b \\ f_b - f_c \\ f_c \end{pmatrix} \tag{5.1}$$

where $\Re_a$, $\Re_b$ and $\Re_c$ are magnetic reluctances of the three legs with leakage flux path reluctance $\Re_0$ (which is influenced by the magnetic path provided by air gaps and tank structure). The respective leg fluxes are ϕ_a, ϕ_b, and ϕ_c with zero-sequence leakage flux ϕ_0. The developed leg mmfs are f_a, f_b and f_c, respectively. The relationships between the loop fluxes and leg fluxes are

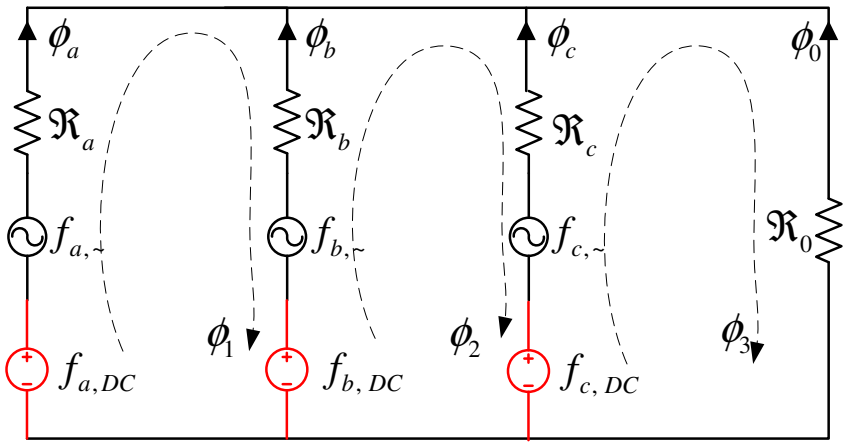

Fig. 5.2. Three-phase three-leg transformer magnetic circuit under dc bias including circulating magnetic fluxes of the iron-core structure.

$$\phi_a = \phi_1, \quad \phi_b = \phi_2 - \phi_1, \quad \phi_c = \phi_3 - \phi_2$$
$$\text{and } \phi_a + \phi_b + \phi_c + \phi_0 = 0 \tag{5.2}$$

Using Cramer's determinant method to solve the system of equations (5.1), the leg flux functions are,

$$\phi_a = \frac{f_a\Re_0\Re_b + f_a\Re_0\Re_c - f_c\Re_0\Re_b - f_b\Re_0\Re_c + f_a\Re_b\Re_c}{\Re_a\Re_b\Re_c + \Re_a\Re_b\Re_0 + \Re_a\Re_c\Re_0 + \Re_b\Re_c\Re_0} \tag{5.3}$$

$$\phi_b = \frac{f_b\Re_0\Re_a - f_c\Re_0\Re_a - f_a\Re_0\Re_c + f_b\Re_0\Re_c + f_b\Re_a\Re_c}{\Re_a\Re_b\Re_c + \Re_a\Re_b\Re_0 + \Re_a\Re_c\Re_0 + \Re_b\Re_c\Re_0} \tag{5.4}$$

$$\phi_c = \frac{f_c\Re_0\Re_a - f_a\Re_0\Re_b - f_b\Re_0\Re_a + f_c\Re_0\Re_b + f_c\Re_a\Re_b}{\Re_a\Re_b\Re_c + \Re_a\Re_b\Re_0 + \Re_a\Re_c\Re_0 + \Re_b\Re_c\Re_0} \tag{5.5}$$

and the zero-sequence leakage flux is

$$\phi_0 = \frac{-f_a\Re_b\Re_c - f_b\Re_a\Re_c - f_c\Re_a\Re_b}{\Re_a\Re_b\Re_c + \Re_a\Re_b\Re_0 + \Re_a\Re_c\Re_0 + \Re_b\Re_c\Re_0} \tag{5.6}$$

5.2.2 Influence of balanced and unbalanced dc leg mmfs

By decomposing the mmfs into their dc and periodic components $f = f_{DC} + f_{\sim}$ and substituting into (5.3)-(5.5), the leg dc flux components $\phi_{DC} = \frac{1}{T}\int_0^T \phi(t)\mathrm{d}t$ as a function of dc leg mmfs in each leg are,

$$\phi_{a,DC} = \frac{f_{a,DC}\left(\Re_0\Re_b + \Re_0\Re_c + \Re_b\Re_c\right) - f_{b,DC}\Re_0\Re_c - f_{c,DC}\Re_0\Re_b}{\Re_a\Re_b\Re_c + \Re_a\Re_b\Re_0 + \Re_a\Re_c\Re_0 + \Re_b\Re_c\Re_0} \tag{5.7}$$

$$\phi_{b,DC} = \frac{f_{b,DC}\left(\Re_0\Re_c + \Re_a\Re_c + \Re_0\Re_a\right) - f_{a,DC}\Re_0\Re_c - f_{c,DC}\Re_0\Re_a}{\Re_a\Re_b\Re_c + \Re_a\Re_b\Re_0 + \Re_a\Re_c\Re_0 + \Re_b\Re_c\Re_0} \tag{5.8}$$

$$\phi_{c,DC} = \frac{f_{c,DC}\left(\Re_0\Re_a + \Re_0\Re_b + \Re_a\Re_b\right) - f_{a,DC}\Re_0\Re_b - f_{b,DC}\Re_0\Re_a}{\Re_a\Re_b\Re_c + \Re_a\Re_b\Re_0 + \Re_a\Re_c\Re_0 + \Re_b\Re_c\Re_0} \tag{5.9}$$

with the dc leakage flux

$$\phi_{0,DC} = \frac{-\left(f_{DC,a}\Re_b\Re_c + f_{DC,b}\Re_a\Re_c + f_{DC,c}\Re_a\Re_b\right)}{\Re_a\Re_b\Re_c + \Re_a\Re_b\Re_0 + \Re_a\Re_c\Re_0 + \Re_b\Re_c\Re_0} \tag{5.10}$$

Equations (5.7)-(5.9) show the dc fluxes in each leg are dependent on interrelated dc mmfs developed in all magnetic branches. In the following, it will be shown how these equations apply to balanced dc biases by forcing the dc mmfs in each leg to be equal

$$f_{DC,a} = f_{DC,b} = f_{DC,c} = f_{DC} \tag{5.11}$$

The dc flux components under applied balanced dc mmfs can then be written as

$$\phi_{a,DC} = \frac{f_{DC}\Re_b\Re_c}{\Re_a\Re_b\Re_c + \Re_a\Re_b\Re_0 + \Re_a\Re_c\Re_0 + \Re_b\Re_c\Re_0} \tag{5.12}$$

$$\phi_{b,DC} = \frac{f_{DC}\Re_a\Re_c}{\Re_a\Re_b\Re_c + \Re_a\Re_b\Re_0 + \Re_a\Re_c\Re_0 + \Re_b\Re_c\Re_0} \tag{5.13}$$

$$\phi_{c,DC} = \frac{f_{DC}\Re_a\Re_b}{\Re_a\Re_b\Re_c + \Re_a\Re_b\Re_0 + \Re_a\Re_c\Re_0 + \Re_b\Re_c\Re_0} \tag{5.14}$$

$$\phi_{0,DC} = \frac{-f_{DC}\left(\Re_b\Re_c + \Re_a\Re_c + \Re_a\Re_b\right)}{\Re_a\Re_b\Re_c + \Re_a\Re_b\Re_0 + \Re_a\Re_c\Re_0 + \Re_b\Re_c\Re_0} \tag{5.15}$$

If an idealised symmetric core is considered, then

$$\Re_a = \Re_b = \Re_c = \Re_{leg} \tag{5.16}$$

and (5.12)-(5.15) can be reduced to

$$\phi_{a,DC} = \phi_{b,DC} = \phi_{c,DC} = \frac{f_{DC}}{\Re_{leg} + 3\Re_0} \tag{5.17}$$

$$\phi_{0,DC} = \frac{-3f_{DC}}{\Re_{leg} + 3\Re_0} \tag{5.18}$$

Equations (5.12)-(5.15) and (5.17)-(5.18) are a special (balanced) case of (5.7)-(5.10). Furthermore, (5.17) reveals that if the zero-sequence reluctance is much larger than the leg reluctances (e.g., large air gap between tank and iron-core), the impact of balanced dc bias currents on dc flux generation is small and should not significantly increase current harmonic distortion. This is in complete agreement with experimental observations of [35, 96] where the influence of tank air gaps was investigated under dc bias.

To further understand the implications of these equations, consider the following examples. In this example, the zero-sequence high reluctance is assumed to be 100 times that of leg reluctances. A symmetrical transformer is assumed with equal reluctances as in (5.16). According to (5.17), if there is a 1% balanced increase in dc mmfs in all three phases, the corresponding leg dc fluxes would increase by the same proportion (assuming linear core conditions).

Now consider unbalanced increases (and/or decreases) in leg mmfs. From the balanced dc bias state, if one of the leg dc mmfs is now increased by 1% and the other leg dc mmfs are kept constant, the corresponding leg dc fluxes change by up to 200% based on (5.7)-(5.9). This is similar to the problem of paralleling three batteries with slightly different terminal voltages. Large currents would flow

between the unbalanced batteries. In the case of a transformer, the unbalanced dc mmfs force large circulating dc fluxes superimposed with ac fluxes through the core structure. The zero-sequence high reluctance path impacts this behaviour significantly. If $\Re_0$ is increased (e.g., by variation of tank design through larger air gaps), the percentage changes (sensitivities) in dc fluxes would further increase. This is expected because the zero-sequence path is the only other path available for imbalance fluxes to flow in three-leg cores. Therefore, limiting this path with a larger $\Re_0$ would otherwise force the dc flux to redistribute itself within the three-leg core.

From this analysis, it is concluded that the generation of dc fluxes in the core-legs is highly sensitive to unbalanced dc biases. However, in practice, even if balanced dc bias currents could be achieved precisely, there is still the problem of inherent core asymmetry, nonlinearity and residual magnetism including hysteresis in the leg reluctances, which are not considered in this mathematical treatment. Thus, these inherently small imbalances can still give rise to small dc fluxes in the legs and increase current harmonic distortion. Therefore, in theory, balancing dc mmfs and the use of symmetric core designs could significantly suppress effects of dc bias (e.g., harmonic currents and reactive power demand).

5.2.3 Transformer models for dc bias

Transformer simulation models for dc bias have been demonstrated for single-phase [98-100] and balanced three-phase transformers [101]. However, the crucial asymmetric multi-leg core behaviour with mutual leg flux interaction is not addressed in dc bias studies. The time-domain computer model of an asymmetric three-phase three-leg transformer as previously described is employed for this study. The electromagnetic equivalent circuits are modified to include dc bias by including an independent dc voltage source placed in situ with the transformers neutral-earth connection to mimic dc bias conditions (e.g., GICs). The model is used to analyse the distortions in voltage, current and flux waveforms under (un)balanced dc bias and verify predicted theoretical findings.

5.3 EXPERIMENTAL AND SIMULATION RESULTS

Measurements were performed on a small-scale laboratory three-phase transmission line system designed for dc bias tests. The setup consists of an autotransformer source, step-up source-side transformer (wye/wye $55\sqrt{3}$ / $440\sqrt{3}$ V), transmission line model, step-down load-side transformer (wye/wye $440\sqrt{3}$ / $55\sqrt{3}$ V) and resistive load network (Fig. 5.3) operating at 50 Hz. The two transformers are of identical types with three-phase three-leg core structures (see Appendix A specifications). Rheostats are used as transmission line and load impedances and are varied as a means of investigating the impact of imbalances in dc biases. For dc biased conditions, the influence of transmission line reactances (e.g., capacitances) is negligible and is therefore omitted from the analysis. Likewise, the measured source impedance of the grid (e.g., $|Zs| \approx 0.62 \pm 0.09$ ohms at the Electrical Machine Laboratory, Curtin University of Technology, WA, Australia) has no noticeable impact on simulations. A laboratory dc power supply is used as a controlled dc bias current source. A Fluke 434 three-phase power quality meter is used to measure the waveforms and harmonics data for the load-side transformer primary (Table 5.1).

5.3.1 Case 1: DC bias and balanced operation

In this test, the transmission line system was configured for nominal balanced operation by setting the line impedances in each phase to be approximately equal (1 Ω per phase). This is deemed sufficient to represent the scaled down cable resistances in a typical transmission line. The load-side transformer serves a balanced wye-connected resistive load (15 Ω per phase). Fig. 5.4 demonstrates primary current waveforms and harmonics for nominal operation with no dc bias input. The total harmonic distortion (THD) of the load-side transformer primary currents and terminal phase voltages range from THD_i = 4 to 5.3% and THD_v = 2.2 to 2.8%, respectively, due to nominal levels of saturation and small supply voltage harmonics.

In order to generate dc bias effects similar to practical situations in power systems (e.g., GICs), a dc supply is connected between the neutrals of both transformers on the high voltage side (Fig. 5.3). The transmission system is operating under the same

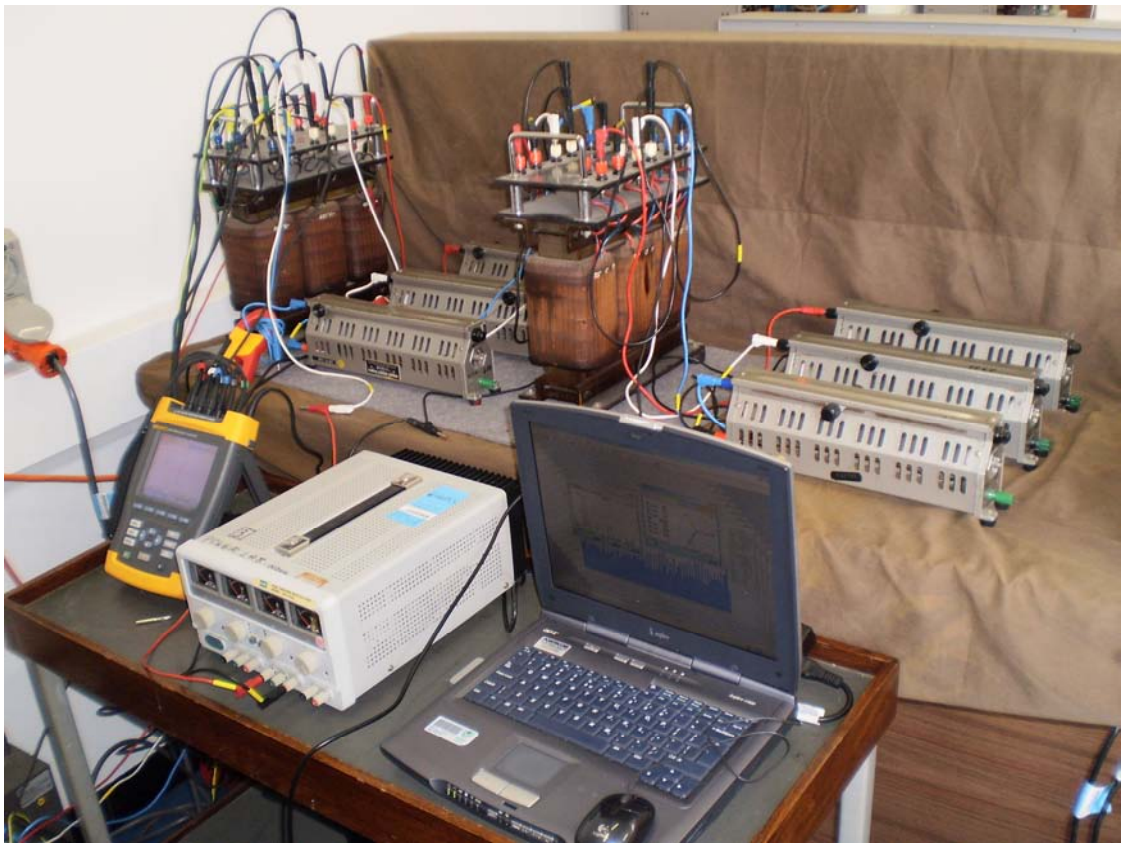

(a)

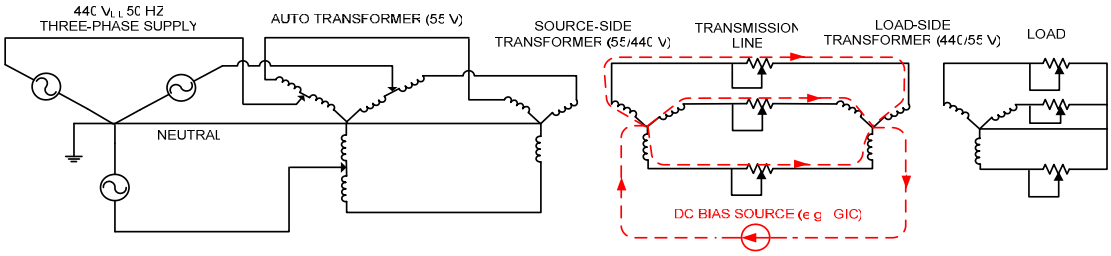

(b)

Fig. 5.3. (a) Experimental setup and network diagram (b) of a three-phase transmission system under dc bias. A dc potential difference can be induced in the ground (e.g., due to GMDs) between earthed neutrals of transformers at opposite ends of long transmission lines. The resulting dc bias current (e.g., GICs) is forced through each phase conductor of the transmission line and transformer windings giving rise to (un)balanced three-phase dc mmfs in the iron core structure. A dc supply is connected between the neutrals of the star windings for the load-side and source-side transformers to inject dc bias currents.

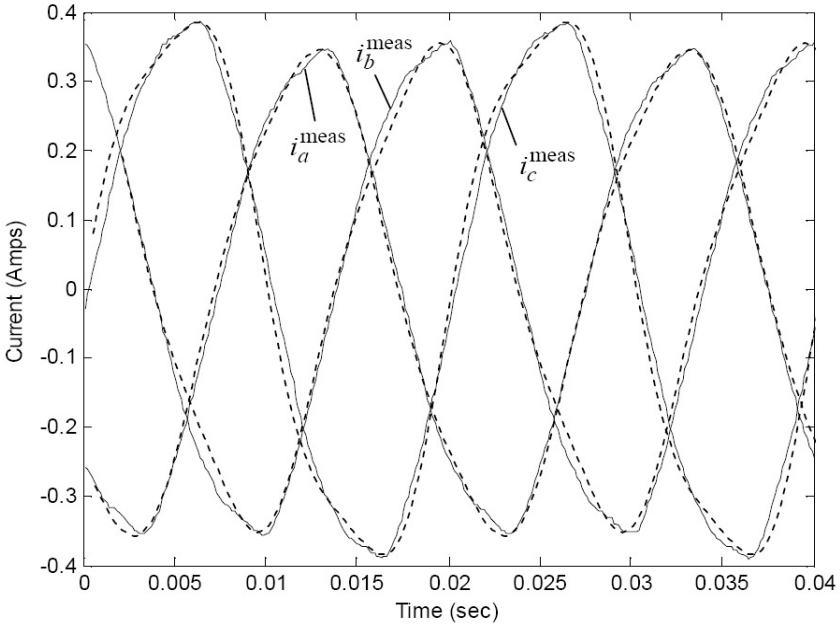

(a)

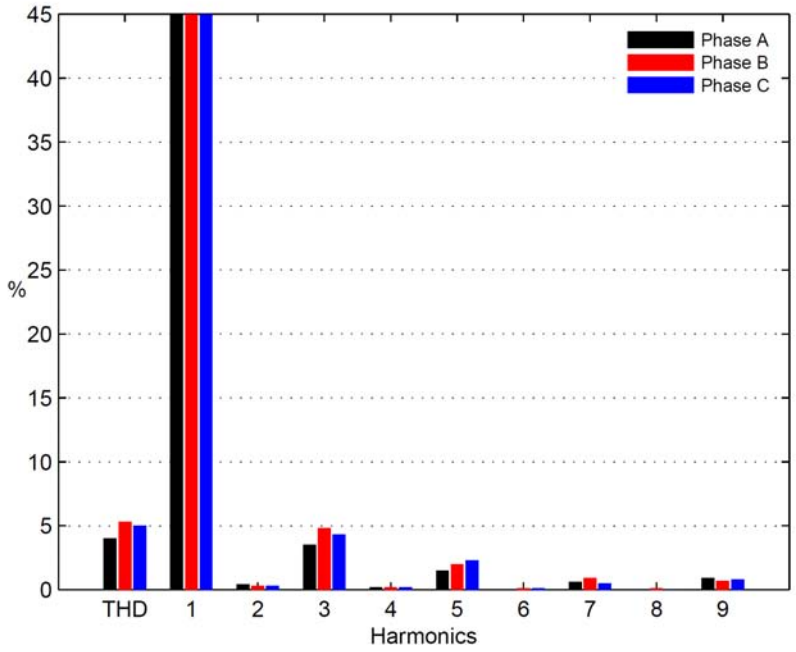

(b)

Fig. 5.4. Case 1 (no dc bias): Transformer is operating under nominal balanced conditions (symmetrical line and load impedances) with no dc bias; (a) Measured and simulated primary winding currents of the load-side transformer; (b) Measured current harmonic spectra (fundamental values are 100% in each phase) showing the presence of harmonics mainly due to nonlinearity from the core and small low order harmonics in supply voltage.

balanced line and loading conditions as before; however, dc bias current of 6 amperes is now injected into the transformer neutrals corresponding to approximately equal dc bias currents (~2A) in each phase. The 6 ampere dc is selected to mimic GICs as it is the maximum current that can be safely generated in the laboratory without seriously damaging equipment. In practice, GICs from several amperes to over hundreds of amperes have been reported. Hence, for this small-scale setup, the lower end currents are deemed sufficient enough to mimic practical conditions seen in a true power system. The peak value of the biased line currents reaches 1.5 pu of rated peak transformer current. This results in approximately balanced dc mmfs in the three core legs.

The impact on transformer primary current waveforms and harmonics is shown in Fig. 5.5. The harmonic distortions have increased slightly ($THD_{i,max}$ = 5.7% and $THD_{v,max}$ = 2.9%). Low order even harmonics were also observed indicating small components of dc leg fluxes causing unipolar saturation. Therefore, it is concluded here that while current harmonics still exist, the application of balanced dc biases does not significantly contribute to an increase in distortions. This is in complete agreement with theory predicting less sensitivity to dc bias for a balanced system. Furthermore, it is observed that power factors remain close to unity despite the presence of dc bias (Table 5.1), which is consistent with the observations reported by [96].

5.3.2 Case 2: Impact of unbalanced transmission system

In general, transmission networks strive to operate in a state of near balance. However, sources of imbalances typically impractical to control may arise. For example, the presence of unbalanced load currents with dc components (e.g., unbalanced rectifiers and power electronic devices in separate phases) and imperfect line transpositions can impact transformers under dc bias. The three-leg core structure itself is also a source of imbalance with different centre and outer leg (phase) nonlinear reluctances. As shown theoretically, such small imbalances can cause the three-phase three-leg transformer to be highly sensitive to dc bias.

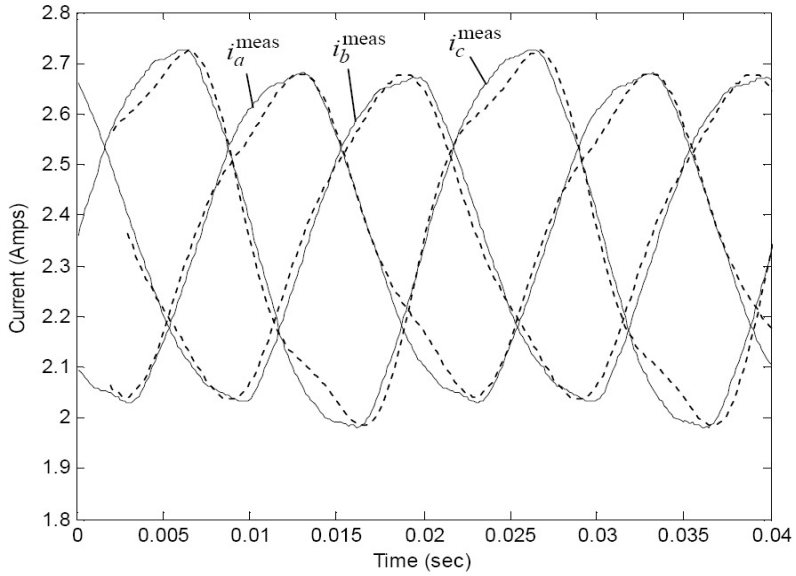

(a)

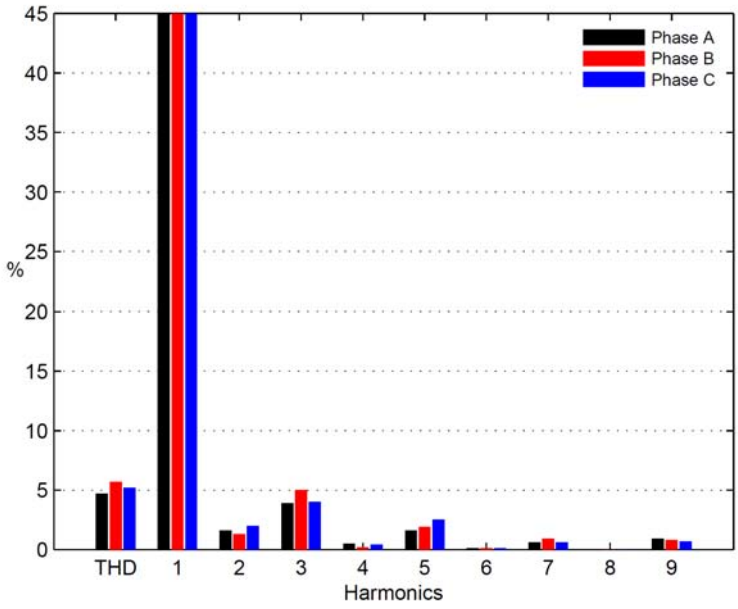

(b)

Fig. 5.5. Case 1 (dc bias): Transformer is operating under balanced conditions (symmetrical line and load impedances) with a dc bias of 6 amperes corresponding to $I_a = I_b = I_c = 1.5$ pu of rated peak transformer current; (a) Measured and simulated primary winding currents of the load-side transformer; (b) Measured current harmonic spectra (fundamental values are 100% in each phase) showing a small 1-2% increase in even harmonics (in comparison to no dc bias of Fig. 5.4) indicating the presence of small dc biased core leg fluxes causing minimal unipolar core saturation.

Table 5.1
Measurements of harmonics and power factors at
the primary of the load-side transformer.

Cases	DC Bias [A]	$THDi_{,a}$ [%]	$THDi_{,b}$ [%]	$THDi_{,c}$ [%]	$THDv_{,a}$ [%]	$THDv_{,b}$ [%]	$THDv_{,c}$ [%]	$PF_{,a}$	$PF_{,b}$	$PF_{,c}$
Case 1: Balanced	0	4.0	5.3	5.0	2.2	2.8	2.8	0.99	0.98	0.98
Line and Load	6	4.7	5.7	5.2	2.3	2.9	2.8	0.99	0.99	0.99
Case 2a:	0	2.9	3.6	3.7	2.2	2.7	2.6	0.99	0.99	0.98
Unbalanced Line #1	6	31.9	7.0	10.8	4.7	3.0	2.6	0.69	0.97	0.83
Case 2b:	0	4.6	5.5	6.8	2.6	3.0	2.9	0.99	0.98	0.97
Unbalanced Line #2	6	42.7	10.5	15.5	4.8	2.6	2.4	0.58	0.94	0.68
Case 3a:	0	5.1	5.1	3.6	2.1	2.8	2.6	0.97	0.98	1.00
Unbalanced Load	6	6.6	5.3	3.5	2.1	2.8	2.6	0.97	0.99	1.00
Case 3b:	0	6.4	3.9	5.4	2.2	2.6	2.6	0.89	1.00	0.99
Unbalanced Load	6	8.9	3.9	5.5	2.1	2.7	2.7	0.92	1.00	0.98

Case 1: $Z_{line,\,a} = Z_{line,\,b} = Z_{line,\,c} = 1.0\ \Omega$, $Z_{load,\,a} = Z_{load,\,b} = Z_{load,\,c} = 15.0\ \Omega$.
Case 2a: $Z_{line,\,a} = 10.0\ \Omega$, $Z_{line,\,b} = 1.1\ \Omega$, $Z_{line,\,c} = 1.4\ \Omega$.
Case 2b: $Z_{line,\,a} = 1.1\ \Omega$, $Z_{line,\,b} = 5.5\ \Omega$, $Z_{line,\,c} = 6.2\ \Omega$.
Case 3a: $Z_{load,\,a} = 24.5\ \Omega$, $Z_{load,\,b} = 10.1\ \Omega$, $Z_{load,\,c} = 5.0\ \Omega$.
Case 3b: $Z_{load,\,a} = 26.0\ \Omega$, $Z_{load,\,b} = 10.0\ \Omega$, $Z_{load,\,c} = 23.0\ \Omega$.

The impact of unbalanced dc bias currents imposed on the transformer was explored by unbalancing the transmission line impedances using rheostats. By doing so, the excitation voltages, dc bias levels and developed mmfs at the load-side transformer become unbalanced. The impact on transformer primary current waveforms is shown for two different transmission line imbalances (Figs. 5.6 and 5.7, Table 5.1). The dc bias currents flow asymmetrically in magnitude through the windings resulting in unbalanced leg dc mmfs. The corresponding dc fluxes and primary currents behave as predicted by magnetic circuit theory and are closely matched in simulations. In contrast with the balanced scenario (Case 1), the power quality of the input voltages and currents has deteriorated substantially (over 30% increase in THD_i) mostly due to the generation of second-order current harmonics. Furthermore, the transformer is severely overloaded reaching 2 pu of rated peak current and reactive power flow has increased significantly as indicated by the low power factors.

The impact of winding configurations was tested by repeating Case 2b with

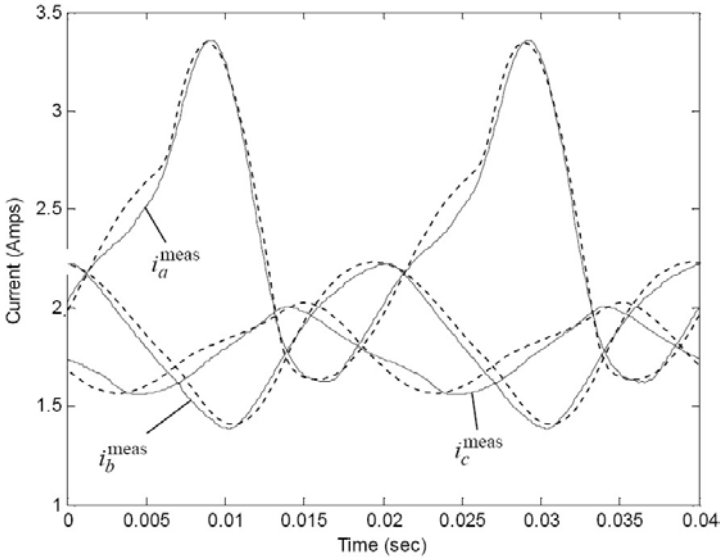

(a)

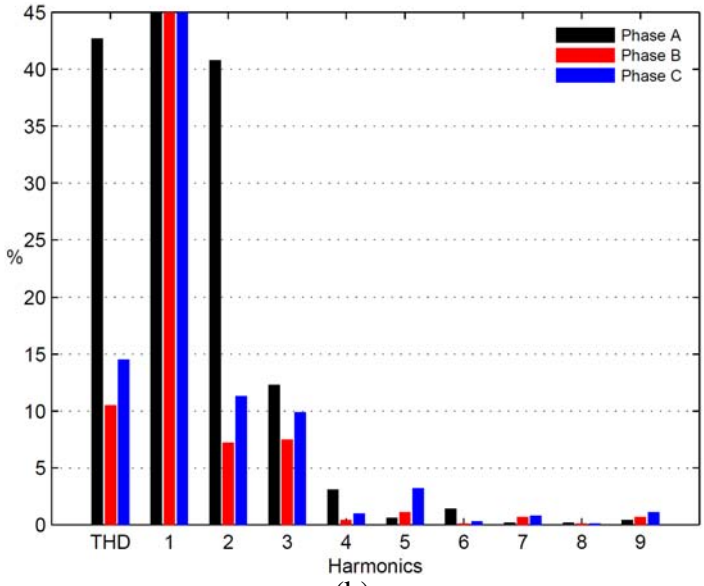

(b)

Fig. 5.6. Case 2a (dc bias): Transformer is operating under unbalanced conditions with a dc bias source current of 6 amperes (I_a= 1.5, I_b= 1.7 I_c= 1.4 pu of rated peak transformer current). System imbalance is achieved by mismatching the transmission line phase impedances ($Z_{line,a}$ = 10.0 Ω, $Z_{line,b}$ = 1.1 Ω, $Z_{line,c}$ = 1.4 Ω) which affect the load-side transformers leg mmfs; (a) Measured and simulated primary current waveforms; (b) Measured current harmonic spectra (fundamental values are 100% in each phase) indicating a large increase in harmonic distortion (over 30% THD_i) mostly due to even harmonics generated by large dc biased fluxes and unipolar half-wave saturation of the transformer core.

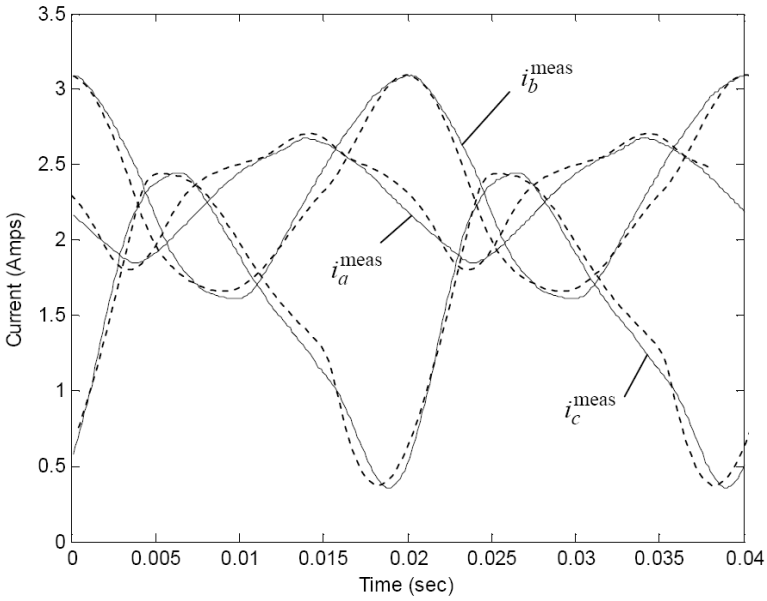

(a)

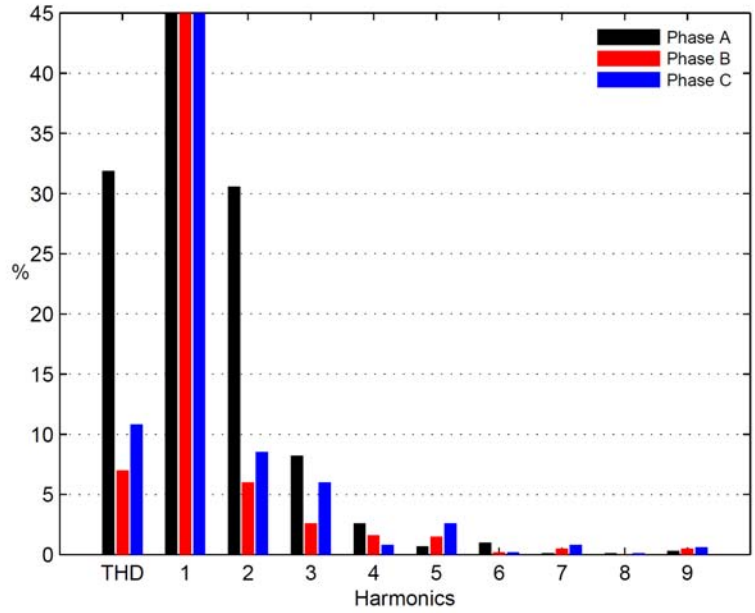

(b)

Fig. 5.7. Case 2b (dc bias): Transformer is operating under a different set of unbalanced conditions ($Z_{line,a}$ = 1.1 Ω, $Z_{line,b}$ = 5.5 Ω, $Z_{line,c}$ = 6.2 Ω) with a dc bias source current of 6 amperes (I_a= 1.9, I_b= 1.3 I_c= 1.1 pu of rated peak transformer current); (a) Measured and simulated primary current waveforms of the load-side transformer; (b) Measured current harmonic spectra (fundamental values are 100% in each phase) which also show a large increase in current harmonics (up to 42.8% THD_i).

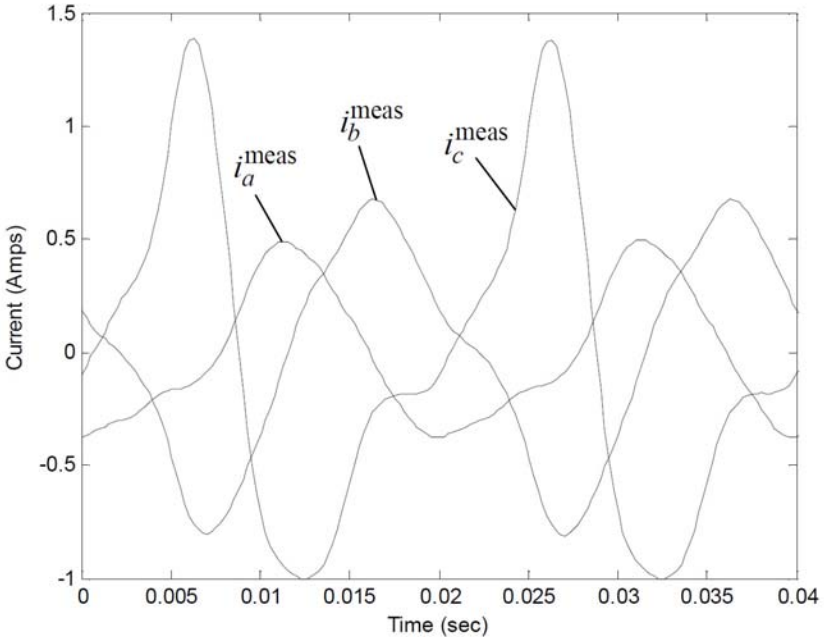

(a)

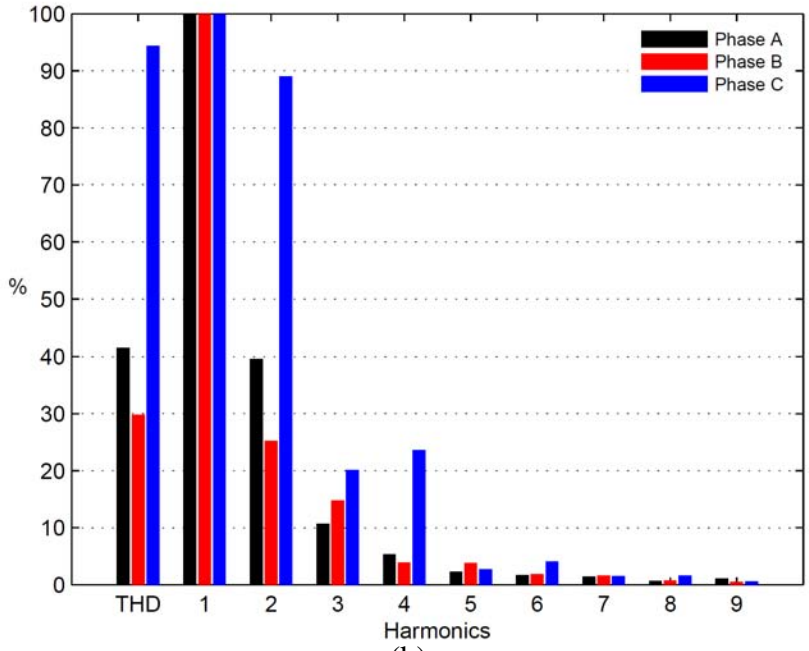

(b)

Fig. 5.8. Case 2c (dc bias): Transformer is operating under the same unbalanced conditions as Case 2b (Fig. 5.7) except the transformer connections have been modified to delta/wye-grounded (source-side transformer) and wye-grounded/delta (load-side transformer) with a dc bias source current of 6 amperes; (a) Measured primary current waveforms of the load-side transformer; (b) Measured current harmonic spectra indicating severe current harmonic generation ($THD_{i,max}$ = 94.4%).

delta/wye-grounded and wye-grounded/delta connections for the source-side and load-side transformers, respectively (Fig. 5.8). It is well known that delta/wye transformers, used for stepping up generator voltages, can block dc bias currents from entering the generation equipment by virtue of having no zero-sequence path to ground [102]. Nevertheless, as demonstrated in Fig. 5.8, unbalanced dc bias currents may still result in a significant increase of current harmonic distortions (over 90% THD_i) due to unipolar core flux saturation compared to the balanced dc bias case. This can potentially cause severe damage to generator equipment.

5.3.3 Case 3: Impact of unbalanced transformer loading

The influence of unbalanced loads on transformer operation under dc bias was examined. Many combinations of load imbalance were tested by changing the phase impedances of the wye-connected load with rheostats. The results for two different unbalanced load conditions are shown in Table 5.1. Measurements and simulations indicate very small changes in distortion (up to 2% change in THD_i) with and without the 6 ampere dc bias. Thus, based on these results, unbalanced loads appear to have less of an impact on power quality in the presence of dc bias compared to unbalanced transmission line operation.

5.4 CONCLUSION

This study presents a new analysis based on electromagnetic circuit theory, simulation and experimental results to explore the impacts of (un)balanced dc bias on the operation of three-phase three-leg transformers. In particular, the significance of power system symmetry in suppressing harmonic distortion in a dc biased three-leg transformer is studied. A detailed asymmetric three-phase three-leg transformer model suitable for dc bias investigations has been implemented. Theoretical predictions are confirmed by simulation results which are further corroborated with experimental tests. The main conclusions are:

- The link between unbalanced transformer operation and the generation (and suppression) of dc fluxes in three-leg cores is analytically shown for the first time

using electromagnetic circuit theory. The possibility of unbalanced dc leg mmfs leading to dangerously biased dc core leg fluxes is demonstrated.

- Large zero-sequence reluctances (e.g., due to tank structure and air gaps) can amplify the impact of unbalanced dc bias currents and further increase harmonic distortions. However, these effects can largely be mitigated if precisely balanced conditions exist as shown in theory and by experimentation.
- Furthermore, experimental and simulation results confirm that regardless of dc bias current magnitude, the impact on harmonics and reactive power flow generated in three-leg transformer cores is insignificant provided the dc mmfs in the core legs are balanced (Figs. 5.4 and 5.5 and Table 5.1, rows 3, 4).
- On the other hand, unbalanced leg dc leg mmfs invariably lead to excessive peak currents, even and odd current harmonics and increased reactive power flow (Figs. 5.6 to 5.8 and Table 5.1, rows 6, 8, 10, 12) due to large dc biased fluxes circulating in the core resulting in unipolar and asymmetric saturation.
- Moreover, under dc bias it was observed that unbalanced transmission line impedances more significantly upset the balance in the net leg dc mmfs compared to unbalanced loads (Table 5.1, rows 6, 8, 10, 12), thereby causing large dc leg fluxes to appear.
- The presented time-domain modelling approach is based on a true and accurate representation of an asymmetric three-phase transformer. It is well suited for protection studies where accurate prediction of transformer behaviour and stress under dc bias is beneficial for over-current and differential relay coordination studies.
- This study shows its importance in establishing design and operational guidelines for power system operators to consider system imbalances and its impact during dc bias events (e.g., GICs). Furthermore, the analysis highlights the importance and potential benefits of seeking out alternative transformer core designs with reduced core asymmetry which could assist in suppressing dc bias effects.

Chapter 6. Aging of three-phase transformers in distorted power systems

6.1 INTRODUCTION

Transformer performance under degraded power quality of transmission and distribution systems has come under further scrutiny which could adversely impact the transformer service life [37, 103-105]. The vast majority of transformer aging publications study the loss of life effect from insulation and dielectric breakdown relating to temperature rise above rated operation [106-110]. However, there are very limited studies which attempt to relate the effect of voltage and current harmonic distortions to temperature rise and aging. Through a series of studies [111-116] it has been shown that even and odd harmonic distortions present in the power system voltage resulted in increased ohmic and iron-core losses in transformers leading to a temperature rise. In most situations, it is the low order odd harmonics that are more common and problematic in power systems having the greatest impact on electric machine aging [37]. The possibility, however, exists for even order harmonics to contribute to aging with unsymmetrical waveform distortions (e.g., dc bias from half-wave diode rectifier loads, half-cycle transformer saturation due to geomagnetically induced currents or proximity to HVDC return currents [32]).

Reference [111] introduced a relatively simple approach for estimating transformer aging based on the weighted harmonic factor (WHF) defined as the ratio of total harmonic losses to the fundamental losses [37]. However, WHF is computed using a simplified transformer harmonic model and superposition theorem. In addition, past transformer aging studies have mainly been restricted to sinusoidal, single-phase or balanced symmetric operation of transformers. This is seldom true as transformers often operate in a state of power system imbalance and distortion. Furthermore,

three-phase transformer core structures exhibit inherent asymmetry in their designs (e.g., three-leg and five-leg cores) which have not been considered in prior aging studies.

The main contribution of this study is an improved method of estimating transformer aging based on the recently developed and validated nonlinear model of a three-phase asymmetric three-leg transformer (Chapter 2) [26, 32, 39, 117]. Unlike existing approaches, the proposed method is applicable to three-phase asymmetric multi-leg transformer cores operating with (un)balanced and (non)linear loads and considers the harmonic interactions between the load, transformer and grid source nonlinearities. The model improves upon the conventional WHF approach [37, 111-113] of aging estimation by direct evaluation of additional fundamental and harmonic losses generated by the iron-core, nonlinear loads and terminal voltage distortions. The nonlinear model is implemented in time-domain and considers core topology, magnetic couplings of the legs, as well as nonlinearities and asymmetries in the iron core structure. Furthermore, accurate dynamic hysteresis nonlinearities including major and minor loop effects are incorporated in each magnetically coupled core-leg. Based on this new approach, aging estimations are carried out for different operating conditions and the results are compared against the conventional WHF approach.

6.2 TRANSFORMER AGING BASED ON WEIGHTED HARMONIC FACTOR AND ARRHENIUS THERMAL REACTION THEORY

The lifetime of magnetic devices such as transformers is largely related to their operating temperature which has been known to rise in the presence of terminal voltage harmonics. Transformer parts (e.g., insulation and core material) and their cooling systems are normally manufactured to accommodate a maximum allowed temperature rise ($T_{rise,\ rated}$) for continuous rated sinusoidal operating conditions [2]. The resulting transformer operating temperature considering worst-case ambient temperature (e.g., $T_{amb} = 40^{o}\ C$) can be expressed as

$$T_{rated} = T_{amb} + T_{rise,rated} \tag{6.1}$$

The voltage harmonics and their phase shifts can lead to additional fundamental and harmonic losses within the transformer leading to increases in operating temperatures beyond $T_{rise,\ rated}$ (6.1) and thermal stresses on the insulation [37]. If the rated temperature is exceeded over any period of time, the service life can be significantly reduced due to breakdown in insulation dielectrics and thermal fatiguing of components. A method of estimating temperature rise and resulting aging due to system voltage harmonics has been previously developed through the use of weighted harmonic factors and Arrhenius thermal reaction theory [37, 111-113].

6.2.1 Weighted harmonic factor (WHF)

Prior studies have found that the harmonic spectra of voltages supplying magnetic devices have a noticeable impact on the operating temperature that can be quantified by the weighted harmonic factor (WHF). WHF for transformers is derived from their electric equivalent circuits which accounts for the effect of additional transformer losses (fundamental and harmonics) due to voltage harmonics. The complete derivation of WHF is omitted for the sake of brevity and can be found in [37, 111]. WHF is defined as the ratio of the sum of transformer losses for all harmonic orders to total transformer losses at the fundamental frequency. According to [37, 111], it was found that the WHF could be approximated as

$$WHF_{estimated} = \frac{W_{\text{total},h\sum}}{W_{\text{total},1}} = K_1 \sum_{h=2}^{\infty} \frac{1}{(h)^k} \left(\frac{V_{ph}}{V_{p1}} \right)^l \tag{6.2}$$

where, $W_{total,h\sum}$ and $W_{total,1}$ are the total harmonic and fundamental losses, respectively, h is the harmonic order, V_{ph} and V_{p1} are the h^{th} harmonic and fundamental rms phase terminal voltages, respectively, and K_1 is a proportionality constant. In the original study, parameters *k* and *l* were found to fall within a certain range depending on the type of magnetic device [37].

Based on experimental data [112, 113], Table 6.1 shows the range of exponents k

and l assume for single-phase and three-phase transformers as well as rotating electrical machines. These parameters represent the various sensitivities in temperature-rises that occur for different electrical machines in the presence of terminal voltage harmonics. In this study, the values used for the conventional aging estimations are $0.6 \le k \le 1.2$ and $1.5 \le l \le 2$ which correspond to transformer type devices. Therefore, minimum (best-case) and maximum (worst-case) aging is computed with this method.

As can be inferred from the right hand side of (6.2), WHFs are approximated from the terminal voltage harmonic spectra and each harmonic order has a different weighting in its effect on additional losses and aging. Low order harmonic components have the highest impact. Based on empirical data, it is then possible to deduce the temperature rise in Celsius from the WHF for a given magnetic device. An inaccuracy associated with (6.2) is the application of superposition.

Table 6.1

Evaluation of weighted harmonic factor exponents

k and l based on measured temperature rises [112, 113].

Apparatus	**k**	$\mathbf{k_{average}}$	**l**	$\mathbf{l_{average}}$
Single-phase transformer	$0.6 \le k \le 1.2$	0.90	$1.5 \le l \le 2.0$	1.75
Three-phase transformer	$0.6 \le k \le 1.2$	0.90	$1.5 \le l \le 2.0$	1.75
Single-phase induction machine	$0.7 \le k \le 1.2$	0.85	$1.0 \le l \le 1.8$	1.40
Three-phase induction machine	$0.7 \le k \le 1.2$	0.95	$1.2 \le l \le 2.0$	1.60
Universal machine	$0.8 \le k \le 1.2$	1.00	$1.5 \le l \le 2.5$	2.00

6.2.2 WHF and temperature rise in transformers

For small additional temperature rises compared with the rated temperature rise, the cooling conditions are not significantly altered and therefore it can be assumed that the additional losses (quantified by the WHF) are proportional to additional temperature rise. Based on measurement data given in [37], the graph of Fig. 6.1 is used to translate WHF into temperature rise. Knowing the temperature rise, the final

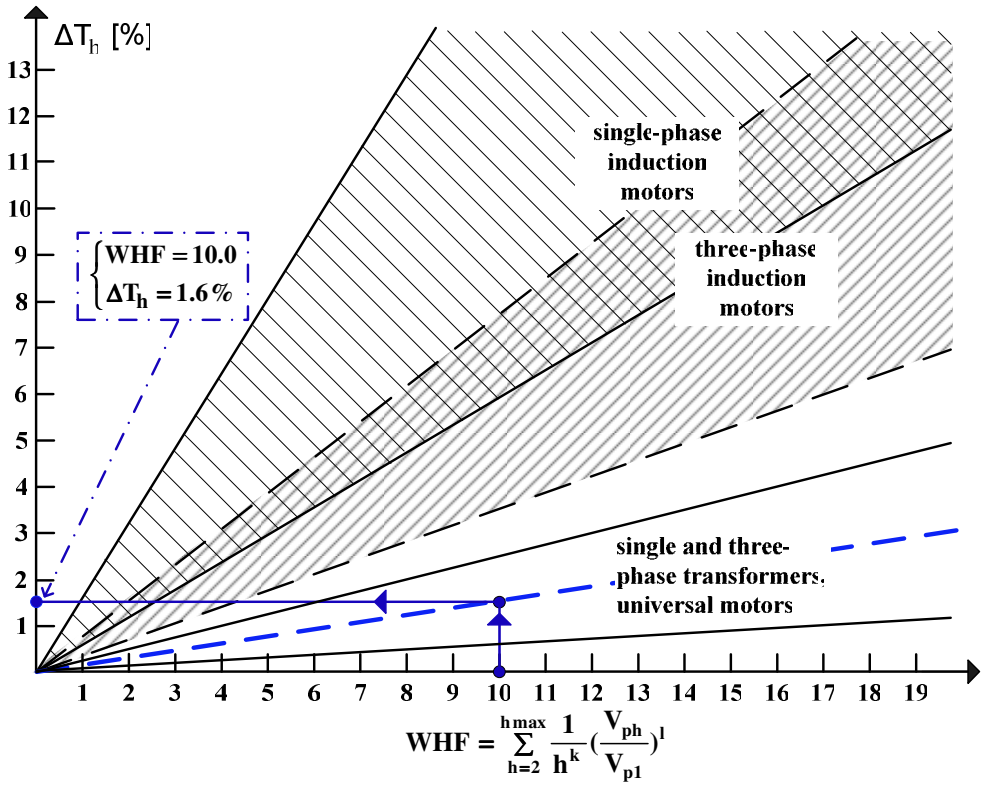

Fig. 6.1. Additional temperature rise versus WHF [37]. The blue-dotted line is selected for the study as it represents the median characteristics for the three-phase transformer part of the graph.

step relies on Arrhenius' thermal reaction rate theory in order to relate temperature rise to an estimated value of loss in operating service life.

6.2.3 Transformer aging estimation with Arrhenius thermal reaction rate theory

The thermal aging of electromagnetic devices is mostly related to the strength of insulation material which can be of organic or inorganic origin. The additional heating caused by loss dissipation in the machine can cause mechanical weakening or a breakdown in dielectric behaviour in the insulator. In addition to thermal stresses, harmonics can produce mechanical vibrations that can further cause mechanical stresses.

Thermal degradation has long been studied and can be modelled using the rate

reaction law derived by Swedish scientist Svante Arrhenius. The reaction rate can be represented in differential equation form as follows

$$\frac{dR}{dt} = Ae^{-E/KT} \tag{6.3}$$

where dR/dt is the property experiencing thermal aging reduction with respect to time *t*, A is an integration constant, K is the Boltzmann gas constant, T is the absolute temperature in Kelvins and E is the activation energy of the aging reaction. After some manipulation [37], the integration of (6.3) can be expressed as

$$\ln R - \ln t = \ln A - \left(\frac{E}{K}\right)\frac{1}{T} \tag{6.4}$$

which can be written in the form of a log scale linear equation

$$\ln t = \left(\frac{E}{K}\right)\frac{1}{T} + B \tag{6.5}$$

On a logarithmic scale, equation (6.5) produces a straight line which is known as the Arrhenius plot. The slope of the Arrhenius plot determines the aging of the insulation material and can be used to measure the aging in transformers. From two points of this line for temperature (T_1, T_2) and lifetime (t_1, t_2), the following can be written,

$$\ln t_1 - \ln t_2 = \left(\frac{E}{K}\right)\left(\frac{1}{T_1} - \frac{1}{T_2}\right) \tag{6.6}$$

where t_2 is the rated lifetime, t_1 is the reduced life time, T_2 is the rated temperature ($T_2 = T_{rated} = T_{amb} + T_{rise,rated}$) and T_1 is the new temperature. The ambient temperature is typically considered to be at the most $T_{amb} = 40^o\ C$ and a commonly permitted rated temperature rise value of $T_{rise,rated} = 80^o\ C$ is used. Given that the new elevated temperature is $T_1 = T_2 + \Delta T$, substituting this into (6.6) results in

$$\ln t_1 - \ln t_2 = \left(\frac{E}{K}\right)\left(\frac{1}{T_2 + \Delta T} - \frac{1}{T_2}\right) \tag{6.7}$$

After some manipulation of (6.7), and given rated operating temperatures T_2, rated

service life t_2, and ΔT computed from WHF, the new service lifetime of the device is estimated as

$$t_1 = t_2 e^{-\left(\frac{E}{K}\right)\left(\frac{\Delta T}{T_2(T_2+\Delta T)}\right)} \tag{6.8}$$

and loss of transformer life can be expressed as a percentage

$$\left(1-\frac{t_1}{t_2}\right)\times 100\% \tag{6.9}$$

6.2.4 Deficiencies associated with WHF approach

While the WHF method is moderately simple to apply, it does however suffer from several significant drawbacks:

- Different transformer loading levels cannot be included in the calculation since the conventional WHF is based mainly on the composition of the terminal voltage waveform.
- Current harmonics injected by nonlinear loads are not directly considered as well as their interactive effects with power system induced harmonics and transformer nonlinearities.
- WHF is derived from a linear single-phase transformer equivalent circuit for each harmonic frequency. Superposition for the harmonic component effects for WHF are used which is not strictly valid for nonlinear systems. Thus, coupling effects amongst the harmonics are not properly considered.
- WHF method cannot be applied for unbalanced three-phase transformer and power system operation.
- When applied to three-phase transformers, WHF assumes the loss distribution in multi-leg cores to be symmetric. The magnetic circuit with coupling effects and asymmetry in the core-legs are therefore omitted.
- Dynamic hysteresis nonlinearities (major and minor loop formations) impact

core-losses and aging which are not considered in WHF

- WHF only considers the effect of terminal harmonic voltage magnitudes but ignores the phase-shifts of the harmonics
- Errors and difficulty in determining k and l for (6.2) result in a large uncertainty in the projected aging estimation.

In order to address these deficiencies, a new enhanced transformer aging estimation method is proposed based on detailed and accurate nonlinear modelling of three-phase multi-leg transformers.

6.3 PROPOSED ENHANCED AGING ESTIMATION BASED ON ACCURATE NONLINEAR THREE-PHASE TRANSFORMER MODEL

This section describes the proposed aging estimation method and improvement over the conventional WHF approach. An overview of the computational method for transformer additional losses based on the nonlinear three-phase multi-leg transformer core model used for estimating aging is described. The model features accurate representation of seldom considered hysteresis nonlinearities (major and minor loops) with core asymmetry and magnetic cross-coupling effects in the core-leg fluxes. These effects have so far been ignored in conventional transformer aging studies.

An improvement to the WHF computation is made possible through detailed loss analysis enabled by the three-phase nonlinear transformer model. According to the definition, WHF is the ratio of the total harmonic losses to the fundamental losses in the transformer. As an alternative to using the right-hand-side of (6.2) which only considers terminal voltage characteristics, the model can be used to directly evaluate fundamental and harmonic losses for the WHF as follows:

$$WHF_{actual} = \frac{W_{\text{total},h\sum}}{W_{\text{total},1}}$$ where

$$
\begin{aligned}
W_{\text{total},h\sum} &= \sum_{h=2}^{h_{\max}} \left(P^{h}_{\text{windings}} + P^{h}_{\text{hys+eddy}} \right) \\
&= \sum_{h=2}^{h_{\max}} \Big[\left(I^{h}_{p,a} \right)^2 R_{p,a} + \left(I^{h}_{p,b} \right)^2 R_{p,b} + \left(I^{h}_{p,c} \right)^2 R_{p,c} \\
&+ \left(I^{h}_{s,a} \right)^2 R_{s,a} + \left(I^{h}_{s,b} \right)^2 R_{s,b} + \left(I^{h}_{s,c} \right)^2 R_{s,c} \\
&+ \left(I^{h}_{\text{hys+eddy},a} \right)^2 R_{c,a} + \left(I^{h}_{\text{hys+eddy},b} \right)^2 R_{c,b} + \left(I^{h}_{\text{hys+eddy},c} \right)^2 R_{c,c} \Big]
\end{aligned}
\tag{6.10}
$$

and

$$
\begin{aligned}
W_{\text{total, 1}} &= P^{1}_{\text{windings}} + P^{1}_{\text{hys+eddy}} \\
&= \left(I^{1}_{p,a} \right)^2 R_{p,a} + \left(I^{1}_{p,b} \right)^2 R_{p,b} + \left(I^{1}_{p,c} \right)^2 R_{p,c} \\
&+ \left(I^{1}_{s,a} \right)^2 R_{s,a} + \left(I^{1}_{s,b} \right)^2 R_{s,b} + \left(I^{1}_{s,c} \right)^2 R_{s,c} \\
&+ \left(I^{1}_{\text{hys+eddy},a} \right)^2 R_{c,a} + \left(I^{1}_{\text{hys+eddy},b} \right)^2 R_{c,b} + \left(I^{1}_{\text{hys+eddy},c} \right)^2 R_{c,c}
\end{aligned}
\tag{6.11}
$$

where primary and secondary phase currents $I^{h}_{p,k}$ and $I^{h}_{s,k}$ as well as hysteresis and eddy loss currents $I^{h}_{\text{hys+eddy},k}$ are computed from the nonlinear model at each harmonic h for each phase $k=(a, b, c)$.

The formulation of losses from the electromagnetic circuit includes the effect of core nonlinearities, hysteresis and eddy current losses, as well as load current (fundamental and harmonic) ohmic losses in the windings. The asymmetric loss distribution exhibited in multi-leg core structures is also considered with different hysteresis functions (2.4)-(2.5) defined for each core-leg. Furthermore, the electromagnetic solution fully considers the harmonic couplings and interactions with system harmonics, load and transformer nonlinearities currently ignored in the conventional WHF calculation (6.2). Through direct evaluation of WHF in (6.10)-(6.11), subjective machine dependent parameters k and l of (6.2) no longer need to be determined since the model mimics the electric machine characteristics. Thus, it is then possible to carry out the rest of the aging calculation based on Arrhenius' thermal reaction rate theory as described in Section 6.2. Fig. 6.2 depicts the augmented nonlinear transformer model for the purpose of aging estimation with terminal voltage distortions and (un)balanced nonlinear loads.

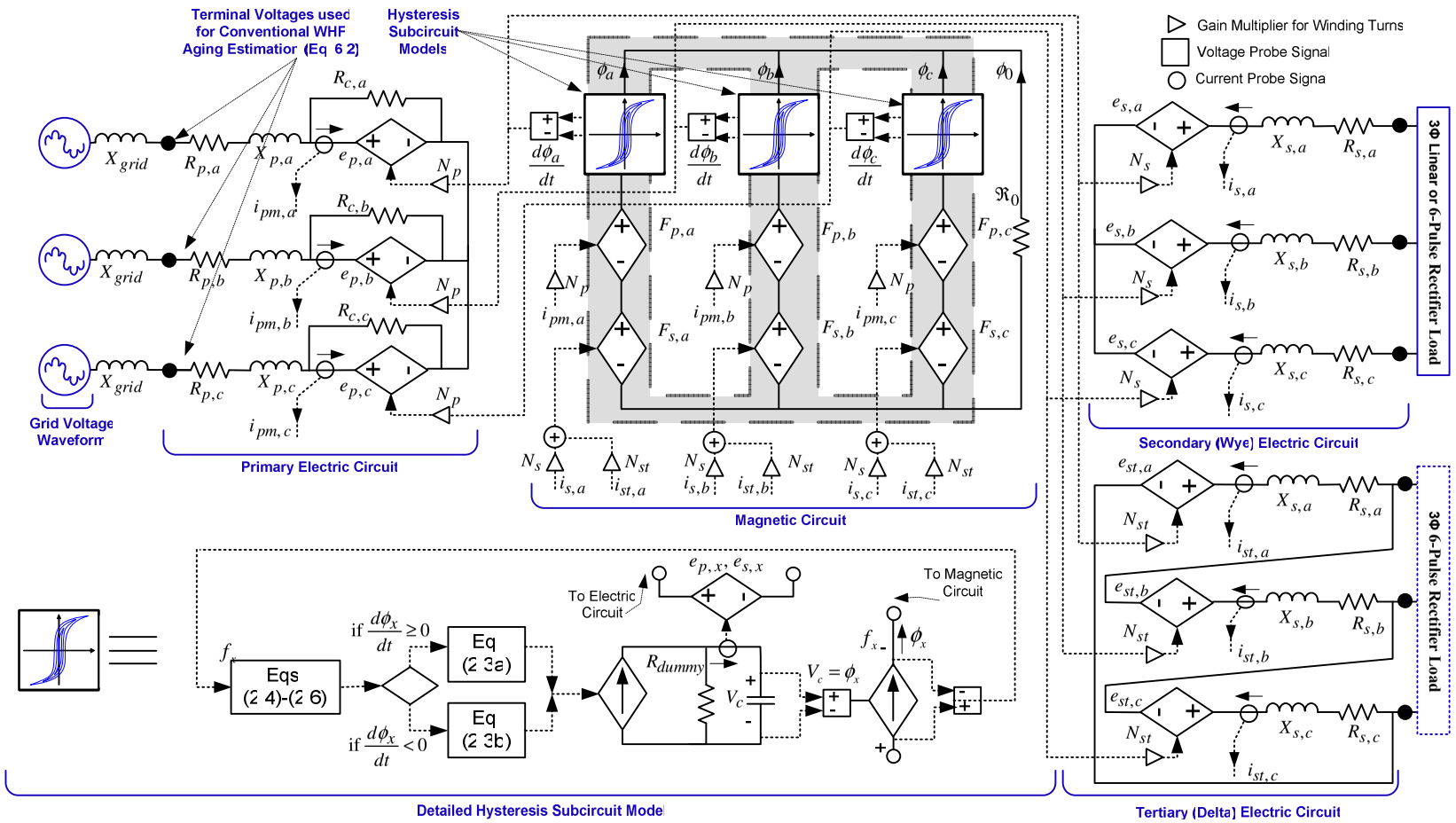

Fig. 6.2. Nonlinear model of a three-phase three-leg transformer (wye/wye) for estimating transformer aging considering (un)balanced nonlinear loading, magnetic hysteresis and asymmetric core-leg coupling effects.

6.4 RESULTS AND DISCUSSION

Extensive simulation tests are performed for four types of three-phase transformer; T1: 1.65 kVA ($440\sqrt{3}/55\sqrt{3}$ V), T2: 7.5 kVA (380/220 V), T3: 60 kVA (380/220 V) and T4: 2 MVA (25000/575 V) with three-leg cores (Appendix A) operating under (un)balanced (non)linear conditions. WHF and transformer aging are compared for the proposed aging calculation method and the conventional estimation approach under various operating conditions as shown in Table 6.2. The selected case studies depict practical scenarios of transformer operation under degraded power quality conditions. Therefore, case studies have been performed at different load levels, harmonic distortions and unbalanced conditions in order to test the validity of the different aging estimation methods. Time-domain waveforms of transformer currents and voltages are shown for selected cases in Figs. 6.3 to 6.4 and 6.6 to 6.7.

Table 6.2

Effect of degraded power quality on three-phase distribution transformer aging.

$\phi_{h=5}$ [deg]	Load [%]*	THD** [%]		Conventional Aging Estimation [3, 9]				Proposed Aging Calculation							
				$WHF_{estimated}$ for T4 (Eq. 2)		Decrease in Life for T4 (Eq. 9) [%]		WHF_{actual}*** (Eqs. 14-15)				Decrease in Life*** (Eq. 9) [%]			
		i_p	v_p	min	max	min	max	T1	T2	T3	T4	T1	T2	T3	T4
Case A: Rated Sinusoidal & Linear Load															
	0-100	0.226	~0	0	0	0	0	0	0	0	0	0	0	0	0
Case B1: Nonsinusoidal 10% of 5th Harmonic Terminal Voltage ($V_{h=5}=0.1\angle\phi_{h=5}$ pu) & Linear Load															
0	125	9.797	9.970	4.563	11.986	4.010	10.166	0.981	0.964	0.954	0.967	1.027	1.009	0.999	0.865
	100	9.845	9.979	4.570	12.002	4.016	10.179	0.982	0.976	0.972	0.978	1.028	1.021	1.017	0.875
	75	9.871	9.986	4.574	12.015	4.020	10.189	0.983	0.987	0.985	0.987	1.029	1.033	1.031	0.883
	50	9.868	9.990	4.577	12.022	4.022	10.195	0.984	0.998	0.996	0.993	1.030	1.044	1.042	0.888
	25	9.775	9.993	4.579	12.027	4.024	10.199	0.984	1.013	1.000	0.998	1.030	1.060	1.047	0.893
180	125	9.797	9.970	4.563	11.986	4.010	10.166	0.981	0.961	0.947	0.963	1.027	1.006	0.991	0.861
	100	9.845	9.979	4.570	12.002	4.016	10.179	0.983	0.974	0.964	0.974	1.029	1.020	1.009	0.871
	75	9.871	9.986	4.574	12.015	4.020	10.189	0.984	0.987	0.976	0.983	1.030	1.033	1.021	0.879
	50	9.868	9.990	4.577	12.022	4.022	10.195	0.985	1.000	0.986	0.989	1.031	1.046	1.032	0.884
	25	9.775	9.993	4.579	12.027	4.024	10.199	0.985	1.019	0.991	0.994	1.031	1.066	1.037	0.889
Case B2: Nonsinusoidal 20% of 5th Harmonic Terminal Voltage ($V_{h=5}=0.2\angle\phi_{h=5}$ pu) & Linear Load															
0	125	19.648	19.944	12.907	33.901	10.900	25.975	3.937	3.847	3.805	3.866	4.052	3.961	3.919	3.409
	100	19.757	19.961	12.927	33.952	10.915	26.008	3.932	3.892	3.873	3.911	4.047	4.007	3.987	3.448
	75	20.419	19.974	12.936	33.978	10.923	26.025	3.951	3.930	3.922	3.952	4.066	4.045	4.036	3.484
	50	21.022	19.986	12.956	34.029	10.938	26.058	3.944	3.959	3.963	3.981	4.059	4.074	4.078	3.508
	25	20.239	19.952	12.918	33.930	10.908	25.994	3.954	3.984	3.982	3.974	4.069	4.099	4.097	3.503
180	125	19.607	19.895	12.869	34.214	10.869	26.178	3.924	3.833	3.789	3.838	4.039	3.947	3.902	3.384
	100	19.724	19.912	12.878	33.826	10.877	25.927	3.929	3.880	3.855	3.882	4.044	3.994	3.969	3.423
	75	19.817	19.926	12.898	33.877	10.892	25.960	3.935	3.917	3.904	3.917	4.049	4.032	4.019	3.453
	50	19.887	19.935	12.907	33.903	10.900	25.976	3.937	3.947	3.944	3.941	4.052	4.062	4.058	3.474
	25	19.924	19.941	12.907	33.903	10.900	25.976	3.939	3.981	3.962	3.960	4.053	4.097	4.077	3.490
Case C1: Sinusoidal Terminal Voltage & 6-Pulse Rectifier Load															
-	125	25.024	0.508	0.049	0.167	0.044	0.150	5.582	5.816	2.297	5.646	5.691	5.922	2.386	4.936
	100	25.575	0.439	0.037	0.131	0.034	0.118	5.093	5.712	1.781	5.572	5.208	5.820	1.856	4.873
	75	26.176	0.371	0.028	0.100	0.025	0.089	4.303	5.349	1.211	5.217	4.419	5.461	1.266	4.571
	50	26.746	0.286	0.018	0.067	0.016	0.060	2.915	4.362	0.642	4.205	3.017	4.478	0.674	3.702
	25	27.139	0.176	0.007	0.031	0.007	0.028	1.092	2.108	0.193	2.002	1.142	2.192	0.203	1.781
Case C2: Sinusoidal Terminal Voltage & 12-Pulse Rectifier Load															
-	125	10.492	0.436	0.023	0.095	0.021	0.085	2.112	2.255	0.778	4.208	2.196	2.343	0.816	3.704
	100	10.914	0.409	0.016	0.095	0.014	0.085	1.889	2.239	0.607	3.948	1.967	2.326	0.636	3.480
	75	11.437	0.336	0.018	0.064	0.016	0.057	1.486	2.045	0.404	3.305	1.551	2.127	0.424	2.922
	50	12.013	0.274	0.010	0.050	0.009	0.045	0.936	1.589	0.214	2.287	0.980	1.657	0.225	2.032
	25	12.649	0.160	0.004	0.021	0.004	0.019	0.312	0.747	0.069	0.816	0.328	0.782	0.073	0.731

Table 6.2 (Continued)

$\phi_{h=5}$ [deg]	Load [%] *	THD** [%]		Conventional Aging Estimation [3, 9]				Proposed Aging Calculation							
				$WHF_{estimated}$ for T4 (Eq. 2)		Decrease in Life for T4 (Eq. 9) [%]		WHF_{actual}*** (Eqs. 14-15)				Decrease in Life*** (Eq. 9) [%]			
		i_p	v_p	min	max	min	max	T1	T2	T3	T4	T1	T2	T3	T4
Case D1: Nonsinusoidal 10% of 5th Harmonic Terminal Voltage ($V_{h=5} = 0.1\angle\phi_{h=5}$ pu) & 6-Pulse Rectifier Load															
0	125	28.337	9.833	4.488	11.832	3.945	10.043	6.940	7.458	3.407	7.291	7.022	7.524	3.517	6.324
	100	28.655	9.880	4.516	11.900	3.970	10.098	6.384	7.283	2.834	7.093	6.480	7.354	2.935	6.158
	75	29.001	9.923	4.542	11.959	3.992	10.145	5.471	6.791	2.218	6.602	5.582	6.877	2.305	5.745
	50	29.243	9.959	4.563	12.009	4.010	10.185	4.010	5.642	1.639	5.425	4.125	5.751	1.709	4.748
	25	29.300	9.987	4.579	12.040	4.024	10.210	2.112	3.208	1.177	3.066	2.196	3.315	1.230	2.714
180	125	21.768	10.228	4.756	12.521	4.176	10.594	4.720	4.785	2.844	4.495	4.836	4.900	2.946	3.952
	100	22.599	10.187	4.725	12.436	4.150	10.525	4.563	4.818	2.466	4.631	4.680	4.933	2.560	4.068
	75	23.491	10.133	4.688	12.335	4.117	10.445	4.115	4.682	2.033	4.579	4.231	4.798	2.115	4.024
	50	24.499	10.075	4.642	12.210	4.078	10.345	3.203	4.092	1.574	4.061	3.310	4.207	1.642	3.577
	25	25.476	10.026	4.609	12.115	4.050	10.270	1.854	2.568	1.188	2.562	1.931	2.664	1.242	2.274
Case D2: Nonsinusoidal 20% of 5th Harmonic Terminal Voltage ($V_{h=5} = 0.2\angle\phi_{h=5}$ pu) & 6-Pulse Rectifier Load															
0	125	31.806	19.843	12.833	33.755	10.841	25.881	8.983	9.658	5.974	9.453	8.985	9.624	6.077	8.115
	100	32.562	19.879	12.867	33.835	10.868	25.933	8.577	9.462	5.439	9.264	8.599	9.439	5.550	7.960
	75	32.163	19.921	12.901	33.917	10.895	25.985	7.747	8.982	4.933	8.789	7.803	8.984	5.048	7.569
	50	32.264	19.963	12.937	34.004	10.923	26.042	6.483	7.971	4.454	7.781	6.577	8.018	4.570	6.734
	25	32.199	19.977	12.951	34.029	10.934	26.058	4.892	5.895	4.079	5.732	5.007	6.000	4.195	5.009
180	125	17.295	20.183	13.158	34.591	11.099	26.421	3.068	4.433	5.217	3.386	3.173	4.550	5.331	2.992
	100	18.029	20.164	13.135	34.524	11.080	26.378	3.377	4.591	5.055	3.707	3.487	4.707	5.169	3.271
	75	18.963	20.125	13.093	34.409	11.047	26.304	3.732	4.758	4.824	4.085	3.845	4.874	4.940	3.598
	50	20.149	20.081	13.050	34.289	11.013	26.226	4.023	4.793	4.540	4.450	4.138	4.909	4.656	3.913
	25	21.522	20.037	13.008	34.172	10.980	26.151	4.114	4.487	4.219	4.512	4.229	4.603	4.335	3.966
Case D3: Nonsinusoidal 10% of 5th Harmonic Terminal Voltage ($V_{h=5} = 0.1\angle\phi_{h=5}$ pu) & 12-Pulse Rectifier Load															
0	125	12.169	10.028	4.605	12.181	4.046	10.322	2.563	2.673	1.684	4.879	2.658	2.770	1.756	4.281
	100	12.506	10.027	4.615	12.157	4.054	10.303	2.404	2.638	1.536	4.559	2.495	2.735	1.603	4.007
	75	12.917	10.026	4.614	12.151	4.054	10.298	2.141	2.523	1.355	3.999	2.226	2.618	1.415	3.524
	50	13.363	10.008	4.600	12.102	4.042	10.259	1.726	2.183	1.178	3.007	1.799	2.270	1.232	2.663
	25	13.895	9.998	4.586	12.055	4.030	10.222	1.248	1.569	1.062	1.744	1.304	1.636	1.111	1.553
180	125	12.282	10.047	4.635	12.221	4.072	10.354	2.679	2.803	1.680	4.436	2.777	2.903	1.752	3.901
	100	12.505	10.032	4.621	12.173	4.060	10.316	2.505	2.813	1.507	4.195	2.600	2.913	1.572	3.693
	75	12.946	10.021	4.611	12.141	4.052	10.290	2.220	2.631	1.350	3.754	2.307	2.728	1.410	3.312
	50	13.482	10.023	4.606	12.132	4.047	10.283	1.743	2.307	1.200	2.931	1.817	2.396	1.255	2.596
	25	14.003	10.002	4.595	12.061	4.037	10.226	1.241	1.630	1.074	1.677	1.297	1.700	1.123	1.495
Case D4: Nonsinusoidal 20% of 5th Harmonic Terminal Voltage ($V_{h=5} = 0.2\angle\phi_{h=5}$ pu) & 12-Pulse Rectifier Load															
0	125	16.809	19.946	12.924	33.987	10.913	26.031	3.553	4.368	4.541	6.257	3.664	4.485	4.657	5.455
	100	16.984	19.933	12.911	33.943	10.903	26.002	3.684	4.301	4.491	6.109	3.797	4.417	4.607	5.329
	75	17.109	19.954	12.930	33.987	10.918	26.031	3.771	4.296	4.447	5.794	3.885	4.412	4.563	5.062
	50	17.172	19.956	12.929	33.976	10.917	26.024	3.913	4.269	4.163	5.267	4.028	4.385	4.279	4.613
	25	17.219	19.915	12.883	33.849	10.880	25.941	3.959	4.125	4.116	4.497	4.073	4.240	4.231	3.953
180	125	17.517	20.035	13.011	34.214	10.982	26.178	4.060	4.557	4.458	4.903	4.176	4.673	4.574	4.302
	100	17.278	20.037	13.010	34.207	10.981	26.173	4.085	4.542	4.437	5.009	4.200	4.659	4.554	4.392
	75	17.332	20.032	13.010	34.201	10.981	26.169	4.109	4.541	4.310	5.023	4.225	4.657	4.426	4.405
	50	17.370	20.032	13.001	34.166	10.974	26.147	4.090	4.430	4.159	4.845	4.205	4.546	4.275	4.252
	25	20.777	20.032	12.998	34.147	10.972	26.135	4.001	4.267	4.055	4.440	4.116	4.383	4.171	3.904
Case E: Sinusoidal Unbalanced Terminal Voltage (phase b voltage increased to 1.05 pu) & 12-Pulse Rectifier Load															
-	125	17.959	0.453	N/A	N/A	N/A	N/A	1.917	1.955	0.730	4.054	1.996	2.035	0.765	3.572
	100	21.428	0.414	N/A	N/A	N/A	N/A	1.641	1.798	0.564	3.701	1.711	1.873	0.592	3.266
	75	28.222	0.332	N/A	N/A	N/A	N/A	1.245	1.502	0.365	3.037	1.301	1.568	0.384	2.689
	50	30.941	0.249	N/A	N/A	N/A	N/A	0.727	1.021	0.197	2.001	0.762	1.069	0.207	1.781
	25	10.567	0.162	N/A	N/A	N/A	N/A	0.239	0.406	0.065	0.718	0.251	0.427	0.068	0.643
Case F: Sinusoidal Terminal Voltage & Asymmetric Nonlinear Load (phases a and b: half-wave diode rectifier, phase c: resistive load)															
-	125	37.713	0.245	N/A	N/A	N/A	N/A	11.217	11.044	4.175	10.891	11.080	10.920	4.291	9.285
	100	38.211	0.212	N/A	N/A	N/A	N/A	10.504	10.658	3.124	10.529	10.417	10.560	3.230	8.993
	75	38.265	0.155	N/A	N/A	N/A	N/A	9.360	9.788	2.022	9.607	9.342	9.746	2.104	8.241
	50	38.207	0.108	N/A	N/A	N/A	N/A	7.573	7.830	1.009	7.549	7.635	7.883	1.056	6.540
	25	37.902	0.056	N/A	N/A	N/A	N/A	5.245	3.760	0.276	3.488	5.358	3.873	0.290	3.081

*) 100% power level corresponds to rated transformer loading (assuming fundamental current component is at 1 pu).

**) Total harmonic distortion for transformer primary line current (THD_{ip}) and primary voltage (THD_{vp}). Due to core asymmetry and unbalanced operation, THD values in each phase differ, therefore, the worst phase THDs are shown.

***) Full aging results sets (conventional and proposed approaches) shown for transformer T4 (2 MVA, 25 kV/575 V) and condensed aging results (proposed approach only) shown for transformers T1-T3.

6.4.1 Sinusoidal voltage and linear loads

The transformers were simulated under ideal conditions with pure sinusoidal terminal voltages and resistive loads. As expected, the predicted aging based on the model and conventional WHF approach showed no loss of life due to no additional transformer losses and temperature rise in the absence of harmonic distortions (Table 6.2, row 2).

6.4.2 Terminal voltage distortions and linear loads

The effect of terminal voltage distortions on WHF and transformer aging is investigated for a balanced resistive load. The commonly occurring 5^{th} voltage harmonic was simulated at the transformer primary terminals with phase angles of 0 and 180 degrees at 5, 10 and 20% magnitude of the rated voltage. For harmonic magnitudes less than 5%, the aging estimation based on the nonlinear transformer model is predicted to be up to 1.1% loss of the rated life while the conventional approach predicts between 1 to 4% aging.

Higher harmonic levels greater than 10% result in significant increases in aging based on the conventional approach, but not so severe increases using the transformer model (up to 4.1% loss of life with 20% of 5^{th} harmonic). In these cases, the phase angle of the voltage harmonic has negligible impact (Table 6.2, rows 3-4).

6.4.3 Sinusoidal voltage and nonlinear loads

The previous case is repeated for pure sinusoidal terminal voltages with two different nonlinear loads connected at the transformer secondary. The loads consist of a 6-pulse diode rectifier and 12-pulse diode rectifier. The 12-pulse diode rectifier consists of two 6-pulse rectifiers connected in series which must be supplied from secondary and tertiary windings with star and delta connections in order to produce two 30-degree phase shifted three-phase voltage sets for the 12-pulse action.

Results indicate that under rated load currents with the 6-pulse rectifier load, the model based aging approach predicts approximately up to 6% loss of life (Table 6.2, row 5). The 12-pulse load results in a smaller loss of life (~3.5%) due to the load

current exhibiting less distortion (Table 6.2, row 6). On the other hand, for both cases the conventional WHF calculation shows negligible aging. This highlights a significant shortcoming of the conventional approach which in this case is only considering the sinusoidal terminal voltage and ignores the additional fundamental and harmonic losses caused by the nonsinusoidal load currents.

6.4.4 Terminal voltage distortions and nonlinear loads

The effect of terminal voltage distortions combined with the transformer serving the same nonlinear loads as before is investigated (Table 6.2, rows 7-10). Compared to the previous case, the predicted model based aging significantly increases to approximately 7% loss of life for rated loading with the 6-pulse rectifier with 10% of 5^{th} voltage harmonic. Again, the aging is not so severe for the 12-pulse rectifier load since the load current more approximates a sine wave versus 6-pulse rectifier (Figs. 6.3 and 6.4).

Unlike previous cases, the voltage distortions (magnitudes and phase shifts) have a noticeable interaction with the current harmonics generated by the nonlinear loads. This is indicated by the variation of the model based WHF which responds to changes in transformer losses when the phase angle of the 5^{th} harmonic is changed. The conventional WHF approach is much less sensitive to these changes as it does not consider the harmonic couplings and interactions of load, transformer and source distortions. The sensitivity of WHF for linear and nonlinear loads to phase angle of harmonics is depicted in Fig. 6.5.

Moreover, the conventional WHF calculations are insensitive to voltage harmonic phase-angles according the conventional WHF definition of (6.2). For the same reasons, the conventional WHF does not respond significantly to changes in load level which leads to false aging prediction for lighter loads. The proposed aging method accurately factors in load levels, transformer nonlinearities and current-voltage harmonic interactions in the loss computations of the transformer model.

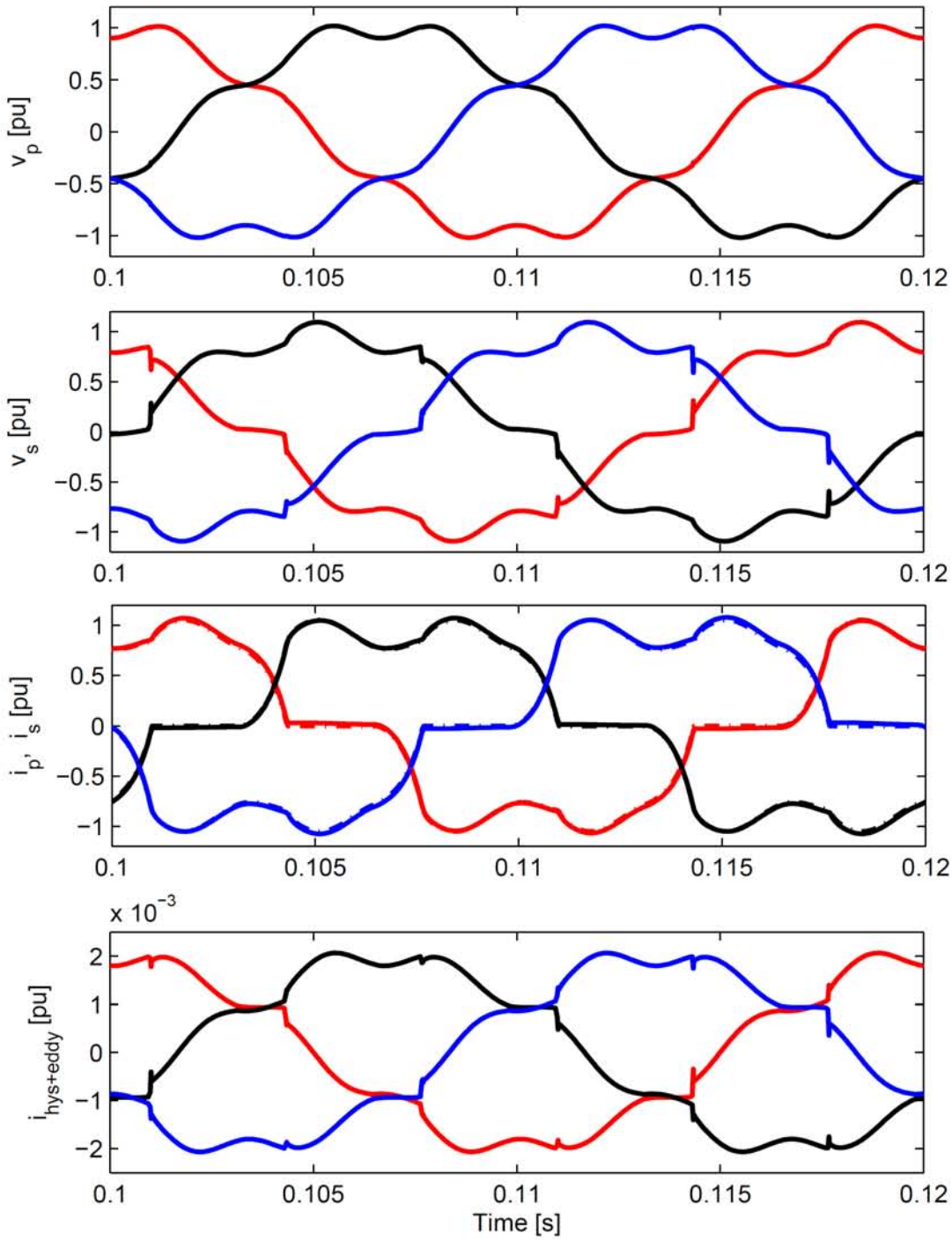

Fig. 6.3. Transformer waveforms for terminal voltage harmonics (5% of 5th harmonic at a phase angle of 0 degrees) with nonlinear load (6-pulse rectifier). Primary and secondary winding voltage and currents as well as core-loss currents are shown in per-unit of peak rated values.

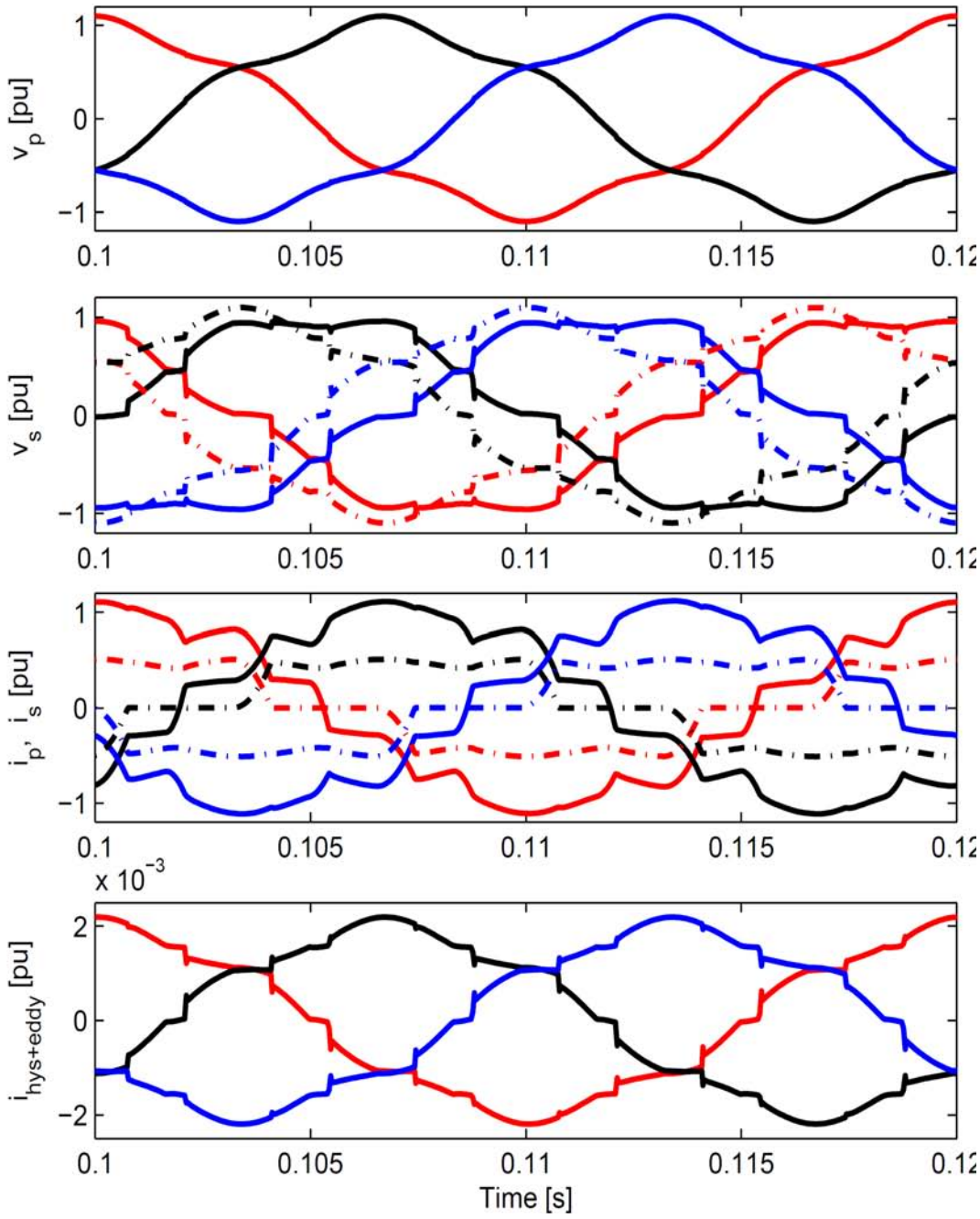

Fig. 6.4. Transformer waveforms for terminal voltage harmonics (5% of 5th harmonic at 0 degrees phase shift) with nonlinear load (12-pulse rectifier). Primary/secondary voltages and currents are shown in per-unit of peak rated values. Secondary and tertiary windings are necessary for the 12-pulse rectification action and therefore exhibit different harmonic contents due to the 30 degree phase shift in the star and delta connected windings.

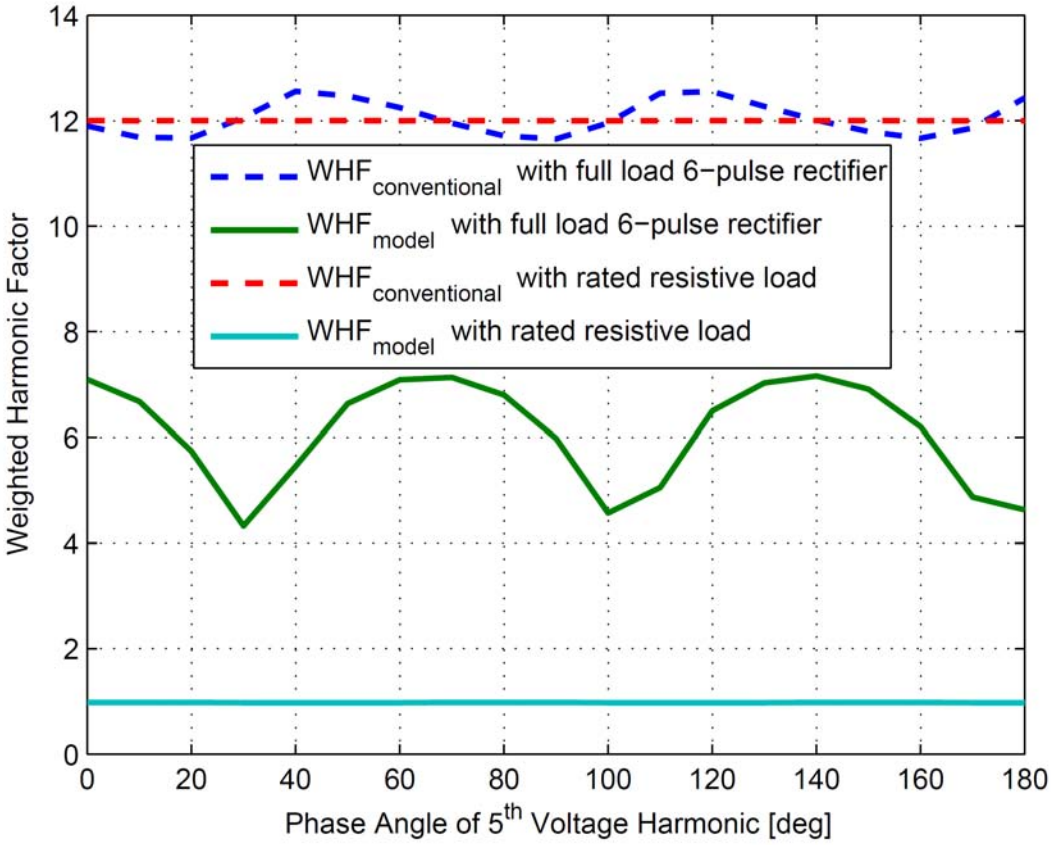

Fig. 6.5. Influence of voltage harmonic phase angle for 10% of 5th harmonic on WHF computed by conventional and nonlinear modelling approaches for linear and nonlinear loads. The large variances in WHF under nonlinear loads indicate a notable interaction between the terminal voltage and load current harmonics which impact the overall transformer additional losses.

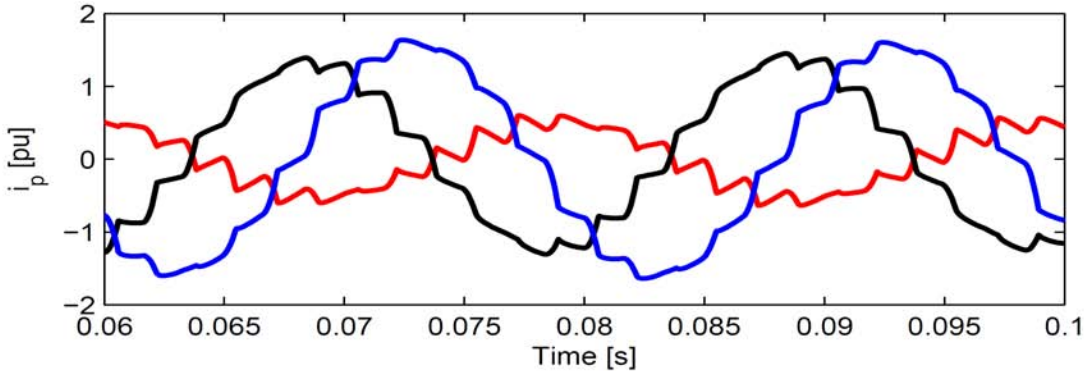

Fig. 6.6. Transformer primary winding currents for unbalanced sinusoidal voltages (phase b voltage is 5% above nominal) and 12-pulse rectifier load.

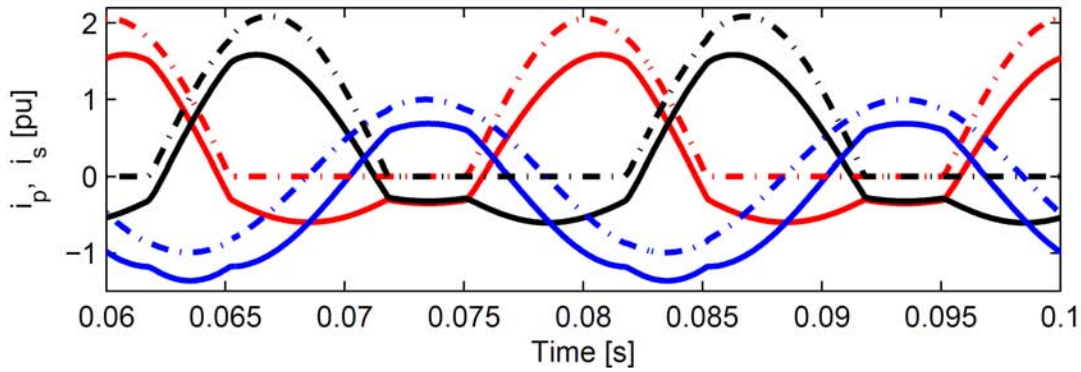

Fig. 6.7. Transformer primary (solid lines) and secondary (dashed lines) winding currents for unbalanced linear and nonlinear loads (phase a: half-wave rectifier, phase b: half-wave rectifier and phase c: resistive load).

6.4.5 Unbalanced supply with nonlinear load

Voltage imbalance in power systems is a common occurrence due to unbalanced single-phase loads, poor transmission line transpositions, unsymmetrical capacitor bank switching and single-phase faults. Furthermore, the three-leg core structure itself is also a source of imbalance with different centre and outer leg (phase) nonlinear reluctances. Such operation can unbalance the voltages and mmfs developed in the transformer electromagnetic circuit which leads to a nonuniform loss distribution in the transformer windings and core. Unbalanced voltage condition is simulated by increasing phase *b* voltage to 5% above nominal while the transformer is supplying a 12-pulse rectifier load. This results in unbalanced line currents and harmonic distortions in each phase as shown in Fig. 6.6. The resulting aging is computed to be over 3% loss of service life at full continuous load. In such a case, the conventional WHF approach is invalid as there is no consideration for multi-leg asymmetric core geometries, non-uniform core losses and phase imbalance of transformer mmfs.

6.4.6 Asymmetric nonlinear loads

An asymmetric load condition is simulated with unbalanced linear and nonlinear loads that result in the propagation of different harmonic currents in each phase. This

is of significance for new loading patterns expected for example by Plug-in Electric Vehicles (PEVs) which are growing in popularity [118, 119]. PEVs will employ single-phase ac/dc converters for battery chargers that may cause unbalanced single-phase distortions in residential networks. This was investigated by placing two single-phase half-wave diode rectifiers on phases *a* and *b* with a resistive load on phase *c*. The full-load transformer current waveforms are shown in Fig. 6.7 which contributes to a drastic increase in WHF and transformer aging (over 9% loss of life) as predicted by the nonlinear model. As in the previous case, the conventional WHF aging calculation is not applicable for asymmetric transformer operating conditions.

6.5 CONCLUSION

This study presents a new approach to the calculation of transformer aging in asymmetric three-phase three-leg transformer cores with (un)balanced (non)sinusoidal excitation and (non)linear (a)symmetric loading. The proposed approach improves upon the accuracy of calculating weighted harmonic factor (WHF) through accurate transformer loss modelling considering (un)balanced (non)linear loads, terminal voltage imbalances and harmonics. The loss modelling is based on a nonlinear three-phase three-leg transformer model which features the inclusion of magnetic flux couplings and dynamic core hysteresis effects in asymmetric multi-leg core structures. For comparison, aging estimations are carried out for four types of three-phase three-leg transformers. The main conclusions are:

- The proposed aging technique is applicable to a wider range of transformer operation versus the conventional WHF aging estimation that only considers rated single-phase and rated balanced three-phase conditions.
- The proposed model based aging calculations properly consider the internal transformer nonlinearities combined with the operating environment that includes grid disturbances (e.g., odd and even harmonics with imbalances) and load characteristics (e.g., (non)linear (un)balanced behaviour).

- The loss behaviour and resulting aging are shown to not only be influenced by the magnitude of the voltage harmonic, but also the phase angle. The effect is more pronounced for nonlinear loads as there is a crucial interaction between the voltage and current harmonic magnitudes with phase-shifts that is not considered in the conventional WHF definition.
- Results indicate that unbalanced nonlinear loads with different harmonic levels in each phase can cause a significant rise in transformer aging. This is of concern for new unbalanced single-phase loading conditions such as Plug-In Electric Vehicles now appearing in distribution systems and smart grids which employ nonsinusoidal ac/dc battery chargers circuitry.
- Based on the premature aging results for four types of transformers (Table 6.2), it is recommended to perform more frequent maintenance and monitoring of distribution transformers with (non)sinusoidal terminal voltages with imbalances and asymmetric linear/nonlinear loading conditions. An evolving situation is the loading of power transformers in smart grid configurations with unbalanced (single-phase) charging of plug-in electric vehicles (PEV) in residential feeders and three-phase nonlinear PEV charging stations in distribution networks
- The modelling approach relies on electric and magnetic equivalent circuits that could be modified to perform aging estimations for other electrical machines (e.g., five-leg transformer core and induction machines).

Chapter 7. Transformer operational issues in future smart grids with plug-in electric vehicles

7.1 INTRODUCTION

The power networks industry is on the verge of a revolutionary transformation that has not been experienced since the founding of the electricity system in the late 1800s. Reminiscent of the "War of Currents" debate [120-126] that took place over a century ago about the merits of ac versus dc transmission systems, a massive network overhaul toward a "smart grid" is currently being considered [127-132]. This debate is very much apparent in industry and research communities through many recent conferences held and new research journals opened on this subject over the last 3 years.

Indeed, many governments are allocating significant resources in exploring this new frontier as the electrical energy market is fundamental to many countries economic growth. In lieu of these new developments, it is worthwhile to investigate possible future smart grid operational scenarios and the corresponding demands imposed on power system components operating within a smart grid system. To that end, this chapter looks at the importance of transformer performance considering smart grid related operations such as coordinated and uncoordinated PEV battery charging.

7.1.1 Smart grids

The smart grid is a new term that refers to a broad collection of technologies aiming to transform the electricity network to become more flexible, economic, reliable, secure and efficient [133]. It is being heralded as the new paradigm for future designs of power transmission and distribution systems for the 21st century. While aiming to improve energy efficiency and reliability [134, 135], it is also to function toward improving security of customer supply with self-healing and automatic

reconfiguration of the grid in response to electrical disturbances, natural disasters, or malicious activity [130, 136].

Traditional distribution grids based on century old design philosophies must be updated to contend with flexible grid operations and new energy requirements of the future [128, 131, 132]. This is particularly relevant in the current trend toward deregulating power industries, promoting new energy marketing opportunities, increasing integration of renewable energy sources, and new loading patterns expected such as battery charging of multiple Plug-In Electric Vehicles (PEVs) in residential networks. Due to these new challenges, it must be expected that the transition to smart grids will likely lead to new transformer operational performance issues as investigated in this study.

The backbone of a smart grid is envisaged to be a bi-directional communications network providing the framework for real-time monitoring and control of transmission, distribution and end-user consumer assets. This includes demand-side management functions with smart metering, sensors and load control of smart appliances for effective coordination and usage of available energy resources [118, 137, 138]. Although these functions are the core of future smart grid operations, it should be noted that concepts such as automation in load management and extending SCADA monitoring and control to the distribution and consumer level have already been developing as early as the 1980s [139, 140]. These efforts are now being accelerated with renewed interest and momentum under the smart grid mantra. To that end, this research explores some of these new developments for its potential in affecting distribution transformer lifecycle performance.

7.1.2 Utility challenges in smart grids and plug-in electric vehicles

PEV charging is likely to take place in public or corporate car parks, electric charging stations, or at a customer's premises [141]. From the utilities point of view, the adoption of PEVs into distribution systems represents a number of challenges and potential network reliability issues [131, 142]. Many questions arise such as to whether or not the infrastructure is capable of supporting mass PEV charging and

what the alternatives are to costly upgrades of network assets. Even without PEVs, many countries distribution systems are frequently overloaded (e.g., hot climate areas with increased air-conditioned usage). Adding PEVs to this already fragile situation may severely stress the distribution system beyond their capacities. Smart grid technologies such as coordinated smart charging are being explored as a possible solution to managing the PEV charging problem [118, 141].

The main problem from the utilities perspectives is that PEV battery chargers represent a sizeable and unpredictable load. As PEV battery capacities continue to increase, so do the ratings of the PEV chargers. In great numbers, PEV chargers could significantly stress local neighbourhood distribution circuits. Distribution transformers, which are the weakest link in residential grids, could become the bottleneck for network congestion thereby becoming heavily loaded thus increasing the likelihood of equipment failure potentially blacking out entire suburbs. A quite plausible scenario is that numerous PEV owners will arrive home from work within a narrow time period and immediately plug-in their vehicles to charge during a time of already high peak demand. These uncoordinated and random charging activities could significantly stress the distribution system causing severe voltage fluctuations, suboptimal generation dispatch, degraded system efficiency and poor economy. In view of these future loading patterns, this study focuses on the impacts of uncoordinated and coordinated PEV charging with particular emphasis on transformer loading issues.

7.2 STUDIED SMART GRID DISTRIBUTION SYSTEM

A smart grid system study considering coordinated and uncoordinated PEV charging is carried out in the steady-state using modified load flow algorithms coded in a MATLAB programming environment [143]. Different types of PEV battery charging scenarios are programmed to evaluate the corresponding power flow patterns and their impacts on transformer operation. In the following case studies, extensive simulations have been performed for a large and realistic distribution system

topology with varying penetrations and random plugging in of PEVs. This section describes the implemented test system configuration simulating a smart grid as well as PEV battery and charger characteristics, system loads and the justifications for the assumptions necessary for the analysis.

7.2.1 System under study

A large test system consisting of a main high voltage feeder (23 kV) with several low voltage networks (415 V) is implemented in the study. The high voltage feeder is a 30 bus test system [144] combined with several low voltage sections based on a typical 53 node 415 V residential system in Western Australia (WA) [145]. Each node of the low voltage networks represents individual households where vehicles

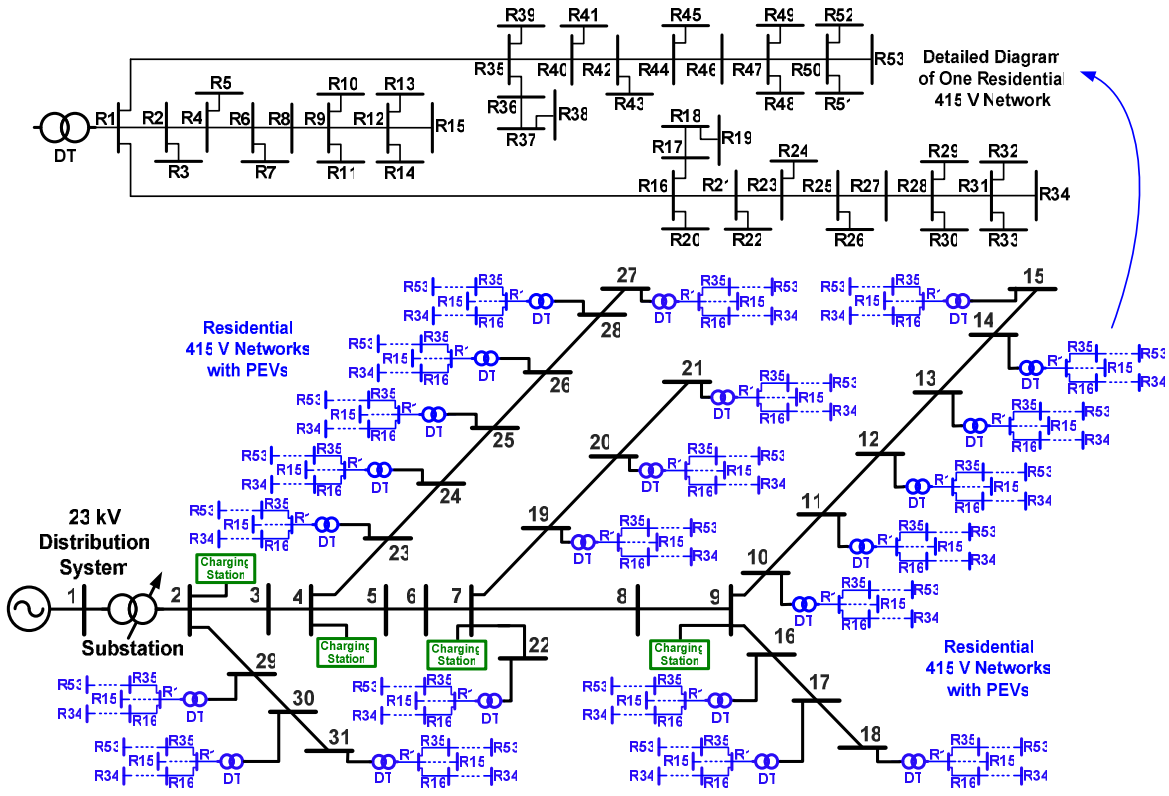

Fig. 7.1. The 1200 node smart grid distribution system consisting of a 23 kV 30 bus test system connected to low voltage 415 V networks (53 nodes each) through 22 distribution transformers (DT-10 to DT-31) populated with PEVs.

may plug in for charging (Fig. 7.1). There are a total of 22 low voltage residential networks supplied from the main 23 kV high voltage buses via 100 kVA distribution transformers. This system has a total of 1200 nodes which is implemented using the MATLAB software package. The data for this system is listed in Appendix D.

7.2.2 Load profile for residential households

Typical household load profiles without PEV loads (Fig. 7.2) are simulated over the course of a day based on actual recordings from a distribution transformer in Western Australia's South-West Interconnected System (SWIS). A constant power factor of 0.9 is assumed with an average house peak demand of 1.5 kW.

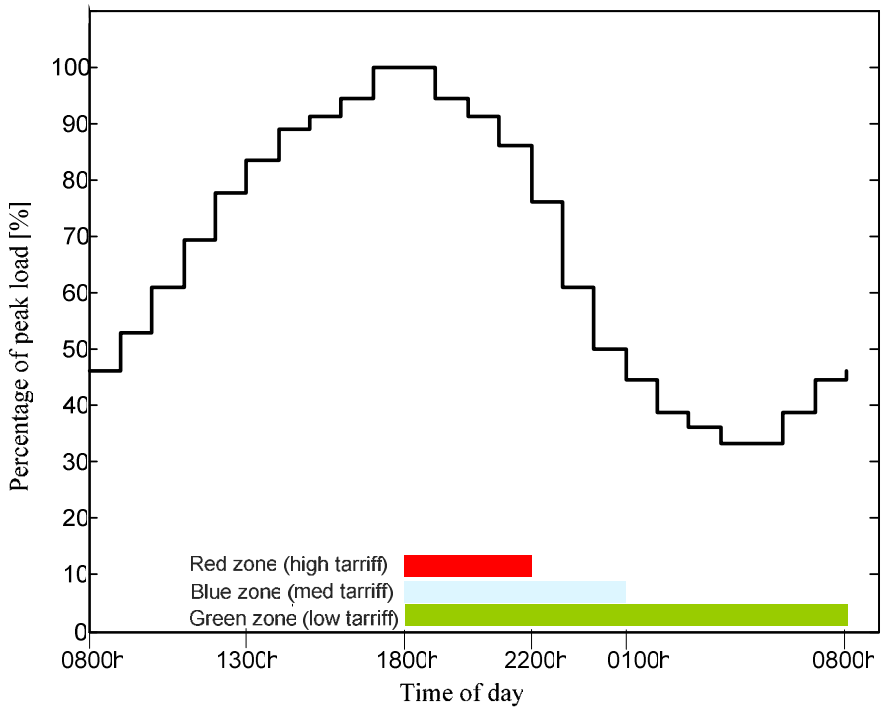

Fig. 7.2. Typical daily load curve for Western Australian residential networks for modelling household daily load variations (without PEVs).

7.2.3 Plug-in electric vehicles charger load profile

Based on currently available PEVs on the market, each PEV battery is assumed to have a maximum storage capacity of 10 kWh [9]. A depth of discharge of 70% of the

rated battery capacity is assumed as is typically expected for prolonging charging cycles and battery life expectancy. Therefore, 8 kWh of energy is required per PEV battery bank, given a typical charging efficiency of 88% [10].

7.2.4 Ratings of PEV chargers

A 4 kW rating for internal PEV battery chargers that can be plugged into residential household supply is assumed with a unity power factor. This charger rating is within the capability of most modern day residential circuits and wiring standards (e.g., in Western Australia) which can typically carry 10 to 20 amps from a single phase 230 V supply. Therefore, next to air-conditioning, PEV charger loads are expected to be one of the most dominant loads in PEV owner households [11]. Rapid charging is a feature also offered in some PEV models, but it is not considered in this analysis as it would require reinforcement of household wiring and an external battery charger connection with a significantly higher power rating (e.g., from rapid-charge stations or three-phase connections).

7.2.5 PEV penetrations and priority charging time zones

Random and uncoordinated PEV charging for different PEV penetration levels of 17%, 31%, 46% and 62% are simulated which reflects different charging power levels and loading patterns in the near or long-term future. The PEV penetration level is defined as the ratio of the total number of PEV nodes to the total number of low voltage nodes (households).

7.2.6 Distribution transformers

The loading patterns of the multiple 100 kVA 22kV/415V distribution transformers supplying neighbourhoods with PEVs in the test system are of interest in this study. The selected transformer ratings and impedance values are representative of presently in-service distribution transformer types used in Western Australia. The system and transformer impedance data are listed in Appendix D. A small inconsistency is noted here in that the implemented 30 bus test system [144] is a 23 kV feeder whereas in Western Australia, similar type feeders operate at a lower

nominal voltage of 22 kV, hence the 22 kV/415 V transformer. This difference in voltage level should not have a noticeable impact on the study results and hence 23 kV voltage level is maintained throughout the simulations in accordance with the 30 bus test system in [144].

7.3 DISTRIBUTION TRANSFORMER LOADING WITH MULTIPLE UNCOORDINATED PEV CHARGING ACTIVITY

In the following case study, random and uncoordinated plugging in of PEVs for charging is simulated. The random arrivals and plugging-in times follow a normal distribution simulated for three different time spans throughout the day as follows:

1800h-2200h: This time zone is representative of PEV owners who immediately, or after some fixed time delay, plug-in their electric vehicles to charge on arrival from work at the end of the day. This is a realistic time span which coincides with most of the residential on-peak demand period.

1800h-0100h: Rewards and incentives schemes (e.g., cheaper electricity prices during off-peak hours) could persuade PEV owners to charge their electric vehicles later in the evening at partially off-peak times. Therefore, a wider range of uncoordinated and randomised time distribution of PEV charging is considered in this time span.

1800h-0800h: This case investigates a highly dispersed time distribution of random PEV charging where night time off-peak charging also occurs.

Based on 24 hour load flow analysis with simulated random PEV plug-in activity, the resulting system loading patterns, voltage profiles and individual distribution transformer load currents are computed (Figs. 7.4-7.11 and Tables 7.3-7.4).

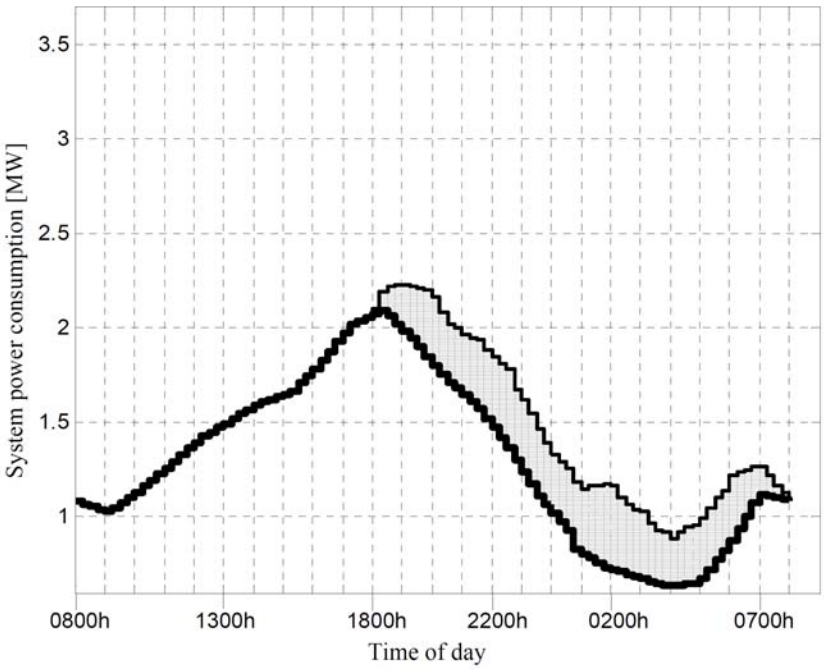

Fig. 7.3. System demand with random uncoordinated PEV charging (47 % PEV penetration) occurring between 1800-0800 hrs (thick line: no PEV curve).

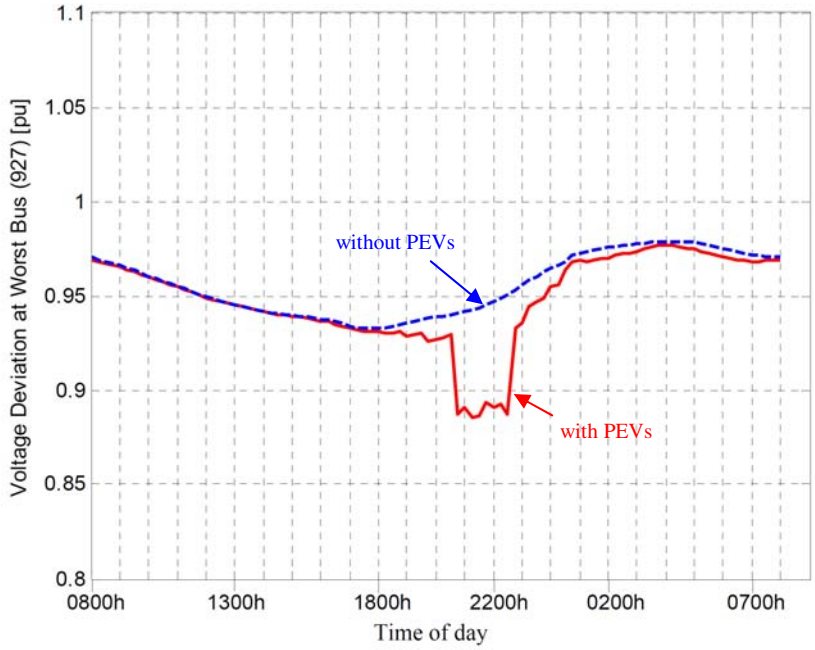

Fig. 7.4. Voltage profile at worst node (17-R48) for random uncoordinated PEV charging (47 % PEV penetration) occurring between 1800-0800 hrs.

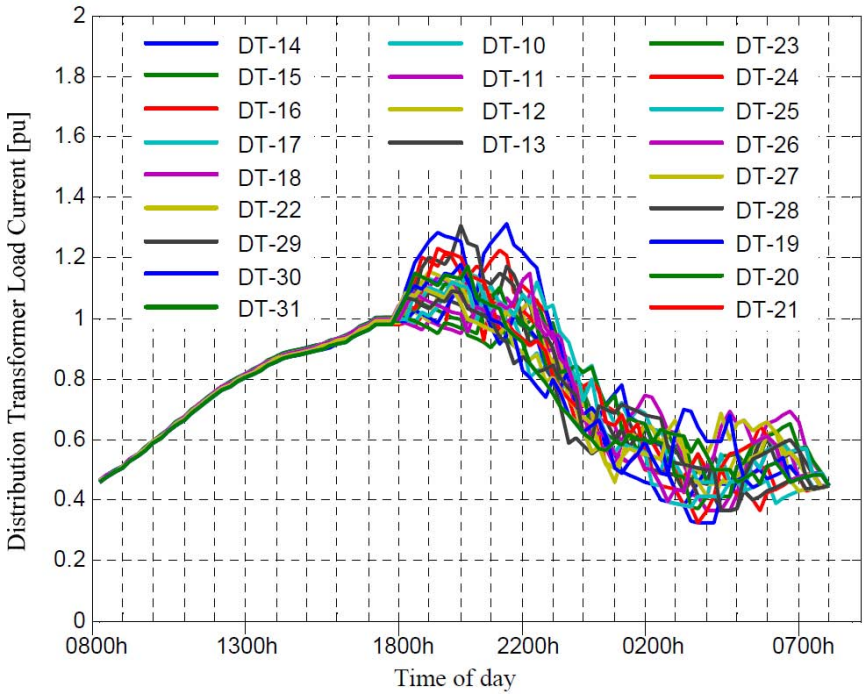

Fig. 7.5. Daily load currents in all 22 distribution transformers with random uncoordinated PEV charging occurring between 1800-0800 hrs.

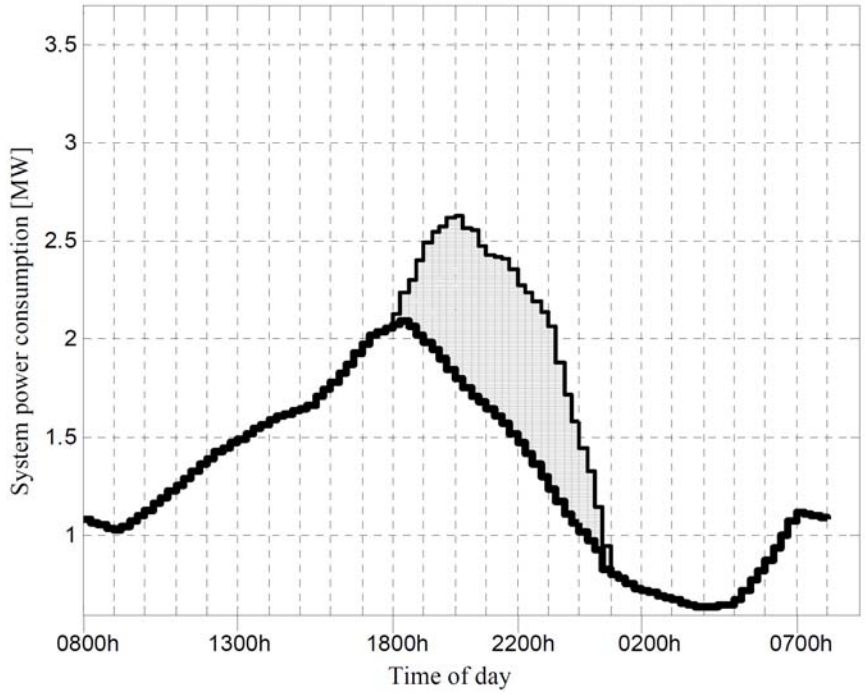

Fig. 7.6. System demand with random uncoordinated PEV charging (47 % PEV penetration) occurring between 1800-0100 hrs (thick line: no PEV curve).

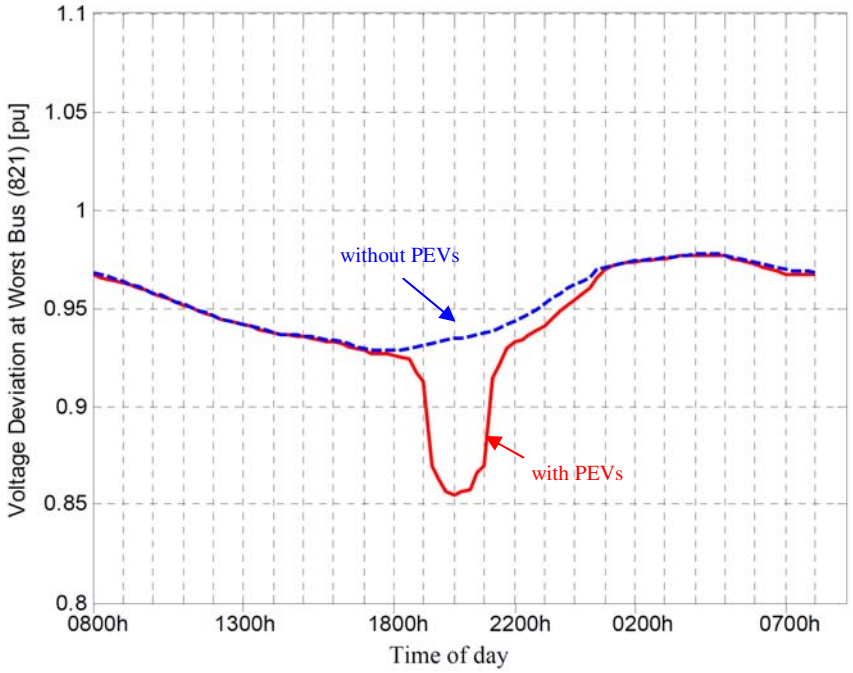

Fig. 7.7. Voltage profile at worst node (15-R48) for random uncoordinated PEV charging (47 % PEV penetration) occurring between 1800-0100 hrs.

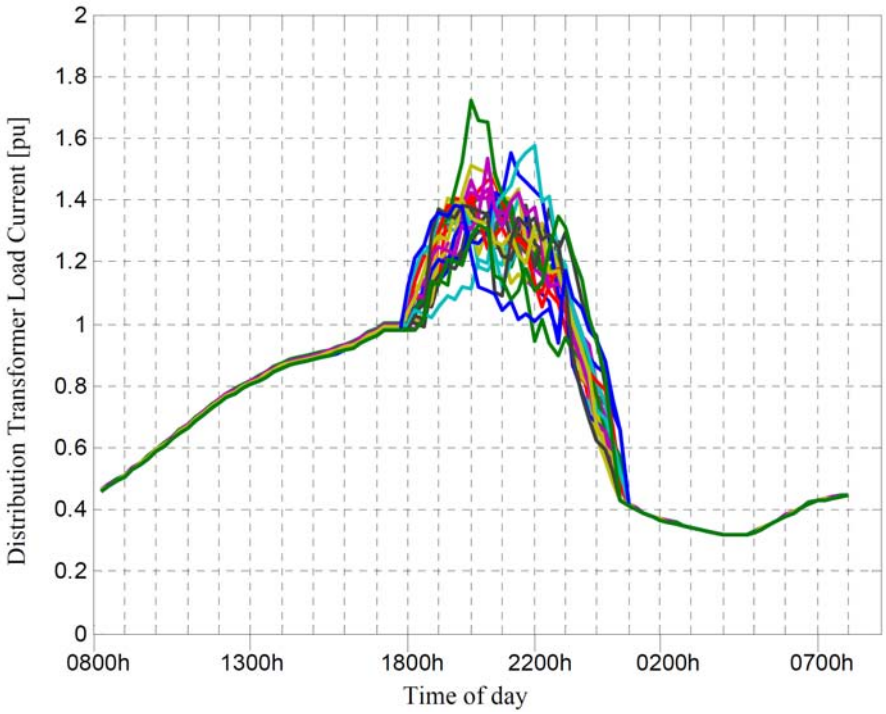

Fig. 7.8. Daily load currents in all 22 distribution transformers with random uncoordinated PEV charging occurring between 1800-0100 hrs.

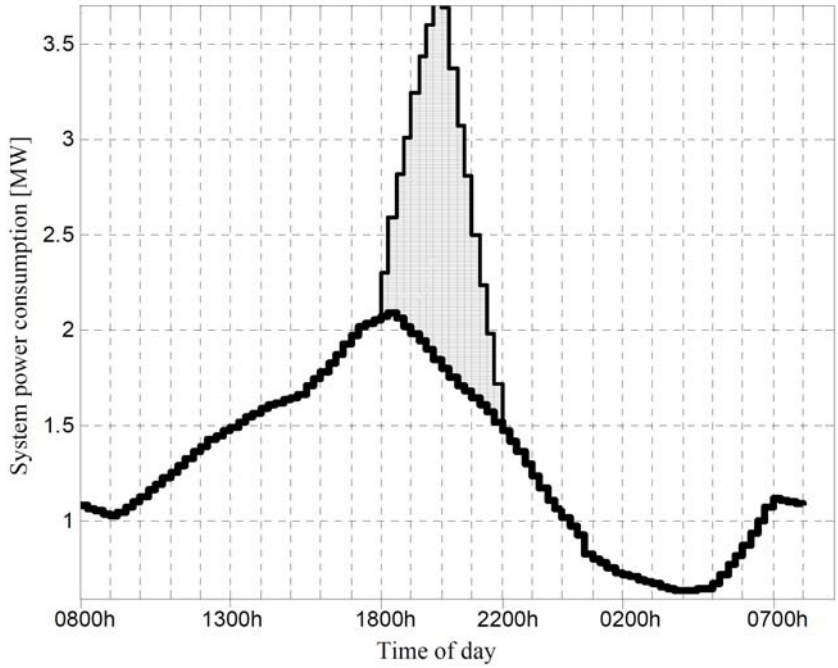

Fig. 7.9. System demand with random uncoordinated PEV charging (47 % PEV penetration) occurring between 1800-2200 hrs (thick line: no PEV curve).

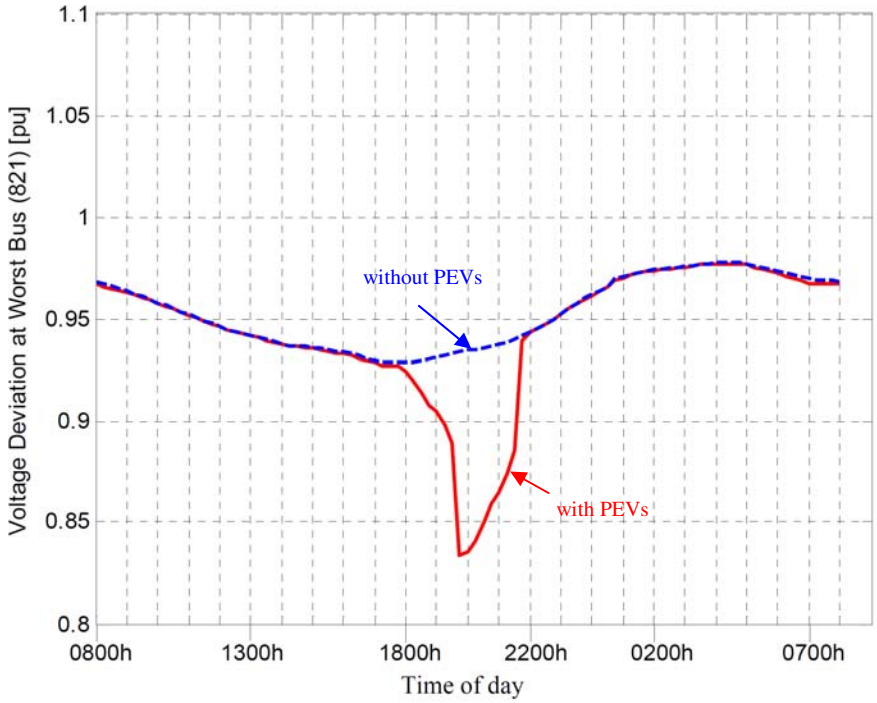

Fig. 7.10. Voltage profile at worst node (15-R48) for random uncoordinated PEV charging (47 % PEV penetration) occurring between 1800-2200 hrs.

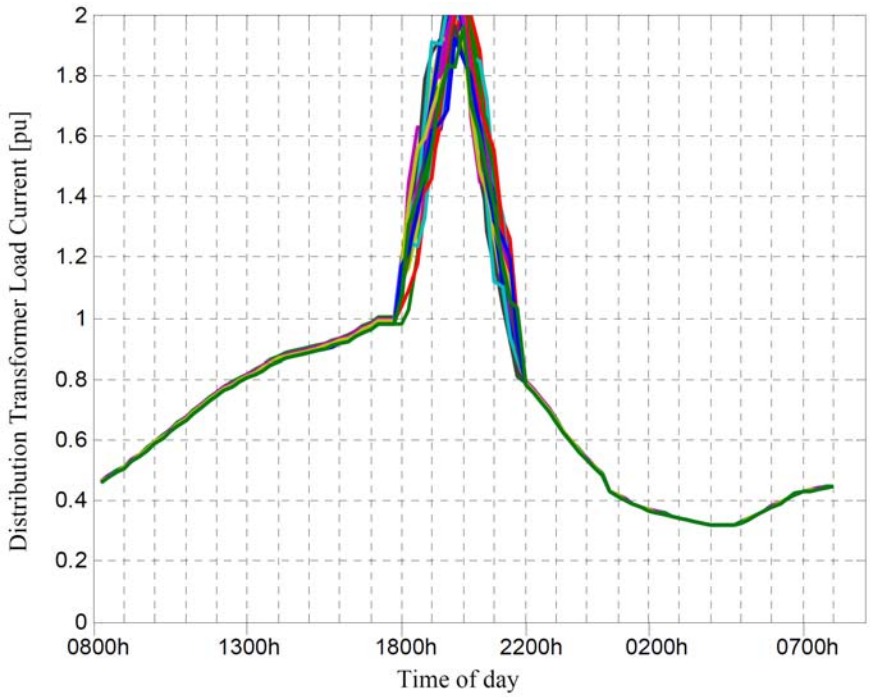

Fig. 7.11. Daily load currents in all 22 distribution transformers with random uncoordinated PEV charging occurring between 1800-2200 hrs.

Table 7.1
Transformer load currents with random uncoordinated charging for different PEV penetrations and time spans.

PEV (%)	I_{max} (pu)*	I_{min} (pu)*	I_{avg} (pu)**
No PEVs			
0	1.00 (DT-15 @ 18:15 hrs)	0.3192 (DT-29 @ 04:00 hrs)	0.6560
Random Uncoordinated PEV Charging occurring between 1800-0800hrs			
17	1.1017 (DT-17 @ 19:00hrs)	0.3192 (DT-29 @ 04:00hrs)	0.6905
31	1.1528 (DT-26 @ 19:45hrs)	0.3216 (DT-17 @ 04:15 hrs)	0.7179
46	1.3147 (DT-19 @ 21:30 hrs)	0.3220 (DT-14 @ 04:00 hrs)	0.7489
62	1.4587 (DT-20 @ 19:45 hrs)	0.3659 (DT-20 @ 04:30 hrs)	0.7804
Random Uncoordinated PEV Charging occurring between 1800-0100hrs			
17	1.2240 (DT-13 @ 19:30 hrs)	0.3192 (DT-29 @ 04:00 hrs)	0.6913
31	1.3624 (DT-31 @ 20:30 hrs)	0.3192 (DT-31 @ 04:00 hrs)	0.7196
46	1.7230 (DT-15 @ 20:00 hrs)	0.3192 (DT-29 @ 04:00 hrs)	0.7515
62	1.8819 (DT-12 @ 21:00 hrs)	0.3192 (DT-29 @ 04:00 hrs)	0.7845
Random Uncoordinated PEV Charging occurring between 1800-2200hrs			
17	1.3773 (DT-12 @ 19:30 hrs)	0.3192 (DT-29 @ 04:00 hrs)	0.6919
31	1.7385 (DT-11 @ 19:45 hrs)	0.3192 (DT-29 @ 04:00 hrs)	0.7212
46	2.1684 (DT-13 @ 19:45 hrs)	0.3192 (DT-29 @ 04:00 hrs)	0.7542
62	2.5788 (DT-14 @ 19:45 hrs)	0.3192 (DT-29 @ 04:00 hrs)	0.7891

*) Load currents in per-unit of peak rms transformer load with no PEVs
**) Daily average of all transformer load currents

Table 7.2
Voltage performance with random uncoordinated charging for different PEV penetrations and time spans.

PEV (%)	V_{worst} (pu)	V_{avg} *(pu)	Worst Node	Worst Time**
No PEVs				
0	0.9225	0.9729	15-R33	18:15 hrs
Random Uncoordinated PEV Charging occurring between 1800-0800hrs				
17	0.88362	0.97134	14-R48	18:30 hrs
31	0.87091	0.97035	16-R14	18:30 hrs
46	0.88543	0.96955	17-R48	21:30 hrs
62	0.86302	0.96852	11-R52	18:30 hrs
Random Uncoordinated PEV Charging occurring between 1800-0100hrs				
17	0.88004	0.97129	14-R48	20:00 hrs
31	0.86213	0.97025	12-R14	19:00 hrs
46	0.85499	0.9694	15-R48	20:00 hrs
62	0.82929	0.96828	12-R52	20:45 hrs
Random Uncoordinated PEV Charging occurring between 1800-2200hrs				
17	0.87315	0.97126	15-R48	19:45 hrs
31	0.83628	0.97016	15-R14	20:00 hrs
46	0.83336	0.96926	15-R48	19:45 hrs
62	0.79416	0.96803	14-R52	19:45 hrs

*) Daily average of all node voltages
**) Time at which worst voltage occurs (to the nearest 15 minutes)

Uncoordinated multiple PEV charging patterns and their effects on individual distribution transformer load currents and network voltage profiles are shown in Figs. 7.3-7.11 and summarised in Table 7.1. For multiple PEV charging activity occurring randomly within the time period 1800-0800 hrs, transformer load peaks up to 15% above the nominal no-PEV current for PEV penetrations up to 31%. This highly diversified random charging pattern is a possible but unlikely scenario unless some form of control or reward incentives is implemented to encourage night time charging. Nevertheless, it is worthwhile considering these effects if PEV chargers could conceivably be programmed to randomise their activation, having the advantage of not requiring smart grid communications infrastructure. As indicated in Table 7.1, such randomisation could diversify the PEV charger loads enough to avoid severe transformer stresses for low PEV penetrations. However, for higher PEV penetrations, even with diversified random charging over a wide time distribution of 1800-0800 hrs, transformer rms currents peak to over 45% above nominal no-PEV currents.

A more realistic uncoordinated PEV plugging-in scenario is simulated where charging occurs within a narrower time distribution of 1800-0100 hrs. This less diversified pattern is because PEV owners are expected to arrive home after work hours with the bulk of PEVs plugging in during peak time and gradually decreasing in plug-in rate toward the late evening (Figs 7.6-7.8 and Table 7.1). Results indicate that transformer peak load currents increase from 22 to 88% for PEV penetrations from 17 to 62%, respectively, and significant voltage drops become apparent in the low voltage networks. Further narrowing the time distribution of random PEV plug-in events to 1800-2200 hrs results in even more network congestions and severe loading conditions. For low PEV penetrations of 17% to 31%, the transformer load current varies significantly from 37 to 74% above nominal no-PEV transformer load currents because the uncoordinated PEV charging coincides more with the peak residential load demand. This raises grave concerns of significant stress on distribution circuits and transformers with the prospect of more frequent and costly network upgrades.

7.4 DISTRIBUTION TRANSFORMER LOADING WITH COORDINATED PEV CHARGING ACTIVITY

Several recent studies over the past two years have proposed novel methods of coordinating multiple PEV battery chargers in residential systems as opposed to allowing PEVs to charge immediately upon connection in an uncoordinated manner. These methods consider the performance of the system as a whole based on heuristic and optimisation methods. A recently proposed PEV charging coordination approach offers to minimise network congestions, operational costs and power losses based on maximum sensitivities selection (MSS) optimisation [119, 141, 146-148]. This MSS smart charging coordination approach is implemented in this study to decide which PEVs begin charging and at what time [119, 147]. Unlike other methods, this approach considers PEV owner subscriber charging priorities in the coordination problem and can be applied to very large systems. The focus of this analysis is on

transformer operation with multiple PEV charging activity over a 24 hour period. This section gives a brief overview of the implemented smart charging approach; however the finer details of the coordination algorithm are omitted for the sake of brevity but can be found in recently published related articles [119, 147, 149, 150].

7.4.1 PEV charger coordination constraints

An important factor in distribution system operation is the regulation of voltages within acceptable limits. The implemented charger coordination strategy has included the voltage limits as a constraint in the algorithm. The voltage limits are set to ± 10% ($V^{\min} = 0.9pu$ and $V^{\max} = 1.1pu$) which is typical of many distribution systems,

$$V^{min} \le V_k \le V^{max} \quad for\ k = 1,..,n. \tag{7.1}$$

where k is the node number and n is the total number of nodes.

A second constraint is to prevent the occurrence of a system overload condition that may be caused by PEV charging. Therefore, the total maximum system demand of the distribution system is specified such that total power consumption at each time step h ($\sum_{\text{Demand}}^{\text{h}}$) is limited to the peak demand level (D_{max}) that would normally occur without any PEVs charging in the residential networks.

$$\sum Demand^{\,h} = \sum_{k=1}^{n} P_{k,load}^{h} \le D_{max}, \quad for\ h = 1,...,24. \tag{7.2}$$

This has a direct impact on the loading of the main substation transformer supplying the 1200 node smart grid distribution system.

7.4.2 Coordination objectives

The minimisation of system demand and total system power losses for the PEV charging time is the main objective of this coordination algorithm. This also has a direct impact on maximising distribution system economy by limiting the cost of energy that would otherwise be expended on cable and transformer losses. In order to achieve this, the following objective function is used:

$$min \sum_{h=h_{start}}^{h_{end}} Demand^{h} = min \sum_{h=h_{start}}^{h_{end}} \sum_{k=1}^{n} P_{k,load}^{h} \quad (7.3a)$$

where h_{start} and h_{end} correspond to the starting and ending charging times within the selected charging time zone, respectively and $P_{k,load}^{h}$ is the load demand of node k at time step *h*. The loss minimisation objective is defined as the minimisation of incremental system losses over 24 hours:

$$min\ W_{loss} = \sum_{h=1}^{24} P_{loss}^{h} \quad (7.3b)$$

Based on Newton-based power flow outputs, the power losses of the distribution system are computed from line losses in sections between nodes k and k+1 is

$$P_{loss(k,k+1)} = R_{k,k+1}\left(\left|V_{k,k+1} - V_k\right| y_{k,k+1}\right)^2 \quad (7.4)$$

and the total power loss is

$$P_{loss} = \sum_{k=0}^{n-1} P_{loss(k,k+1)} \quad (7.5)$$

7.4.3 PEV penetrations and priority charging time zones

Four PEV penetration levels of 17%, 31%, 46% and 62% are simulated. For each penetration level, PEVs are grouped into three priority time zones (e.g., red, blue and green zones) which PEV owners can subscribe to depending on how soon they want their vehicles charged:

- **Red charging zone** (1800h-2200h)- is for high priority PEV owners wanting to charge their PEVs as soon as possible upon return from work in order to have their vehicles ready for use later in the evening. As this charging zone is coinciding with most of the on-peak period, PEV owners that wish to subscribe for high priority on-peak charging will pay a higher tariff rate.
- **Blue charging zone** (1800h-0100h)- is offered for medium priority PEV owners that prefer to charge their vehicles at partially off-peak periods and

pay a lower tariff rate than the red zone.

- **Green charging zone** (1800h-0800h)- is the low priority period that most PEV charging is expected to take place since most (low priority) consumers will require their vehicles fully charged for use throughout the next day. PEV charging during this zone covering off-peak periods will be highly encouraged by setting the cheapest tariff rate.

In this study, the priority groups and residential nodes designated with PEVs are randomly allocated.

7.4.4 Newton-based power flow approach

The implemented PEV charger coordination approach makes use of a modified Newton-based load flow routine to assess the state of the distribution system subject to PEV charging. This includes the evaluation of voltage profile and power losses, which is necessary for the computation of the objective function and checking of constraints. Constant power load models are used with their real and reactive powers updated through a load curve for each time interval of the day the load flow is computed. In a real smart grid system, it is anticipated that sophisticated state estimation techniques and smart metering will obtain the necessary inputs for implemented coordination algorithms.

7.4.5 Smart coordinated PEV charging algorithm

This study assumes a smart grid communication infrastructure is in place to sense PEV connections to the grid and transmit control signals to individual chargers with the devised real-time coordination strategy. The algorithm attempts to charge PEVs as soon as possible based on their designated priorities while considering network operational criteria (e.g., maximum system load, voltage regulation and loss minimisation) through the defined objective functions and constraints.

The coordination algorithm searches from the highest priority group of PEVs (e.g., red) and finds the ideal time to schedule PEV charging such that system losses are minimised (Eq. 3). The order of vehicle charging is selected based on the maximum

sensitivity selection (MSS) optimisation approach [119, 151]. This approach checks the sensitivity of each PEV nodes voltage and power loss behaviour to PEV charger activation. The PEV node for each priority group corresponding to the least impact on power losses and voltage deviation is selected for charging. This search process continues from high to low PEV priorities until all PEV chargers have been scheduled.

PEV nodes whose charging results in out of tolerance conditions (e.g., violating voltage and/or generation limits) will be rescheduled until the constraints are satisfied. Therefore, not all PEV owners may be able to charge in their preferred charging zones and some might be deferred to the next time intervals. Further details and explanation of the proposed real-time PEV coordination algorithm are omitted for the sake of brevity and can be found in related published articles [119, 147, 149].

7.4.6 Coordinated PEV charging results

The results presented in Figs. 7.12-7.23 and Tables 7.3-7.4 show the simulated impacts of various coordinated charging scenarios for multiple PEVs in the 1200 node test system. Daily system load curves are computed with voltage profiles and individual transformer loads supplying each low voltage residential system. The priority grouping of PEVs can be seen in the coloured system load curves indicating that the algorithm is scheduling PEVs to be prioritised within their designated time zones. Most notably, this has the effect of significantly curtailing the system peak demand which is more favourable from a standpoint of generation dispatch and preventing overloads (e.g., Fig. 7.18 for 46% PEV penetration). This also has the effect on limiting the main substation transformer load and improving the system efficiency by reducing I2R losses in cables and transformer impedances. The PEV coordination algorithm is also maintaining all node voltages within specified regulatory limits, even under high PEV penetration levels (Table 7.4).

The 22 individual distribution transformers that supply the low voltage networks show some variability in their daily load cycles depending on PEV penetration level. For low to medium PEV penetrations (e.g., 17-46%, Figs. 7.12-7.20), this

coordination approach effectively diversifies the PEV charging load such that network congestion is largely avoided and the load surges on distribution transformers is relatively low (Table 7.3). This is an important consideration as distribution transformers will be the weakest link in residential networks and newly developing smart grids populated with PEVs. For many of the uncoordinated random charging scenarios (Section 7.3), distribution transformers experienced significant increases (e.g., over 200%) in peak loading which can affect reliability and expected service life. With the coordination smart charging algorithm, transformer currents are significantly reduced by at least 40% when compared to the worst case uncoordinated PEV charging. However, for very large PEV penetrations (e.g., 63%, Figs. 7.21-7.23), which could represent long-term future PEV loading patterns, the coordination approach begins to show its limitations as the rms current in several distribution transformers surges significantly. Nevertheless, these findings demonstrate the possibility of deferring and reducing the frequency of costly upgrades in distribution transformers if PEV charger coordination measures are employed.

The potential for this type of load control in optimising distribution transformer performance is likely to become increasingly important as smart grid technologies gain acceptance. Coordination strategies could be extended to other large domestic loads such as regulating air-conditioner compressors, dishwashers, washing machines and clothes dryers. Furthermore, there are many other factors that could be considered in the development of future coordination strategies that affect transformer performance. For instance, power quality criteria such as THD, harmonic power losses and imbalances generated by single-phase nonlinear smart appliance loads could be considered in the coordination problem to better manage transformer health and improve service life.

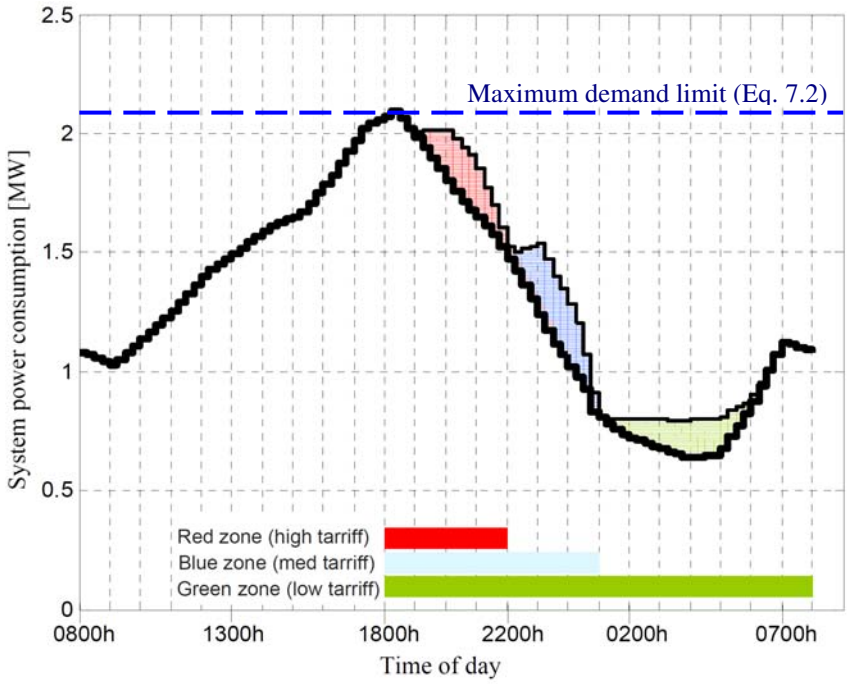

Fig. 7.12. System load curve for coordinated charging considering PEV owner priorities with 17% PEV penetration. Solid black line is the system load with no PEVs. Stacked colour lines are PEV load lines for designated priorities.

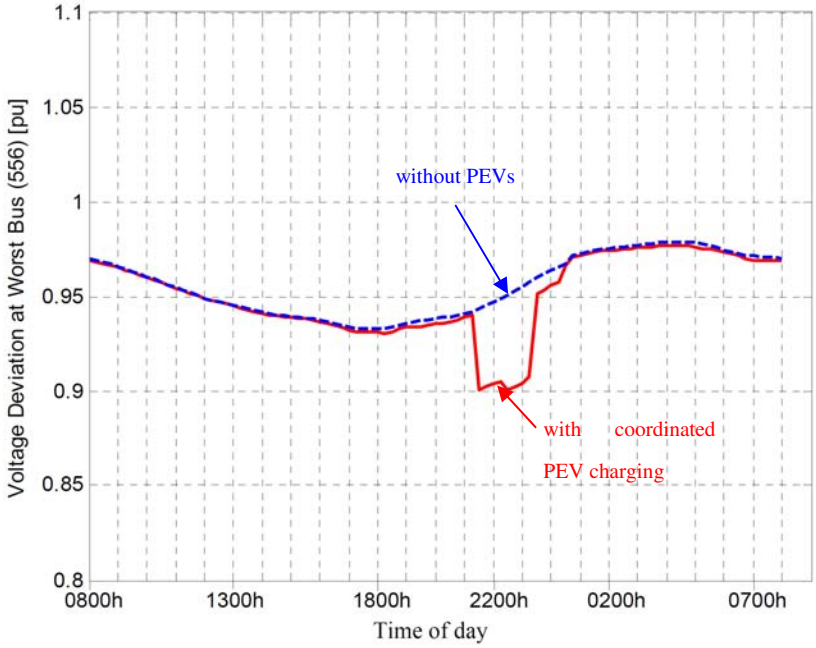

Fig. 7.13. Voltage profile at worst node (10-R48) with coordinated charging (17% PEV penetration).

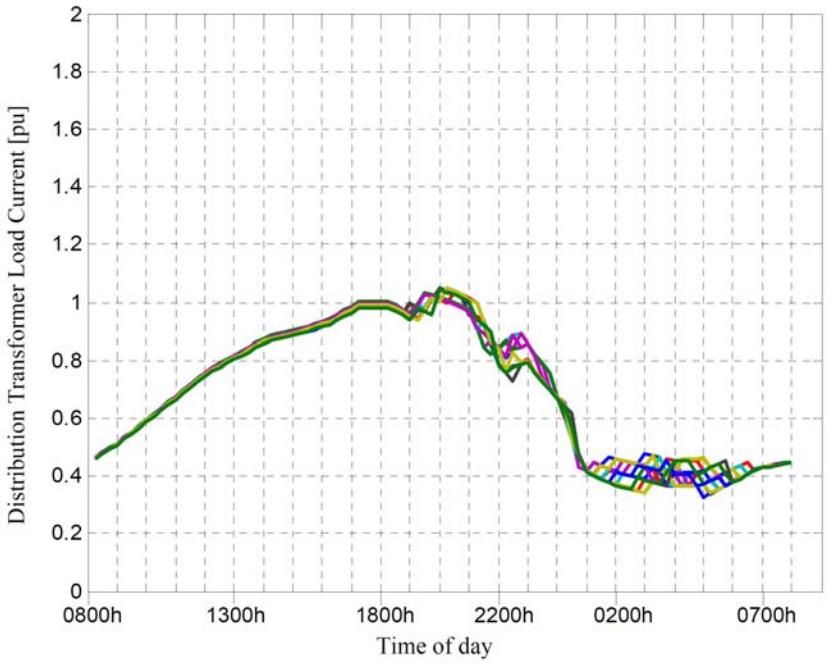

Fig. 7.14. Load currents for all 22 distribution transformers with coordinated charging (17 % PEV penetration).

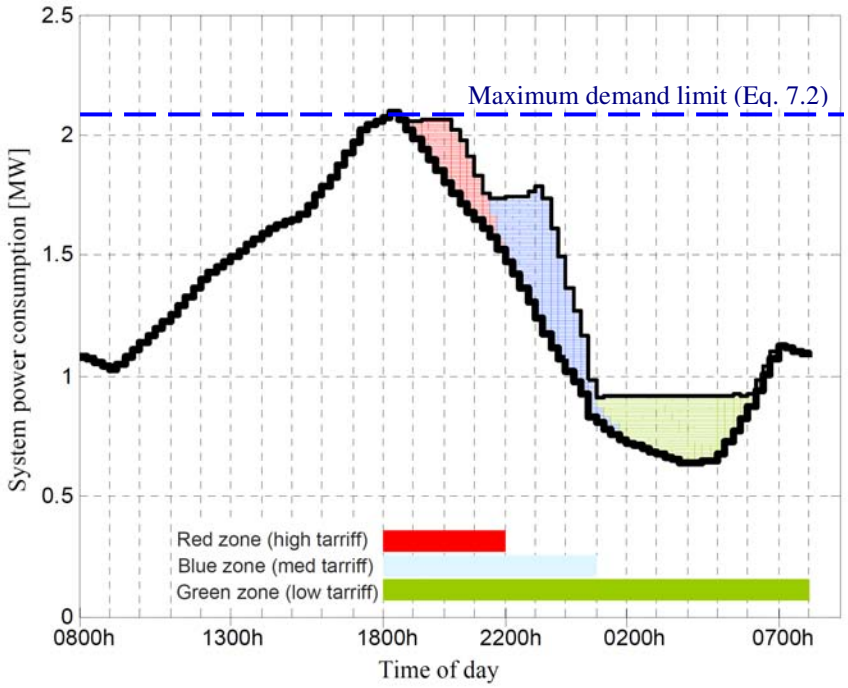

Fig. 7.15. System load curve for coordinated charging considering PEV owner priorities with 31% PEV penetration. Solid black line is the system load with no PEVs. Stacked colour lines are PEV load lines for designated priorities.

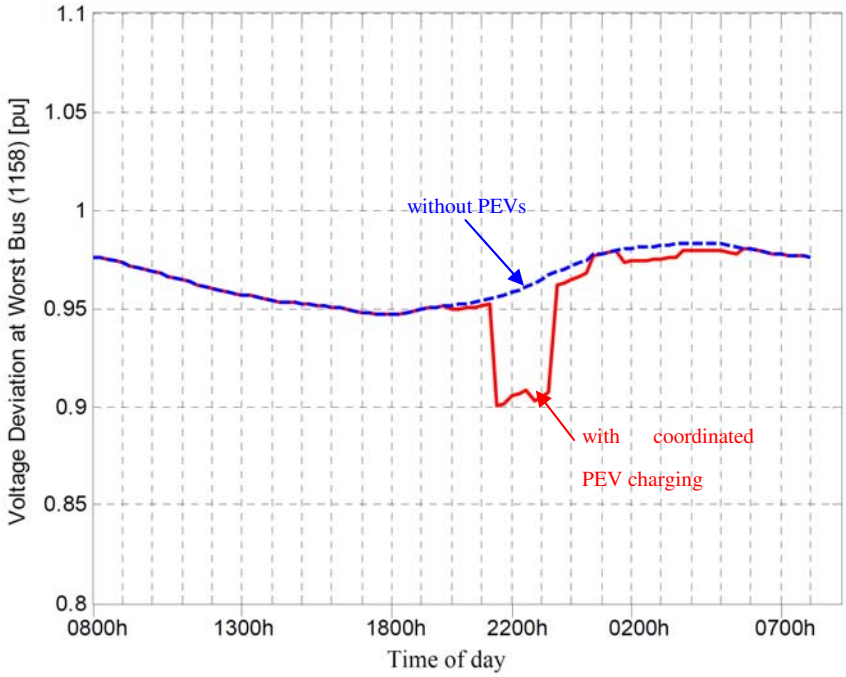

Fig.7.16. Voltage profile at worst node (31-R14) with coordinated charging node (31% PEV penetration).

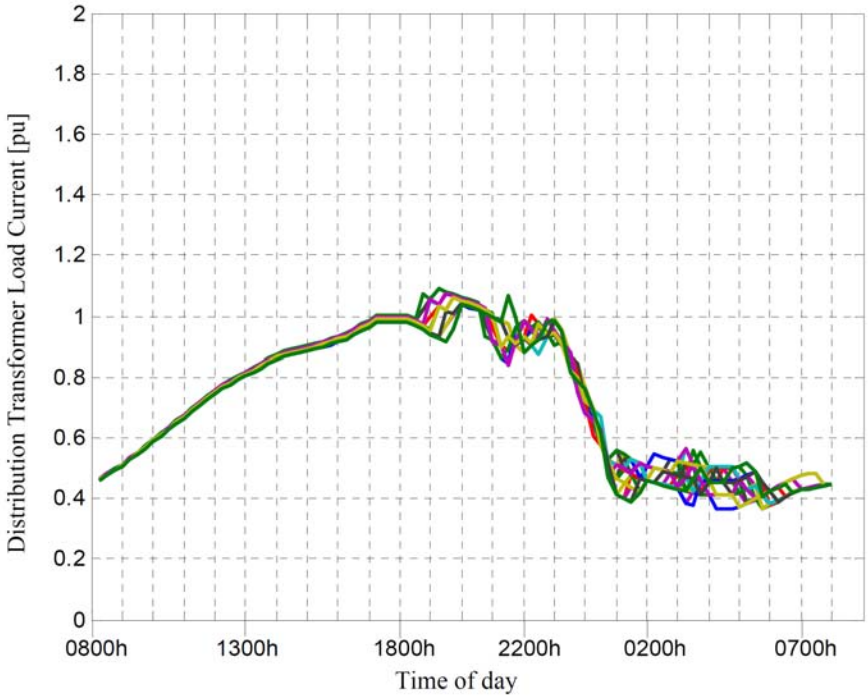

Fig. 7.17. Load currents for all 22 distribution transformers with coordinated charging (31 % PEV penetration).

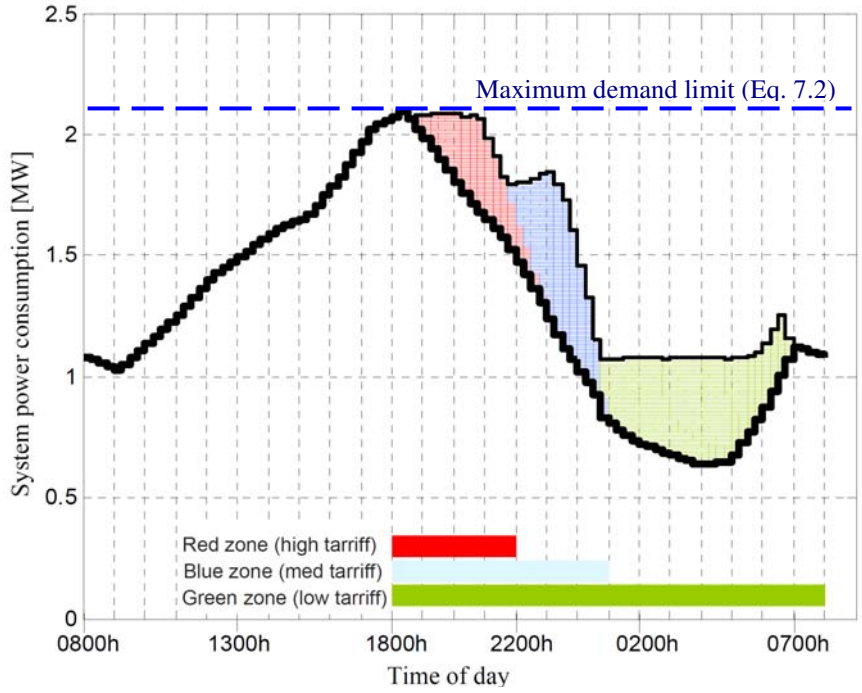

Fig. 7.18. System load curve for coordinated charging considering PEV owner priorities with 46% PEV penetration. Solid black line is the system load with no PEVs. Stacked colour lines are PEV load lines for designated priorities.

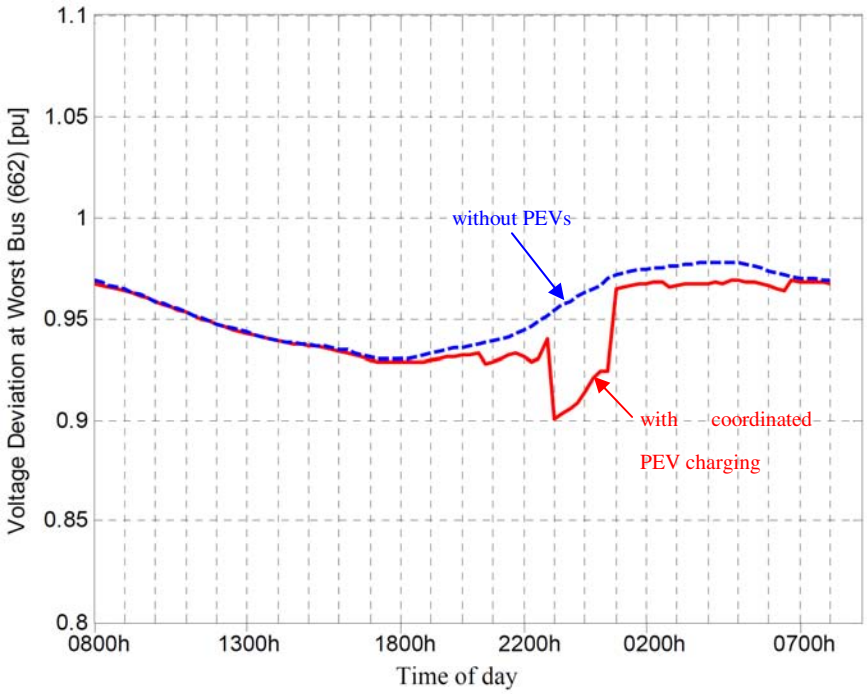

Fig. 7.19. Voltage profile at worst node (12-R48) with coordinated charging (46% PEV penetration).

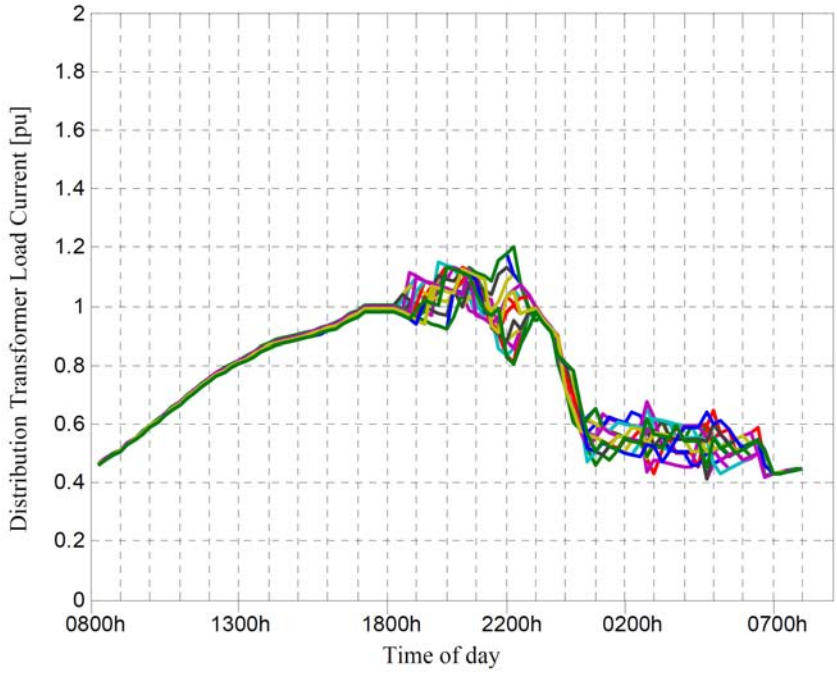

Fig. 7.20. Load currents for all 22 distribution transformers with coordinated charging (46 % PEV penetration).

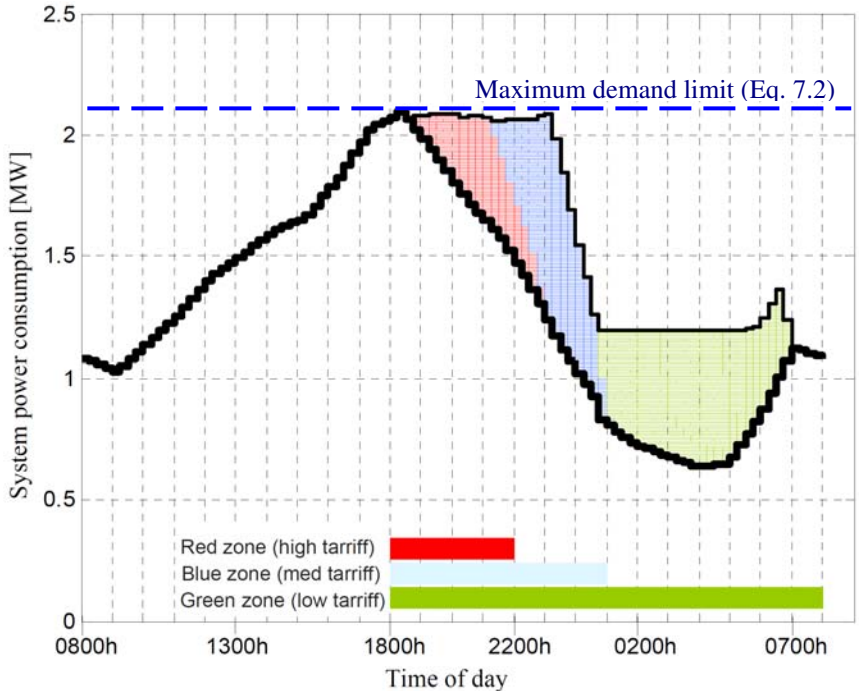

Fig. 7.21. System load curve for coordinated charging considering PEV owner priorities with 62% PEV penetration. Solid black line is the system load with no PEVs. Stacked colour lines are PEV load lines for designated priorities.

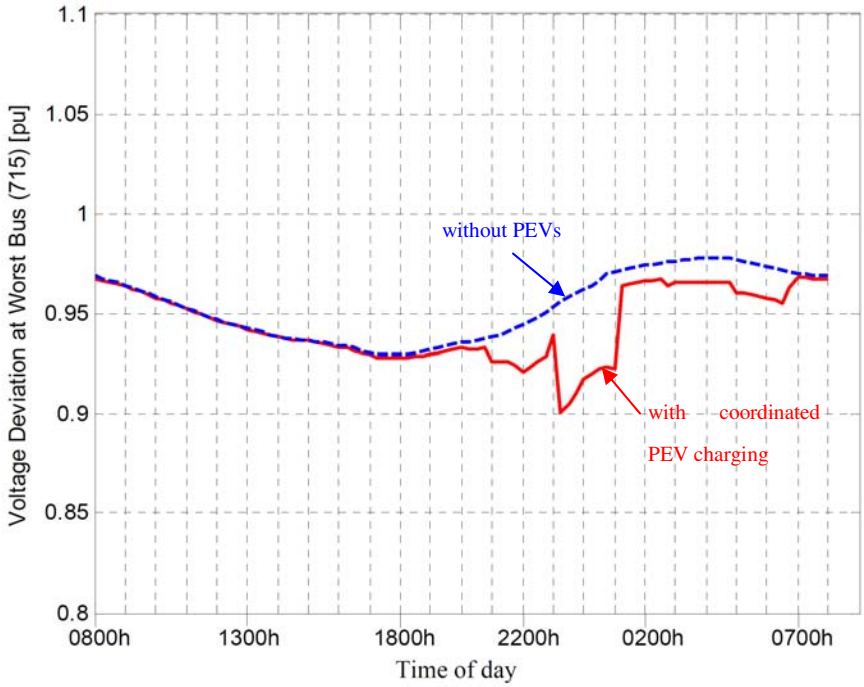

Fig. 7.22. Voltage profile at worst node (13-R48) with coordinated charging (62% PEV penetration).

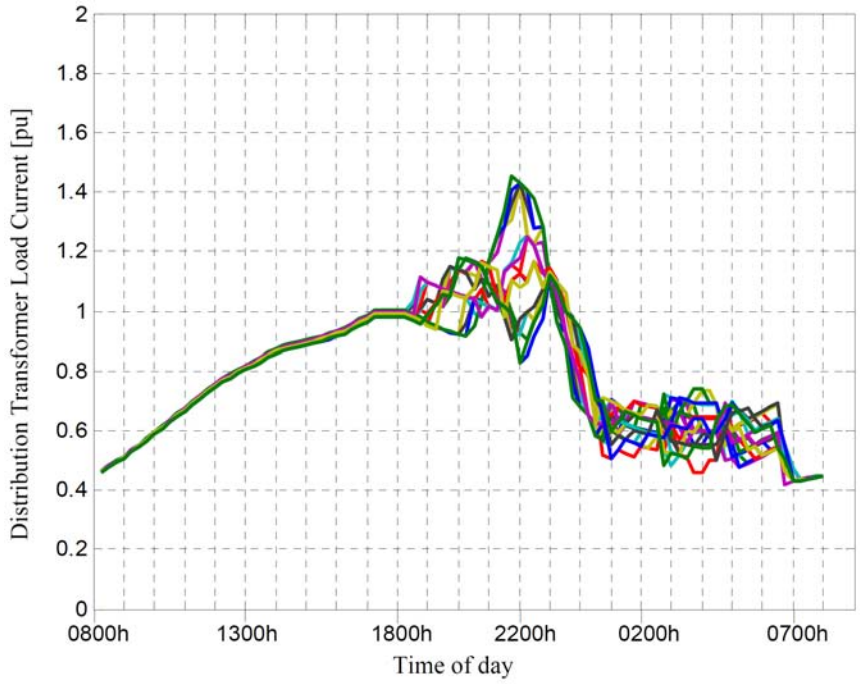

Fig. 7.23. Load currents for all 22 distribution transformers with coordinated charging (63% PEV penetration).

Table 7.3
Transformer load currents with coordinated charging for different PEV penetrations.

PEV (%)	I_{max} (pu)*	I_{min} (pu)*	I_{avg} (pu)*
0	1.000 (DT-15 @ 18:15hrs)	0.3192 (DT-29 @ 04:00hrs)	0.6560
17	1.0492 (DT-28 @ 20:00hrs)	0.3269 (DT-19 @ 05:00hrs)	0.6907
31	1.0902 (DT-15 @ 19:15hrs)	0.3657 (DT-19 @ 04:15hrs)	0.7180
46	1.2035 (DT-15 @ 22:15hrs)	0.4119 (DT-11 @ 04:45hrs)	0.7487
62	1.4560 (DT-15 @ 21:45hrs)	0.4208 (DT-18 @ 06:45hrs)	0.7803

*) Load currents given in per-unit of peak transformer loading with no PEVs

Table 7.4
Voltage performance with coordinated charging for different PEV penetrations.

PEV (%)	V_{worst} (pu)	V_{avg} (pu)	Worst Node	Worst Time*
0	0.9225	0.9729	15-R33	18:15hrs
17	0.90025	0.97132	10-R48	21:30hrs
31	0.90013	0.97035	31-R14	21:30hrs
46	0.90022	0.96957	12-R48	23:00hrs
62	0.90025	0.96853	13-R48	23:15hrs

*) Time at which worst voltage occurs (to the nearest 15 minute)

7.5 CONCLUSION

Future transformer loading issues concerning PEV charger activity within smart grids is explored. Specifically, the impacts of uncoordinated and coordinated PEV charging on low voltage distribution systems were simulated and compared. A recently developed PEV charging coordination strategy was implemented to study the benefits of smart charging on reducing stress on distribution transformers with different levels of PEV penetration. The coordination algorithm includes PEV owner

designated charging priorities, system demand constraints, voltage regulation and loss minimisation functions. The following main conclusions are drawn from this study:

- There is a high probability that uncoordinated PEV charging activity will coincide with much of the on-peak demand period since PEV owners are expected to charge their vehicles in the evening on arrival from work. This is shown to cause significant transformer load surging issues even under low PEV penetrations.
- Simulated uncoordinated PEV charging results indicate that the load on local distribution transformers for PEV penetrations from 17% to 31% result in a significant rise transformer currents (e.g., from 37% to 74% increases). This is indicative of the near future PEV loading patterns expected in some countries as PEVs become more popular over conventional fuel based vehicles.
- Even low PEV penetrations under the most diversified loading conditions (e.g., charging distributed over 1800-0800 hrs with overnight charging) can still result in significant voltage deviations exceeding tight regulatory limits often imposed in low voltage systems.
- If smart coordinated charging capabilities are not ready in the near future, utilities may be faced with the prospect of costly and more frequent distribution transformer upgrades until smart grid and coordinated charging facilities become available.
- Simulation results demonstrate the significant benefits of coordinated smart PEV charging for diversifying the PEV charging activities such that severe substation and distribution transformer load surges are minimised. A significant reduction in the rms current loading was observed versus uncoordinated random charging which results in less losses and thermal stress on transformers thereby improving component reliability.
- The implemented coordinated PEV charging approach resulted in all system node voltages successfully maintained within specified regulatory limits, even under

high PEV penetrations.

- However, under very high PEV penetrations, e.g., 63% and large systems, coordinated charging approach may not fully mitigate from severe increases in transformer loading as shown. However, it can nevertheless defer and reduce the frequency of costly distribution transformer upgrades.

Chapter 8. Conclusions

A range of transformer operational issues and abnormalities covering several types of transient and steady-state electromagnetic disturbances have been explored in this thesis. Particularly, new dynamic disturbance effects related to three-phase transformer operation have been brought to light especially in the areas of inrush, geomagnetically induced currents, harmonic distortion, ferroresonance, and transformer aging. Through the course of these studies, new and improved modelling tools have been proposed for accurate electromagnetic transient models of three-phase multi-leg transformer cores. Finally, this thesis extends transformer research into the domain of newly emerging smart grids by examining transformer performance under coordinated and uncoordinated PEV charging activity in distribution grids.

At the outset of this research, the first stage was to identify short comings of existing three-phase transformer modelling studies as summarised in Chapter 2. Through an extensive literature review, it became apparent that three-phase transformer models had not progressed as far as single-phase transformer models. There was an overwhelming tendency in existing transient studies to oversimplify three-phase transformer models. The majority of investigations were based on models that (1) ignored magnetic effects of multiple fluxes interacting in different multi-leg core geometries, (2) made the assumption of per-phase single-phase transformer models approximating three-phase transformer behaviour and (3) oversimplified ferromagnetic nonlinearities to the degree of ignoring complicated effects such as dynamic magnetic hysteresis (major and minor loop formations). In order to address these shortcomings, Chapter 2 outlined the development of a new three-phase transformer model considering detailed effects of magnetic core hysteresis, core-leg topology including core structure asymmetry with cross-coupling effects of multiple

magnetic core flux paths.

In Chapter 3, the importance of considering dynamic hysteresis effects into electromagnetic transient and steady-state simulations of three-phase transformers was shown for no-load and inrush current predictions. Firstly, a comparison was made between using traditional magnetic core models using single-valued nonlinear functions versus the proposed model that includes hysteresis nonlinearities. When compared with experimental data for steady-state no-load currents, the proposed hysteresis model was shown to agree satisfactorily by being able to reproduce measured hysteresis loops and current waveforms. Following this, the proposed model was tested under dynamic electromagnetic conditions by comparing simulated waveforms of inrush currents to measurements obtained from a laboratory three-leg transformer core. Good agreement was observed under inrush conditions and the results indicated that failure to include magnetic hysteresis effects may lead to inaccurate peak current estimations and inrush dampening times. These results constituted the first successful validation of the proposed transformer model for steady-state and transient electromagnetic disturbances.

Chapter 4 extends the study into a more unpredictable and dynamic electromagnetic disturbance known as ferroresonance. Extensive simulation and experimental studies were carried out for a three-phase transformer undergoing ferroresonance initiated by unbalanced switching with capacitors. The influence of traditional ferromagnetic core modelling assumptions in the creation of false ferroresonance modes as well as the omission of more severe chaotic modes were highlighted when hysteresis effects and magnetic flux couplings are ignored. This work demonstrated for the first time that ferroresonance oscillations can exhibit different behaviour in each phase as was shown experimentally which the model was able to reproduce. For instance, it was observed that chaotic voltage waveforms were observed in the open-circuited phase while subharmonic or quasi-periodic modes appeared in the other phases. Hence, as was typically done in the past, extending per-phase modelling approaches and analysis techniques to the study of three-phase transformer ferroresonance behaviour can lead to incorrect predictions.

Chapter 5 takes the study to one of the largest scale electromagnetic disturbances that impact power networks across the world. Geomagnetically induced currents (GICs) effects on three-phase transformers were investigated with the aid of the developed transformer model together with an experimental test setup designed to mimic GIC events. Noteworthy of this study compared to previous work is the explanation for the significance of power system symmetry in suppressing harmonic distortion in a dc biased three-leg transformer. Until now, the explanation and theoretical proof for this phenomenon had yet to be given. It is shown through theoretical studies, simulation and experimental results why unbalanced GICs in each phase amplify the dc components in the fluxes causing half-cycle saturation and highly distorted currents in three-phase three-leg transformers. However, on the hand, when the dc biases in the currents and mmfs in each phase are balanced, then the transformer is shown to exhibit much less sensitivity to dc bias from GICs because the dc components in the core fluxes are suppressed.

The issue of transformer aging in distorted and unbalanced power networks is studied in Chapter 6. There is very limited work currently done on estimating transformer aging in the presence of harmonic distortions and system imbalances. This chapter details a new enhanced method of transformer aging estimation based on the proposed nonlinear transformer model and Arrhenius thermal aging reaction equations. The approach significantly expands on previous methods which were only applicable to sinusoidal and balanced transformer operation. Through extensive case studies, it is shown that the proposed technique can estimate the loss of life effect based on additional fundamental and harmonic losses computed by the proposed model. Moreover, it is shown that unbalanced nonlinear loads such as single-phase rectification can cause significant additional power losses and temperature rises contributing to loss of life.

The final part of this thesis looks at future transformer operational issues in smart grids with multiple PEV battery charging. This chapter firstly focuses on random uncoordinated PEV battery charging in residential networks that might be expected from PEVs randomly plugging in at different times of the day. The transformer

loading side effects from uncoordinated PEV charging are simulated and discussed based on a modified load flow algorithm. The study highlights significant network congestion issues where the distribution transformer could become the bottleneck for significant overloads, even with low PEV penetrations. The potential benefits of coordinated smart charging in averting transformer overloads is also investigated using a recently proposed PEV charger coordination strategy. The study results indicate the potential for significant benefits of coordinated smart charging in alleviating transformer stresses and maximising transformer life. In general, it is concluded that in the wake of smart grid deployment, there is significant potential for harnessing smart grid technology to better manage transformer health and service life.

8.1 RESEARCH CONTRIBUTIONS

The main results of this doctoral thesis have been documented and published in 8 journal articles and over 20 conference papers as listed in Section 1.5. The primary research contributions are summarised as follows.

1. A new and accurate dynamic model of a three-phase transformer is proposed which unlike previous models considers the detailed magnetic effects of multiple flux paths interacting in asymmetric multi-leg core. Furthermore, the model goes into higher detail for modelling ferromagnetic core nonlinearities by considering the multiple hysteresis loop trajectories (major and minor loops) that can be generated under distorted nonsinusoidal steady-state and transient conditions.
2. The transient response of three-phase transformers under inrush conditions are studied through comprehensive simulation and experimental tests cases. For the first time, the importance of magnetic hysteresis nonlinearities with their major and minor loop trajectories as well as core asymmetry is shown to significantly influence no-load magnetisation and inrush current predictions.
3. A new investigation into the largely unexplored three-phase transformer

ferroresonance phenomenon was carried out with the newly proposed nonlinear model. For the first time, new ferroresonance behaviour was identified with more accurate mode prediction shown for asymmetric three-phase transformer cores with the proposed model. It was concluded that the common practice of oversimplifying transformer models with single-valued non-hysteretic core models and ignoring magnetic flux couplings in multi-leg cores results in false ferroresonance modes or the omission of more dangerous chaotic modes. The newly proposed transformer model considering hysteresis nonlinearities and core topology was able to duplicate measurements of ferroresonance oscillations with good accuracy.

4. Based on improved transformer modelling techniques, new operating conditions of three-leg transformers in the presence of geomagnetically induced currents (GICs) were uncovered. It was shown how three-leg transformer cores were more prone to current harmonic distortions and half-cycle saturation from unbalanced GICs in each phase. On the other hand, if the GIC dc biases in each phase are exactly balanced, the transformer is much less sensitive to the damaging effects of GICs since the dc components in fluxes causing saturation are minimised. This was demonstrated through theoretical and simulation studies which were successfully confirmed by measurements of a dc biased three-leg transformer core.

5. A novel method of estimating transformer aging in three-phase transformers operating in distorted and unbalanced power networks was proposed. For the first time, the aging effects considering voltage-current harmonic interactions, three-phase transformer core nonlinearities and unbalanced nonlinear loads are included in the aging estimation. Results indicated that transformer operation under unbalanced nonlinear loads resulted in significant transformer aging where previous aging methods were not applicable.

6. This thesis carries out new transformer studies of smart grids and plug-in electric vehicle operation impacting transformer operation. The study concluded that

uncoordinated PEV charging may result in detrimental transformer performance degradation issues that could impact reliability and service life. A possible alternative to alleviate transformer stress was investigated through coordinated smart charging of multiple PEV chargers to better manage transformer health.

8.2 FUTURE WORK

The following research avenues are suggested for future study in continuation of this work.

1. Several of the studied electromagnetic disturbances that impact transformers such as inrush, harmonic distortion and unbalanced operation are also known to affect rotating machines. This should be further investigated with improved transient electromagnetic models. The proposed transformer model has scope to be expanded for the study of other electromagnetic devices such as induction machines employing similar electric equivalent circuit models.
2. This thesis covers several transformer electromagnetic disturbances with an improved nonlinear model. In continuation of this work, other disturbances could be investigated with the proposed model such as the effects of voltage sags and swells.
3. With the deployment of smart grids, transformers will undoubtedly become the focal point and weakest links in terms of the reliability of distribution systems. Thus, more research is warranted in assessing the future demands and constraints of distribution transformers operating with different smart grid functions. Examples of this are the integration and coordination of renewable energy sources (e.g., rooftop solar photovoltaics) and distributed generation into smart grids which, together with PEVs, could further affect distribution transformer performance.
4. As shown in this study, future smart grid functions such as demand response load control of smart appliances and PEV battery charging may impact distribution

transformer performance. Development of coordination approaches for scheduling loads to improve transformer performance (e.g., reducing fundamental plus harmonic losses, THD and temperature rises) is a worthwhile research topic.

5. Transformer research into smart grids could further be extended by considering the effects of ancillary services of PEVs that are currently being proposed such as energy storage, vehicle-to-grid (V2G) discharging and frequency regulation support. This may considerably impact distribution transformer loading patterns and should be investigated to determine how power quality, transformer service life and economic running performance may be affected.

References

[1] "The evolution of power transformers: 110 years of power transformer technology ", 2011. [Online]. Available: http://www.abbaustralia.com.au/cawp/db0003db002698/1d5674d769397bc8c12572f40045bd75.aspx.

[2] E. I. Amoiralis, M. A. Tsili, and A. G. Kladas, "Transformer design and optimization: a literature survey," *IEEE Transactions on Power Delivery,* vol. 24, no. 4, pp. 1999-2024, 2009.

[3] "IEEE Recommended Practice for Monitoring Electric Power Quality," *IEEE Std 1159-2009 (Revision of IEEE Std 1159-1995),* pp. c1-81, 2009.

[4] C. K. Duffey and R. P. Stratford, "Update of harmonic standard IEEE-519: IEEE recommended practices and requirements for harmonic control in electric power systems," *IEEE Transactions on Industry Applications,* vol. 25, no. 6, pp. 1025-1034, 1989.

[5] M. R. Iravani, A. K. S. Chaudhary, W. J. Giesbrecht, I. E. Hassan, A. J. F. Keri, K. C. Lee, J. A. Martinez, A. S. Morched, B. A. Mork, M. Parniani, A. Sharshar, D. Shirmohammadi, R. A. Walling, and D. A. Woodford, "Modeling and analysis guidelines for slow transients-Part III. The study of ferroresonance," *IEEE Transactions on Power Delivery,* vol. 15, no. 1, pp. 255-265, 2000.

[6] E. F. Fuchs and Y. Yiming, "Measurement of λ-i characteristics of asymmetric three-phase transformers and their applications," *IEEE Transactions on Power Delivery,* vol. 17, no. 4, pp. 983-990, 2002.

[7] A. Masoum, P. S. Moses, and A. S. Masoum, "Electromagnetic transient behavior of three-phase three-leg asymmetric power transformers subject to voltage sags considering magnetic flux couplings and hysteresis effects," *IET Electric Power Applications,* (submitted).

[8] M. A. S. Masoum, E. F. Fuchs, and D. J. Roesler, "Large signal nonlinear model of anisotropic transformers for nonsinusoidal operation-Part II.

Magnetizing and core-loss currents," *IEEE Transactions on Power Delivery,* vol. 6, no. 4, pp. 1509-1516, 1991.

[9] H. Lamba, M. Grinfeld, S. McKee, and R. Simpson, "Subharmonic ferroresonance in an LCR circuit with hysteresis," *IEEE Transactions on Magnetics,* vol. 33, no. 4, pp. 2495-2500, 1997.

[10] A. Rezaei-Zare, R. Iravani, and M. Sanaye-Pasand, "Impacts of transformer core hysteresis formation on stability domain of ferroresonance modes," *IEEE Transactions on Power Delivery,* vol. 24, no. 1, pp. 177-186, 2009.

[11] A. D. Theocharis, J. Milias-Argitis, and T. Zacharias, "Three-phase transformer model including magnetic hysteresis and eddy currents effects," *IEEE Transactions on Power Delivery,* vol. 24, no. 3, pp. 1284-1294, 2009.

[12] J. V. Leite, A. Benabou, N. Sadowski, and M. V. F. da Luz, "Finite element three-phase transformer modeling taking into account a vector hysteresis model," *IEEE Transactions on Magnetics,* vol. 45, no. 3, pp. 1716-1719, 2009.

[13] P. S. Moses and M. A. S. Masoum, "Modeling subharmonic and chaotic ferroresonance with transformer core model including magnetic hysteresis effects," *WSEAS Transaction on Power Systems,* vol. 4, no. 12, pp. 361-371, 2009.

[14] P. S. Moses and M. A. S. Masoum, "A transformer core model including magnetic hysteresis effects for ferroresonance studies," in *Proc. WSEAS* Genova, Italy: 9th WSEAS International Conf. on Electric Power Systems, High Voltages, Electric Machines, 2009.

[15] A. Rezaei-Zare, R. Iravani, M. Sanaye-Pasand, H. Mohseni, and S. Farhangi, "An Accurate Hysteresis Model for Ferroresonance Analysis of a Transformer," *IEEE Transactions on Power Delivery,* vol. 23, no. 3, pp. 1448-1456, 2008.

[16] L. Chua and K. Stromsmoe, "Lumped-circuit models for nonlinear inductors exhibiting hysteresis loops," *IEEE Transactions on Circuit Theory,* vol. 17, no. 4, pp. 564-574, 1970.

[17] F. De Leon and A. Semlyen, "A simple representation of dynamic hysteresis losses in power transformers," *IEEE Transactions on Power Delivery,* vol. 10, no. 1, pp. 315-321, 1995.

[18] D. Jiles and D. Atherton, "Ferromagnetic hysteresis," *IEEE Transactions on Magnetics,* vol. 19, no. 5, pp. 2183-2185, 1983.

[19] I. D. Mayergoyz, *Mathematical models of hysteresis and their applications*, 1st ed. Amsterdam ; Boston: Elsevier, 2003.

[20] F. Preisach, "Über die magnetische Nachwirkung," *Zeitschrift für Physik,* vol. B 94, pp. 277-302, 1935.

[21] J. Tellinen, "A simple scalar model for magnetic hysteresis," *IEEE Transactions on Magnetics,* vol. 34, no. 4, pp. 2200-2206, 1998.

[22] M. Tumay and R. R. S. Simpson, "Method of predicting three-phase transformer transients including magnetic nonlinearity and hysteresis effects," in *Proc. 7th Mediterranean Electrotechnical Conference*, 1994, pp. 841-844 vol.2.

[23] X. S. Chen and P. Neudorfer, "Digital model for transient studies of a three-phase five-legged transformer," in *Proc. IEE Generation, Transmission and Distribution*. vol. 139, 1992, pp. 351-358.

[24] J. M. Prousalidis, N. D. Hatziargyriou, and B. C. Papadias, "Representation of hysteresis in three-phase transformer models for electromagnetic transients," in *Proc. IEE Electric Power Applications*, 1996, pp. 331-338.

[25] D. Dolinar, J. Pihler, and B. Grcar, "Dynamic model of a three-phase power transformer," *IEEE Transactions on Power Delivery,* vol. 8, no. 4, pp. 1811-1819, 1993.

[26] P. S. Moses, M. A. S. Masoum, and H. A. Toliyat, "Dynamic modeling of three-phase asymmetric power transformers with magnetic hysteresis: no-load and inrush conditions," *IEEE Transactions on Energy Conversion,* vol. 25, no. 4, pp. 1040-1047, 2010.

[27] "PSpice A/D Reference Guide," San Jose, CA, USA: Cadence Design Systems, 2003.

[28] J. Pedra, L. Sainz, F. Corcoles, R. Lopez, and M. Salichs, "PSPICE computer model of a nonlinear three-phase three-legged transformer," *IEEE Transactions on Power Delivery,* vol. 19, no. 1, pp. 200-207, 2004.

[29] G. Chang, C. Hatziadoniu, W. Xu, P. Ribeiro, R. Burch, W. M. Grady, M. Halpin, Y. Liu, S. Ranade, D. Ruthman, N. Watson, T. Ortmeyer, J. Wikston, A. Medina, A. Testa, R. Gardinier, V. Dinavahi, F. Acram, and P. Lehn, "Modeling devices with nonlinear voltage-current characteristics for harmonic studies," *IEEE Transactions on Power Delivery,* vol. 19, no. 4, pp. 1802-1811, 2004.

[30] J. A. Martinez and B. A. Mork, "Transformer modeling for low- and mid-frequency transients - a review," *IEEE Transactions on Power Delivery,* vol. 20, no. 2, pp. 1625-1632, 2005.

[31] E. C. Cherry, "The duality between interlinked electric and magnetic circuits and the formation of transformer equivalent circuits," *Proc. Phys. Soc.,* vol. 62, 1949.

[32] M. A. S. Masoum and P. S. Moses, "Impact of balanced and unbalanced direct current bias on harmonic distortion generated by asymmetric three-phase three-leg transformers," *IET Electric Power Applications,* vol. 4, no. 7, pp. 507-515, 2010.

[33] M. A. S. Masoum, P. S. Moses, and A. S. Masoum, "Derating of asymmetric three-phase transformers serving unbalanced nonlinear loads," *IEEE Transactions on Power Delivery,* vol. 23, no. 4, pp. 2033-2041, 2008.

[34] M. A. S. Masoum, P. S. Moses, and A. S. Masoum, "Impact of adjustable speed PWM drives on operation and harmonic losses of nonlinear three phase transformers," in *Proc. 7th International Conference on Power Electronics and Drive Systems (PEDS)*, 2007, pp. 562-567.

[35] E. F. Fuchs, Y. You, and D. J. Roesler, "Modeling and simulation, and their validation of three-phase transformers with three legs under DC bias," *IEEE Transactions on Power Delivery,* vol. 14, no. 2, pp. 443-449, 1999.

[36] G. Bertotti, *Hysteresis in magnetism: for physicists, materials scientists, and engineers*: Gulf Professional Publishing, 1998.

[37] E. F. Fuchs and M. A. S. Masoum, *Power quality in power systems and electrical machines*: Academic Press/Elsevier, 2008.

[38] P. S. Moses and M. A. S. Masoum, "Modeling ferroresonance in asymmetric three-phase power transformers," in *Proc. Australasian Universities Power Engineering Conference (AUPEC)*, 2009, pp. 1-6.

[39] P. S. Moses, M. A. S. Masoum, and H. A. Toliyat, "Impacts of hysteresis and magnetic couplings on the stability domain of ferroresonance in asymmetric three-phase three-leg transformers," *IEEE Transactions on Energy Conversion,* vol. 26, no. 2, pp. 581-592, 2011.

[40] P. Ferracci, "Ferroresonance," *Group Schneider: Cahier No. 190,* pp. 1-28, March 1998.

[41] R. C. Dugan, "Examples of ferroresonance in distribution," in *Proc. IEEE Power Engineering Society General Meeting*. vol. 2, 2003, pp. 1213-1215.

[42] D. A. N. Jacobson, "Examples of ferroresonance in a high voltage power system," in *Proc. IEEE Power Engineering Society General Meeting*. vol. 2, 2003, pp. 1206-1212.

[43] K. Laohacharoensombat, K. Tuitemwong, S. Jaruwattanadilok, C. Wattanasakpubal, and K. Kleebmek, "Case study of ferroresonance in 33 kV distribution network of PEA Thailand," in *Proc. IEEE Region 10 Conference (TENCON)*. vol. C, 2004, pp. 417-420 Vol. 3.

[44] P. E. Sutherland and R. Manning, "Ferroresonance in a 13.8 kV Distribution Line," in *Proc. 41st IAS Annual Meeting IEEE Industry Applications Conference*, 2006, pp. 2238-2241.

[45] T. Tsao and C. Ning, "Analysis of ferroresonant overvoltages at Maanshan Nuclear Power Station in Taiwan," *IEEE Transactions on Power Delivery,* vol. 21, no. 2, pp. 1006-1012, 2006.

[46] V. Simha and W. Lee, "The jump phenomena," *IEEE Industry Applications Magazine,* vol. 14, no. 5, pp. 53-59, 2008.

[47] A. Clerici and C. H. Didriksen, "Dynamic overvoltages and ferroresonance found in switching surge studies for Iran 400 kV system," *IEEE Transactions on Power Apparatus and Systems,* vol. PAS-91, no. 1, pp. 195-203, 1972.

[48] D. R. Crane and G. W. Walsh, "Large mill power outages caused by potential transformer ferroresonance," *IEEE Transactions on Industry Applications,* vol. 24, no. 4, pp. 635-640, 1988.

[49] J. Bethenod, "Sur le transformateur et résonance," *L`Eclairae Electrique,* pp. 289-296, 1907.

[50] P. Boucherot, "Existence de deux régimes en ferro-résonance," *R. G. E.,* pp. 289-296, 1920.

[51] J. W. Butler and C. Concordia, "Analysis of series capacitor application problems," *AIEE Trans,* vol. 56, pp. 975-988, 1937.

[52] R. H. Hopkinson, "Ferroresonance during single-phase switching of 3-phase distribution transformer banks," *IEEE Transactions on Power Apparatus and Systems,* vol. 84, pp. 289-293, 1965.

[53] L. B. Crann and R. B. Flickinger, "Overvoltages on 14.4/24.9-kV rural distribution systems," *AIEE Trans. on Power Apparatus and Systems,* vol. 73, no. 2, pp. 1208-1212, 1954.

[54] G. G. Auer and A. J. Schultz, "An analysis of 14.4/24.9-kV grounded-wye distribution system overvoltages," *AIEE Trans. on Power Apparatus and Systems,* vol. 73, no. 2, pp. 1027-1032, 1954.

[55] R. Rudenberg, "Transient performance of electric power systems," *New York, NY: McGraw-Hill Book Company,* 1950.

[56] C. Hayashi, "Nonlinear oscillations in physical systems," *New York, NY: McGraw-Hill Book Company,* 1964.

[57] C. Kieny, "Application of the bifurcation theory in studying and understanding the global behavior of a ferroresonant electric power circuit," *IEEE Transactions on Power Delivery,* vol. 6, no. 2, pp. 866-872, 1991.

[58] B. A. Mork and D. L. Stuehm, "Application of nonlinear dynamics and chaos to ferroresonance in distribution systems," *IEEE Transactions on Power Delivery,* vol. 9, no. 2, pp. 1009-1017, 1994.

[59] J. M. T. Thompson and H. B. Stewart, *Nonlinear dynamics and chaos : geometrical methods for engineers and scientists*. Chichester West Sussex: Wiley, 1986.

[60] F. Wornle, D. K. Harrison, and Z. Chengke, "Analysis of a ferroresonant circuit using bifurcation theory and continuation techniques," *IEEE Transactions on Power Delivery,* vol. 20, no. 1, pp. 191-196, 2005.

[61] A. Ben-Tal, V. Kirk, and G. Wake, "Banded chaos in power systems," *Power Delivery, IEEE Transactions on,* vol. 16, no. 1, pp. 105-110, 2001.

[62] A. Ben-Tal, D. Shein, and S. Zissu, "Studying ferroresonance in actual power systems by bifurcation diagram," *Elsevier - Electric Power Systems Research,* vol. 49, pp. 175-183, 1999.

[63] D. Kaplan and L. Glass, *Understanding nonlinear dynamics*. New York: Springer-Verlag, 1995.

[64] G. Mokryani, M. R. Haghifam, H. Latafat, P. Aliparast, and A. Abdollahy, "Analysis of ferroresonance in a 20kV distribution network," in *Proc. 2nd International Conference on Power Electronics and Intelligent Transportation System (PEITS)*, 2009, pp. 31-35.

[65] B. Tanggawelu, R. N. Mukerjee, and A. E. Ariffin, "Ferroresonance studies in Malaysian utility's distribution network," in *Proc. IEEE Power Engineering Society General Meeting*. vol. 2, 2003, pp. 1216-1219.

[66] V. C. Nikolaidis, I. Milis, and G. Rizopoulos, "Transient phenomena analysis and protection evaluation in an industrial power system," *IEEE Transactions on Power Delivery,* vol. 27, no. 1, pp. 300-308, 2012.

[67] G. Mokryani and M. R. Haghifam, "Application of wavelet transform and MLP neural network for ferroresonance identification," in *Proc. IEEE Power and Energy Society General Meeting*, 2008, pp. 1-6.

[68] B. Zhang and T. Lu, "On the use of wavelet decomposition for ferroresonance detection in power system," in *Proc. Asia-Pacific Power and Energy Engineering Conference (APPEEC)*, 2009, pp. 1-4.

[69] W. Piasecki, M. Florkowski, M. Fulczyk, P. Mahonen, and W. Nowak, "Mitigating ferroresonance in voltage transformers in ungrounded MV networks," *IEEE Transactions on Power Delivery,* vol. 22, no. 4, pp. 2362-2369, 2007.

[70] P. Picher, L. Bolduc, B. Girard, and V. N. Nguyen, "Mitigation of ferroresonance induced by single-phase opening of a three-phase transformer feeder," in *Proc. Canadian Conference on Electrical and Computer Engineering (CCECE)*, 2006, pp. 482-485.

[71] M. Sanaye-Pasand, A. Rezaei-Zare, H. Mohseni, S. Farhangi, and R. Iravani, "Comparison of performance of various ferroresonance suppressing methods in inductive and capacitive voltage transformers," in *Proc. IEEE Power India Conference*, 2006.

[72] Y. Yu and H. Zhou, "Study on simulation of ferroresonance elimination in 10kV power system," in *Proc. IEEE/PES Transmission and Distribution Conference and Exhibition: Asia and Pacific*, 2005, pp. 1-7.

[73] L. Yunge, S. Wei, Q. Rui, and Y. Jilin, "A systematical method for suppressing ferroresonance at neutral-grounded substations," *IEEE Transactions on Power Delivery,* vol. 18, no. 3, pp. 1009-1014, 2003.

[74] H. J. Koch, "Gas-insulated transmission line (GIL)," Discussion: Gas-Insulated Transmission Lines, Proceedings of the IEEE PES General Meeting, Toronto, 2003, pp. 2480-2483.

[75] H. J. Koch, "Gas-insulated transmission line (GIL) of the 2nd generation," AC-DC Power Transmission, 28–30 November 2001, Conference Publication No. 485 copyright IEEE 2001, 2001, pp. 39-43.

[76] H. J. Koch and T. Hillers, "Second-generation gas-insulated line," *Power Engineering Journal,* pp. 111-116, 2002.

[77] D. D. Mairs, D. L. Stuehm, and B. A. Mork, "Overvoltages on five-legged core transformers on rural electric systems," *IEEE Transactions on Industry Applications,* vol. 25, no. 2, pp. 366-370, 1989.

[78] P. G. Khorasani and A. Deihimi, "A new modeling of Matlab transformer for accurate simulation of ferroresonance," in *Proc. International Conference on Power Engineering, Energy and Electrical Drives (POWERENG)*, 2009, pp. 529-534.

[79] A. V. Makarov and V. G. Komin, "The research of ferroresonant phenomena in electric circuits under open-phase operating conditions," in *Proc. IEEE Russia Power Tech*, 2005, pp. 1-7.

[80] K. Okumura, "Nonlinear oscillation of three-phase circuit," *Electrical engineering in Japan,* vol. 96, no. 6, p. 106, 1976.

[81] A. Tokic, V. Madzarevic, and I. Uglesic, "Numerical calculations of three-phase transformer transients," *IEEE Transactions on Power Delivery,* vol. 20, no. 4, pp. 2493-2500, 2005.

[82] B. C. Lesieutre, J. A. Mohamed, and A. M. Stankovic, "Analysis of ferroresonance in three-phase transformers," in *Proc. International Conference on Power System Technology (PowerCon).* vol. 2, 2000, pp. 1013-1018.

[83] G. E. Preece, "Earth currents, and the Aurora Borealis of 4th February. Part 2," *Journal of the Society of Telegraph Engineers,* vol. 1, no. 2, pp. 250-256, 1872.

[84] G. E. Preece, "Earth currents, and the Aurora Borealis of 4th February," *Journal of the Society of Telegraph Engineers,* vol. 1, no. 1, pp. 102-114, 1872.

[85] L. Trichtchenko and D. H. Boteler, "Effects of recent geomagnetic storms on power systems," in *7th International Symposium on Electromagnetic Compatibility and Electromagnetic Ecology*, 2007, pp. 265-268.

[86] V. D. Albertson, B. Bozoki, W. E. Feero, J. G. Kappenman, E. V. Larsen, D. E. Nordell, J. Ponder, F. S. Prabhakara, K. Thompson, and R. Walling., "Geomagnetic disturbance effects on power systems," *IEEE Transactions on Power Delivery,* vol. 8, no. 3, pp. 1206-1216, 1993.

[87] T. Hock-Chuan and G. W. Swift, "A novel method of detecting asymmetrical transformer core saturation due to GIC," *IEEE Transactions on Power Apparatus and Systems,* vol. PAS-103, no. 1, pp. 183-189, 1984.

[88] R. J. Pirjola and D. H. Boteler, "Geomagnetically Induced Currents in European high-voltage power systems," in *Canadian Conference on Electrical and Computer Engineering (CCECE '06)*, 2006, pp. 1263-1266.

[89] R. J. Ringlee and J. R. Stewart, "Geomagnetic disturbances and electric power systems," *IEEE Power Engineering Review,* vol. 9, no. 7, pp. c2-c2, 1989.

[90] M. Lahtinen and J. Elovaara, "GIC occurrences and GIC test for 400 kV system transformer," *IEEE Transactions on Power Delivery,* vol. 17, no. 2, pp. 555-561, 2002.

[91] B. Zhang, R. Zeng, J. He, J. Zhao, X. Li, Q. Wang, and X. Cui, "Numerical analysis of potential distribution between ground electrodes of HVDC system considering the effect of deep earth layers," *IET Generation, Transmission & Distribution,* vol. 2, no. 2, pp. 185-191, 2008.

[92] W. Sheng, M. Chengxiong, L. Jiming, M. Guihua, and L. Yancun, "Influence of HVDC ground electrode current on AC transmission system and development of restraining device," in *3rd International Conference on Electric Utility Deregulation and Restructuring and Power Technologies (DRPT 08)*, 2008, pp. 2151-2156.

[93] Z. Bo, Z. Jie, Z. Rong, and H. Jinliang, "Numerical analysis of DC current distribution in AC power system near HVDC system," *IEEE Transactions on Power Delivery,* vol. 23, no. 2, pp. 960-965, 2008.

[94] N. Ben, Z. Rong, Z. Bo, and H. Jinliang, "Research and design of the neutral series resistor to restrain the HVDC ground current flowing into transformer," in *International Conference on Power System Technology (PowerCon '06)*, 2006, pp. 1-6.

[95] E. F. Fuchs and M. A. S. Masoum, "Suppression of harmonic distortion in power systems due to Geomagnetically Induced Currents (GICs) through enforcing GIC balance in all phases of a system (Invention Disclosure)," U. o. Colorado, Ed., 1992.

[96] Y. You, E. F. Fuchs, and P. R. Barnes, "Reactive power demand of transformers with DC bias," in *Proc. Conference Record of the 1994 IEEE Industry Applications Society Annual Meeting*, 1994, pp. 339-346 vol.1.

[97] Y. You, E. F. Fuchs, D. Lin, and P. R. Barnes, "Reactive power demand of transformers with DC bias," *IEEE Industry Applications Society Magazine,* vol. 2, no. 4, pp. 45-52, 1996.

[98] S. Lu, Y. Liu, and J. De La Ree, "Harmonics generated from a DC biased transformer," *IEEE Transactions on Power Delivery,* vol. 8, no. 2, pp. 725-731, 1993.

[99] W. Chandrasena, P. G. McLaren, U. D. Annakkage, and R. P. Jayasinghe, "An improved low-frequency transformer model for use in GIC studies," *IEEE Transactions on Power Delivery,* vol. 19, no. 2, pp. 643-651, 2004.

[100] A. A. Fardoun, E. F. Fuchs, and M. A. S. Masoum, "Experimental analysis of a DC bucking motor blocking geomagnetically induced currents," *IEEE Transactions on Power Delivery,* vol. 9, no. 1, pp. 88-99, 1994.

[101] P. R. Price, "Geomagnetically induced current effects on transformers," *IEEE Transactions on Power Delivery,* vol. 17, no. 4, pp. 1002-1008, 2002.

[102] R. A. Walling and A. N. Khan, "Characteristics of transformer exciting-current during geomagnetic disturbances," *Power Delivery, IEEE Transactions on,* vol. 6, no. 4, pp. 1707-1714, 1991.

[103] D. Lin, E. F. Fuchs, and M. Doyle, "Computer-aided testing of electrical apparatus supplying nonlinear loads," *IEEE Transactions on Power Systems,* vol. 12, no. 1, pp. 11-21, 1997.

[104] E. F. Fuchs, D. Yildirim, and T. Batan, "Innovative procedure for measurement of losses of transformers supplying nonsinusoidal loads," *IEE Proceedings-Generation, Transmission and Distribution,* vol. 146, no. 6, pp. 617-625, 1999.

[105] D. Lin and E. F. Fuchs, "Real-time monitoring of iron-core and copper losses of transformers under (non)sinusoidal operation," *IEEE Transactions on Power Delivery,* vol. 21, no. 3, pp. 1333-1341, 2006.

[106] V. M. Montsinger, "Loading transformers by temperature," *Transactions of the American Institute of Electrical Engineers,* vol. 49, no. 2, pp. 776-790, 1930.

[107] M. K. Pradhan and T. S. Ramu, "On the estimation of elapsed life of oil-immersed power transformers," *IEEE Transactions on Power Delivery,* vol. 20, no. 3, pp. 1962-1969, 2005.

[108] S. M. M. Agah and H. A. Abyaneh, "Distribution transformer loss-of-life reduction by increasing penetration of distributed generation," *IEEE Transactions on Power Delivery,* vol. 26, no. 2, pp. 1128-1136, 2011.

[109] L. Rui-jin, Y. Li-jun, L. Jian, and S. Grzybowski, "Aging condition assessment of transformer oil-paper insulation model based on partial

discharge analysis," *IEEE Transactions on Dielectrics and Electrical Insulation,* vol. 18, no. 1, pp. 303-311, 2011.

[110] L. W. Pierce, "Thermal considerations in specifying dry-type transformers," *IEEE Transactions on Industry Applications,* vol. 30, no. 4, pp. 1090-1098, 1994.

[111] E. F. Fuchs, D. J. Roesler, and K. P. Kovacs, "Aging of electrical appliances due to harmonics of the power system's voltage," *IEEE Transactions on Power Delivery,* vol. 1, no. 3, pp. 301-307, 1986.

[112] E. F. Fuchs, D. J. Roesler, and F. S. Alashhab, "Sensitivity of electrical appliances to harmonics and fractional harmonics of the power system's voltage. Part I: Transformers and induction machines," *IEEE Transactions on Power Delivery,* vol. 2, no. 2, pp. 437-444, 1987.

[113] E. F. Fuchs, D. J. Roesler, and K. P. Kovacs, "Sensitivity of electrical appliances to harmonics and fractional harmonics of the power system's voltage. Part II: Television sets, induction watthour meters and universal machines," *IEEE Transactions on Power Delivery,* vol. 2, no. 2, pp. 445-453, 1987.

[114] T. Stensland, E. F. Fuchs, W. M. Grady, and M. T. Doyle, "Modeling of magnetizing and core-loss currents in single-phase transformers with voltage harmonics for use in power flow," *IEEE Transactions on Power Delivery,* vol. 12, no. 2, pp. 768-774, 1997.

[115] E. F. Fuchs, D. Yildirim, and W. M. Grady, "Measurement of eddy-current loss coefficient P_{EC-R}, derating of single-phase transformers, and comparison with K-factor approach," *IEEE Transactions on Power Delivery,* vol. 15, no. 1, pp. 148-154, 2000.

[116] E. F. Fuchs, D. Yildirim, and W. M. Grady, "Corrections to "measurement of eddy-current loss coefficient P_{EC-R}, derating of single-phase transformers, and comparison with K-factor approach"," *IEEE Transactions on Power Delivery,* vol. 15, no. 4, p. 1357, 2000.

[117] P. S. Moses and M. A. S. Masoum, "Three-phase asymmetric transformer aging considering voltage-current harmonic interactions, unbalanced nonlinear loads, magnetic couplings and hysteresis," *IEEE Transactions on Energy Conversion,* vol. 27, no. 2, pp. 318-327, 2012.

[118] M. A. S. Masoum, P. S. Moses, and S. Deilami, "Load management in smart grids considering harmonic distortion and transformer derating," in *Proc.*

International Conference on Innovative Smart Grid Technologies (ISGT), 2010, pp. 1-7.

[119] S. Deilami, A. Masoum, P. S. Moses, and M. A. S. Masoum, "Real-time coordination of Plug-In Electric Vehicle charging in smart grids to minimize power losses and improve voltage profile," *IEEE Transactions on Smart Grid,* vol. 2, no. 3, pp. 456-467, 2011.

[120] J. Hopkinson, "The theory of alternating currents, particularly in reference to two alternate-current machines connected to the same circuit," *Journal of the Society of Telegraph-Engineers and Electricians,* vol. 13, no. 54, pp. 496-515, 1884.

[121] W. E. Ayrton and J. Perry, "Laboratory notes on alternate-current circuits," *Journal of the Institution of Electrical Engineers,* vol. 18, no. 79, pp. 284-311, 1889.

[122] W. M. Mordey, "On alternate-current working," *Journal of the Institution of Electrical Engineers,* vol. 18, no. 81, pp. 583-630, 1889.

[123] J. Swinburne, "Transformer distribution," *Journal of the Institution of Electrical Engineers,* vol. 20, no. 92, pp. 163-195, 1891.

[124] A. Siemens, "Some experimental investigations of alternate currents," *Journal of the Institution of Electrical Engineers,* vol. 21, no. 97, pp. 164-184, 1892.

[125] N. Tesla, "Experiments with alternate currents of high potential and high frequency," *Journal of the Institution of Electrical Engineers,* vol. 21, no. 97, p. 51, 1892.

[126] C. P. Steinmetz, "Some features of alternating current systems," *Transactions of the American Institute of Electrical Engineers,* vol. XII, pp. 326-349, 1895.

[127] S. Massoud Amin and B. F. Wollenberg, "Toward a smart grid: power delivery for the 21st century," *IEEE Power and Energy Magazine,* vol. 3, no. 5, pp. 34-41, 2005.

[128] F. Jiyuan and S. Borlase, "The evolution of distribution," *IEEE Power and Energy Magazine,* vol. 7, no. 2, pp. 63-68, 2009.

[129] S. M. Amin, "For the good of the grid," *IEEE Power and Energy Magazine,* vol. 6, no. 6, pp. 48-59, 2008.

[130] T. F. Garrity, "Getting Smart," *IEEE Power and Energy Magazine,* vol. 6, no. 2, pp. 38-45, 2008.

[131] A. Ipakchi and F. Albuyeh, "Grid of the future," *IEEE Power and Energy Magazine,* vol. 7, no. 2, pp. 52-62, 2009.

[132] E. M. Lightner and S. E. Widergren, "An orderly transition to a transformed electricity system," *IEEE Transactions on Smart Grid,* vol. 1, no. 1, pp. 3-10, 2010.

[133] P. Wolfs and S. Islam, "Potential barriers to smart grid technology in Australia," in *Proc. Australasian Universities Power Engineering Conference (AUPEC)*, Adelaide, Australia, 2009, pp. 1-6.

[134] B. D. Russell and C. L. Benner, "Intelligent systems for improved reliability and failure diagnosis in distribution systems," *IEEE Transactions on Smart Grid,* vol. 1, no. 1, pp. 48-56, 2010.

[135] K. Moslehi and R. Kumar, "A reliability perspective of the smart grid," *IEEE Transactions on Smart Grid,* vol. 1, no. 1, pp. 57-64, 2010.

[136] A. R. Metke and R. L. Ekl, "Security technology for smart grid networks," *IEEE Transactions on Smart Grid,* vol. 1, no. 1, pp. 99-107, 2010.

[137] F. Rahimi and A. Ipakchi, "Demand response as a market resource under the smart grid paradigm," *IEEE Transactions on Smart Grid,* vol. 1, no. 1, pp. 82-88, 2010.

[138] S. Bruno, S. Lamonaca, M. La Scala, G. Rotondo, and U. Stecchi, "Load control through smart-metering on distribution networks," in *Proc. IEEE Bucharest PowerTech*, 2009, pp. 1-8.

[139] T. Gönen, *Electric power distribution system engineering*: McGraw-Hill, Inc., 1986.

[140] T. Gönen, *Electric power transmission system engineering: analysis and design*: John Willey & Sons, Inc., 1988.

[141] K. Clement-Nyns, E. Haesen, and J. Driesen, "The impact of charging plug-in hybrid electric vehicles on a residential distribution grid," *IEEE Transactions on Power Systems,* vol. 25, no. 1, pp. 371-380, 2010.

[142] P. Fairley, IEEE Spectrum, "Speed bumps ahead for electric-vehicle charging," 2010. [Online]. Available: http://spectrum.ieee.org/green-tech/advanced-cars/speed-bumps-ahead-for-electricvehicle-charging.

[143] "MATLAB/Simulink Version 7.8.0.347 (R2009a)," Natick, MA: Math-Works, Inc.

[144] S. Civanlar and J. J. Grainger, "Volt/VAr control on distribution systems with lateral branches using shunt capacitors and voltage regulators part III: the

numerical results," *IEEE Transactions on Power Apparatus and Systems,* vol. PAS-104, no. 11, pp. 3291-3297, 1985.

[145] P. S. Moses, S. Deilami, A. S. Masoum, and M. A. S. Masoum, "Power quality of smart grids with plug-in electric vehicles considering battery charging profile," in *Proc. IEEE PES Conference on Innovative Smart Grid Technologies (ISGT) Europe*, Chalmers Lindholmen, Gothenburg, Sweden, 2010, pp. 1-7.

[146] E. Sortomme, M. M. Hindi, S. D. J. MacPherson, and S. S. Venkata, "Coordinated charging of plug-in hybrid electric vehicles to minimize distribution system losses," *IEEE Transactions on Smart Grid,* vol. 2, no. 1, pp. 198-205, 2011.

[147] A. Masoum, S. Deilami, P. S. Moses, M. A. S. Masoum, and A. Abu-Siada, "Smart load management of Plug-In Electric Vehicles in distribution and residential networks with charging stations for peak shaving and loss minimization considering voltage regulation," *IET Generation, Transmission & Distribution,* vol. 5, no. 8, pp. 877-888, 2011.

[148] J. A. P. Lopes, F. J. Soares, and P. M. R. Almeida, "Identifying management procedures to deal with connection of Electric Vehicles in the grid," in *Proc. IEEE Bucharest PowerTech*, 2009, pp. 1-8.

[149] M. A. S. Masoum, P. S. Moses, and S. Hajforoosh, "Distribution transformer stress in smart grid with coordinated charging of plug-in electric vehicles," in *Proc. International Conference on Innovative Smart Grid Technologies (ISGT)*, Washington D. C., USA, 2012, pp. 1-7.

[150] P. S. Moses, M. A. S. Masoum, and S. Hajforoosh, "Impacts of random and uncoordinated Plug-In Electric Vehicle charging on distribution transformer loading," in *Proc. International Conference on Innovative Smart Grid Technologies (ISGT)*, Washington D. C., USA, Accepted for publication.

[151] A. S. Masoum, M. Ladjavardi, E. F. Fuchs, and W. M. Grady, "Application of local variations and maximum sensitivities selections for optimal placement of shunt capacitor banks under nonsinusoidal operating conditions," *International Journal of Electrical Power and Energy Systems,* vol. 26, no. 10, pp. 761-769, 2004.

[152] "MATLAB/Simulink Version 7.8.0.347 (R2009a) : simulink example of wind farm using doubly-fed Induction generators," Natick, MA: Math-Works, Inc.

Every reasonable effort has been made to acknowledge the owners of copyright material. I would be pleased to hear from any copyright owner who has been omitted or incorrectly acknowledged.

Appendix A – Three-phase transformer electric and magnetic circuit model parameters

Electromagnetic circuit parameters for the four studied transformers (T1-T4): 1.65 kVA ($440\sqrt{3}/55\sqrt{3}$ V), 7.5 kVA (380/220 V), 60 kVA (380/220 V) and 2 MVA (25 kV/575 V) three-phase three-leg transformers (Tables A1- A2). Model parameters of these transformers have been determined from data available in [26, 28, 39, 152] including B-H characteristics, open and short-circuit tests performed in this work.

Table A1
Hysteresis and magnetic core model data.

Ascending function $\phi_x^+(f_x)$	**Descending function** $\phi_x^-(f_x)$
Transformer #1 (T1)	
$\alpha_a = 0.73, \beta_a = 300, \sigma_a = 0.2$	$\alpha_a = 0.73, \beta_a = 300, \sigma_a = 0.1$
$\alpha_b = 0.65, \beta_b = 1400, \sigma_b = 0.1$	$\alpha_b = 0.68, \beta_b = 1400, \sigma_b = 0.01$
$\alpha_c = 0.73, \beta_c = 300, \sigma_c = 0.2$	$\alpha_c = 0.73, \beta_c = 300, \sigma_c = 0.1$
$\Re_0 = 1500$ At/Wb , $\rho_a = 0.1,\ \rho_b = 1.0,\ \rho_c = 0.1$	
Transformer #2 (T2)	
$\alpha_a = 0.20, \beta_a = 171, \sigma_a = 0.17$	$\alpha_a = 0.19, \beta_a = 188, \sigma_a = 0.17$
$\alpha_b = 0.19, \beta_b = 518, \sigma_b = 0.15$	$\alpha_b = 0.20, \beta_b = 423, \sigma_b = 0.14$
$\alpha_c = 0.20, \beta_c = 171, \sigma_c = 0.17$	$\alpha_c = 0.19, \beta_c = 188, \sigma_c = 0.17$
$\Re_0 = 150$ At/Wb , $\rho_a = 0.001,\ \rho_b = 0.01,\ \rho_c = 0.01$	
Transformer #3 (T3)	
$\alpha_a = 0.92, \beta_a = 100, \sigma_a = 0.2$	$\alpha_a = 0.92, \beta_a = 100, \sigma_a = 0.2$
$\alpha_b = 0.70, \beta_b = 1000, \sigma_b = 0.1$	$\alpha_b = 0.70, \beta_b = 1100, \sigma_b = 0.1$
$\alpha_c = 0.92, \beta_c = 100, \sigma_c = 0.2$	$\alpha_c = 0.92, \beta_c = 100, \sigma_c = 0.2$
$\Re_0 = 1300$ At/Wb , $\rho_a = 0.001,\ \rho_b = 0.01,\ \rho_c = 0.01$	
Transformer #4 (T4)	
$\alpha_a = 0.73, \beta_a = 300, \sigma_a = 0.2$	$\alpha_a = 0.73, \beta_a = 300, \sigma_a = 0.1$
$\alpha_b = 0.65, \beta_b = 1400, \sigma_b = 0.1$	$\alpha_b = 0.68, \beta_b = 1400, \sigma_b = 0.01$
$\alpha_c = 0.73, \beta_c = 300, \sigma_c = 0.2$	$\alpha_c = 0.73, \beta_c = 300, \sigma_c = 0.1$
$\Re_0 = 1500$ At/Wb , $\rho_a = 0.1,\ \rho_b = 1.0,\ \rho_c = 0.1$	

Table A2
Transformer data and electric equivalent circuit parameters

Description	Data			
	T1	**T2**	**T3**	**T4**
Primary voltage	$440\sqrt{3}$ V	380 V	380 V	25 kV
Secondary voltage	$55\sqrt{3}$ V	220 V	220 V	575 V
Operating frequency	50 Hz	50 Hz	50 Hz	50 Hz
Rated power	1.65 kVA	7.5 kVA	60 kVA	2 MVA
Primary winding resistance per phase	9.4229 Ω (0.0268 pu)	0.313 Ω (0.0163 pu)	0.0036 Ω (0.0015 pu)	0.2604 Ω (0.05 pu)
Secondary winding resistance per phase	0.1472 Ω (0.0268 pu)	0.105 Ω (0.0163 pu)	0.0012 Ω (0.0015 pu)	0.147 Ω (0.05 pu)
Primary leakage inductance per phase	6.3411 mH (0.00566 pu)	0.996 mH (5.186e-5 pu)	0.1524 mH (6.332e-5 pu)	0.138 mH (0.025 pu)
Secondary leakage inductance per phase	0.0991 mH (0.00566 pu)	0.334 mH (5.186e-5 pu)	0.0511 mH (6.332e-5 pu)	0.0013 mH (0.025 pu)

$Z_{p,\,base} = N^2 \cdot Z_{s,\,base} = N^2 \cdot v_{s,\,(rated)} / i_{s,\,(rated)}$ (primary referred)

Appendix B – Three-phase ferroresonance circuits

Further system configurations resulting in unbalanced three-phase switching with different ferroresonance paths are shown in Fig. A-1. Different combinations of three-phase single-pole switching together with delta and star (grounded or ungrounded) transformer primary winding connections can result in a ferroresonant circuit involving system capacitances in series with nonlinear magnetising inductances of the transformer magnetic core

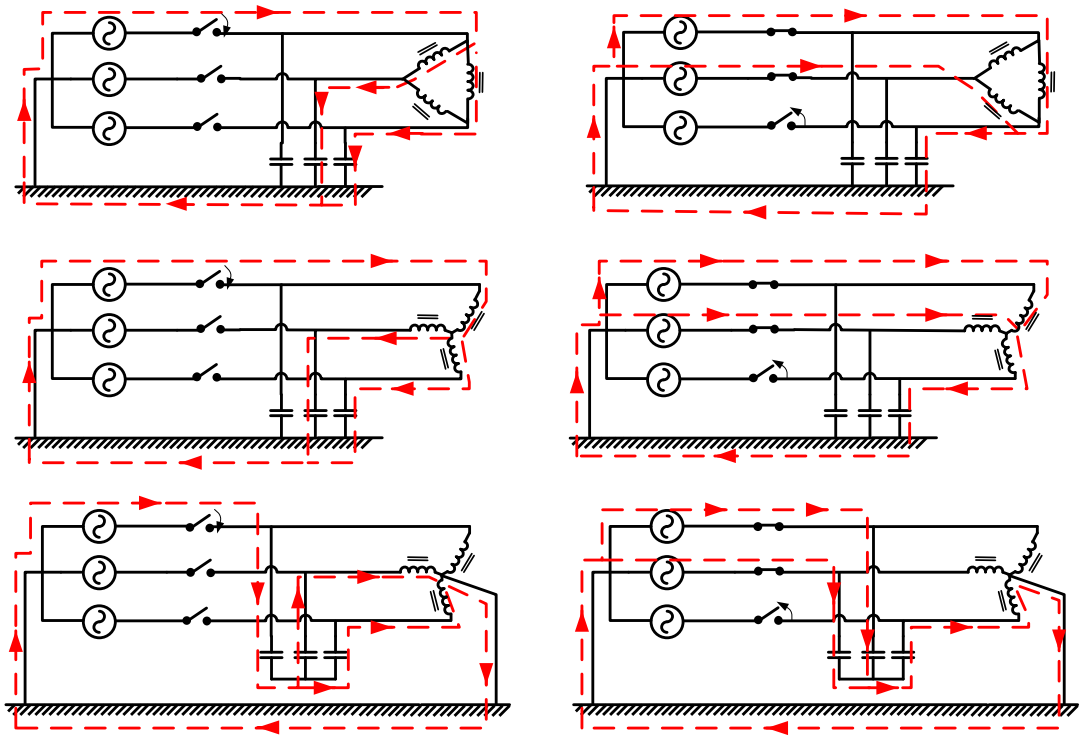

Fig. A-1. Examples of unbalanced three-phase switching resulting in different ferroresonance paths (shown in dashed red lines).

Appendix C – PSPICE computer program code listing

Listed here is an example of the developed base code implementation of the proposed nonlinear three-phase transformer model programmed in PSPICE syntax [27]. Several variations of this code were used and built upon in order to carry out different investigations for this thesis. Although the underlying code for electric and magnetic circuit model remains static in all simulation code versions, the transformer environment is custom modified to mimic each power quality disturbance for each study (e.g., nonsinusoidal functions for load and source behaviour, capacitors and switching for ferroresonance, dc sources for GICs, etc.).

```
**********************************************************
***** Three-Phase Three-Leg Transformer Model ************
***** Rated primary/secondary winding voltage 440/55 V ***
***** Secondary winding rated at 10 Amps *****************
***** Source Code Programmer: Mr. Paul S. Moses
*****.Date of base version: 1 OCT 2010 ******************************
**********************************************************

* Transient analysis settings
.TRAN 0.2ms 5s 0.0s 0.2ms SKIPBP

* Constants
.PARAM PI=3.14159265 FSEQ={2*PI/3} FREQ = 50 W0={2 * PI * FREQ}
+ PHASEDEG = {0} PHASE = {PHASEDEG * PI/180}

* Electrical open and short-circuit test parameters
.PARAM NP = 1 NS = {1/(440/55)}
```

```
+ RPRI = 9.4229 RSEC = 0.1472 LPRI = 6.3411m LSEC = 0.0991m
+ RCORE = 14308  RZERO = 150

* Define nonlinear magnetising characteristic function
.FUNC H(X,K1,K2) {SGN(X)*(K1*LOG10(K2*ABS(X)+1))}

* Primary phase voltage values (RMS and peak)
.PARAM URMS = {440} UMAX = {URMS*SQRT(2/3)}

* Magnetising reluctance characteristic function
+ K1A = 0.92     K1B = 0.7       K1C = 0.92
+ K2A = 100     K2B = 1000       K2C =  100

* Ramping initial voltage
ERAMP 1 0 VALUE {TABLE(TIME, 1m, 0, 0.5, 1)}

* Single-phase switching transients
.MODEL Smod VSWITCH(Ron=1m Roff=1MEG Von=1V Voff=0V)
Sw1 810 10 501 0 Smod
Sw2 820 20 502 0 Smod
Sw3 830 30 503 0 Smod
ESW1   501 0 VALUE    {1};   {TABLE(TIME,   0, 1,   2.600,1,    2.600000001,0 )}
ESW2   502 0 VALUE          {TABLE(TIME,   0, 1,    1.0000,1,    1.00000001,0 )}
ESW3   503 0 VALUE    {1};   {TABLE(TIME,   0, 1,    2.130,1,    2.130001,0 )}

*******************************
* Electric equivalent circuit *
*******************************
* Three-phase voltage source functions connected to transformer primary
EGA 810 0 VALUE {UMAX*V(1)*COS(W0*TIME  +PHASE)}
EGB 820 0 VALUE {UMAX*V(1)*COS(W0*TIME-FSEQ+PHASE)}
EGC 830 0 VALUE {UMAX*V(1)*COS(W0*TIME+FSEQ+PHASE)}
```

```
* CB grading capacitor
.PARAM Cseries = 0.03n
CGA 810 10 {Cseries}
CGB 820 20 {Cseries}
CGC 830 30 {Cseries}

* Shunt capacitance
.PARAM Cshunt = 30.6u
CPA 10 0 {Cshunt}
CPB 20 0 {Cshunt}
CPC 30 0 {Cshunt}

* Primary impedances and winding connections (Star)
RPRIA  10 12 {RPRI}                    ; Winding resistance
LPRIA 12 14 {LPRI}                ; Leakage flux inductance
RCOREA 14 NP {RCORE}                ; Core loss resistance
EPRIA  14 NP VALUE {NP*DDT(-I(EFA))} ; Induced voltage

RPRIB  20 22 {RPRI}                    ; Winding resistance
LPRIB 22 24 {LPRI}                     ; Leakage flux inductance
RCOREB 24 NP {RCORE}                ; Core loss resistance
EPRIB  24 NP VALUE {NP*DDT(-I(EFB))} ; Induced voltage

RPRIC  30 32 {RPRI}                    ; Winding resistance
LPRIC 32 34 {LPRI}                     ; Leakage flux inductance
RCOREC 34 NP {RCORE}                ; Core loss resistance
EPRIC  34 NP VALUE {NP*DDT(-I(EFC))} ; Induced voltage

* Primary neutral connection
* VNP NP 0 0; Solidly grounded
RNP NP 0 {1/0}; Non-grounded
```

```
* Secondary impedances and winding connections (Star)
RSECA  40 42 {RSEC}
LSECA 42 44 {LSEC}
ESECA  44 NS VALUE {NS*DDT(-I(EFA))}; esa=Ns_dphi_a/dt

RSECB  50 52 {RSEC}
LSECB 52 54 {LSEC}
ESECB  54 NS VALUE {NS*DDT(-I(EFB))}; esb=Ns_dphi_b/dt

RSECC  60 62 {RSEC}
LSECC 62 64 {LSEC}
ESECC  64 NS VALUE {NS*DDT(-I(EFC))}; esc=Ns_dphi_c/dt

* Secondary neutral connection
* VNS NS 0 0; Solidly grounded
RNS NS 0 {1M}; Non-grounded

* Secondary load (open-circuit)
.PARAM RLOAD = {1/0}
RLA 40 NS {RLOAD}
RLB 50 NS {RLOAD}
RLC 60 NS {RLOAD}

*******************************************************
***** Magnetic equivalent circuit for three-leg topology ********
*******************************************************

EFA 102   0 VALUE {NP*I(EPRIA)+NS*I(ESECA)}; Fa = Np_Ipea+Ns_Isa
GFA 102 115 VALUE {H(V(102, 115), K1A, K2A)}; phi_a

EFB 202   0 VALUE {NP*I(EPRIB)+NS*I(ESECB)}; Fb = Np_Ipeb+Ns_Isb
GFB 202 115 VALUE {H(V(202, 115), K1B, K2B)}; phi_b
```

```
EFC 302   0 VALUE {NP*I(EPRIC)+NS*I(ESECC)}; Fc = Np_Ipec+Ns_Isc
GFC 302 115 VALUE {H(V(302, 115), K1C, K2C)}; phi_c

* Zero-sequence reluctance
RD 115 0 {RZERO}

* Flux measurements
EFLUXA FLUXA 0 VALUE {-I(EFA)}
EFLUXB FLUXB 0 VALUE {-I(EFB)}
EFLUXC FLUXC 0 VALUE {-I(EFC)}

********************
*** Output plotting ***
********************

.PROBE V(10,NP) V(20,NP) V(30,NP) V(40,NS) v(50,NS) v(60,NS);
primary/secondary phase voltages
+  I(LPRIA) I(LPRIB) I(LPRIC)                ; primary winding currents
+  I(LSECA) I(LSECB) I(LSECC)                ; secondary winding currents
+  I(RCOREA) I(RCOREB) I(RCOREC)             ; core loss current
+  I(EPRIA)  I(EPRIB)  I(EPRIC)              ; magnetising current
+  V(EPRIA)  V(EPRIB)  V(EPRIC)              ; primary induced voltage
+  V([FLUXA]) V([FLUXB]) V([FLUXC])  ; flux linkage waveforms

.END
```

Appendix D – 1200 node smart grid test system data

Table A1 contains the system impedances and branch connections for the simulated low voltage 415V residential networks for the PEV smart grid study of Chapter 7. The original data is compiled from actual system data for a selected low voltage distribution system in the South West Interconnected System (SWIS) of Western Australia. The data is provided by courtesy of Western Power electric utility, Perth Western Australia.

Table A1

Parameters of the typical low voltage 415V residential systems (Fig. 7.1).

The 23 kV high voltage 30 bus test system is available in [144].

LINE		Line resistance R [Ω]	Line reactance X [Ω]	LINE		Line resistance R [Ω]	Line reactance X [Ω]
From node	To node			From node	To node		
1	2	0.0415	0.0145	23	24	0.7763	0.0774
2	4	0.0424	0.0189	21	22	0.5977	0.0596
4	6	0.0444	0.0198	16	17	0.1423	0.0496
6	8	0.0369	0.0165	17	18	0.0837	0.0292
8	9	0.0520	0.0232	18	19	0.3124	0.0312
9	12	0.0524	0.0234	16	20	0.0163	0.0062
12	13	0.0005	0.0002	1	35	0.0163	0.0062
12	15	0.2002	0.0200	35	40	0.0415	0.0145
12	14	1.7340	0.1729	40	42	0.0424	0.0189
9	11	0.2607	0.0260	42	44	0.0444	0.0198
9	10	1.3605	0.1357	44	46	0.0369	0.0165
6	7	0.1402	0.0140	46	47	0.0520	0.0232
4	5	0.7763	0.0774	47	50	0.0524	0.0234
2	3	0.5977	0.0596	50	51	0.0005	0.0002
1	16	0.0163	0.0062	50	53	0.2002	0.0200
16	21	0.0415	0.0145	50	52	1.7340	0.1729
21	23	0.0424	0.0189	47	49	0.2607	0.0260
23	25	0.0444	0.0198	47	48	1.3605	0.1357
25	27	0.0369	0.0165	44	45	0.1402	0.0140
27	28	0.0520	0.0232	42	43	0.7763	0.0774
28	31	0.0524	0.0234	40	41	0.5977	0.0596
31	32	0.0005	0.0002	35	36	0.1423	0.0496
31	34	0.2002	0.0200	36	37	0.0837	0.0292
31	33	1.7340	0.1729	37	38	0.3124	0.0312
28	30	0.2607	0.0260	35	39	0.0163	0.0062
28	29	1.3605	0.1357	Distribution transformer reactance			0.0654
25	26	0.1402	0.0140				